Pushing diffusion MRI towards new dimensions

Martins, Joao

2020

Citation for published version (APA):
Martins, J. (2020). *Pushing diffusion MRI towards new dimensions*. Lund University, Faculty of Science, Department of Chemistry, Division of Physical Chemistry.

Total number of authors:
1

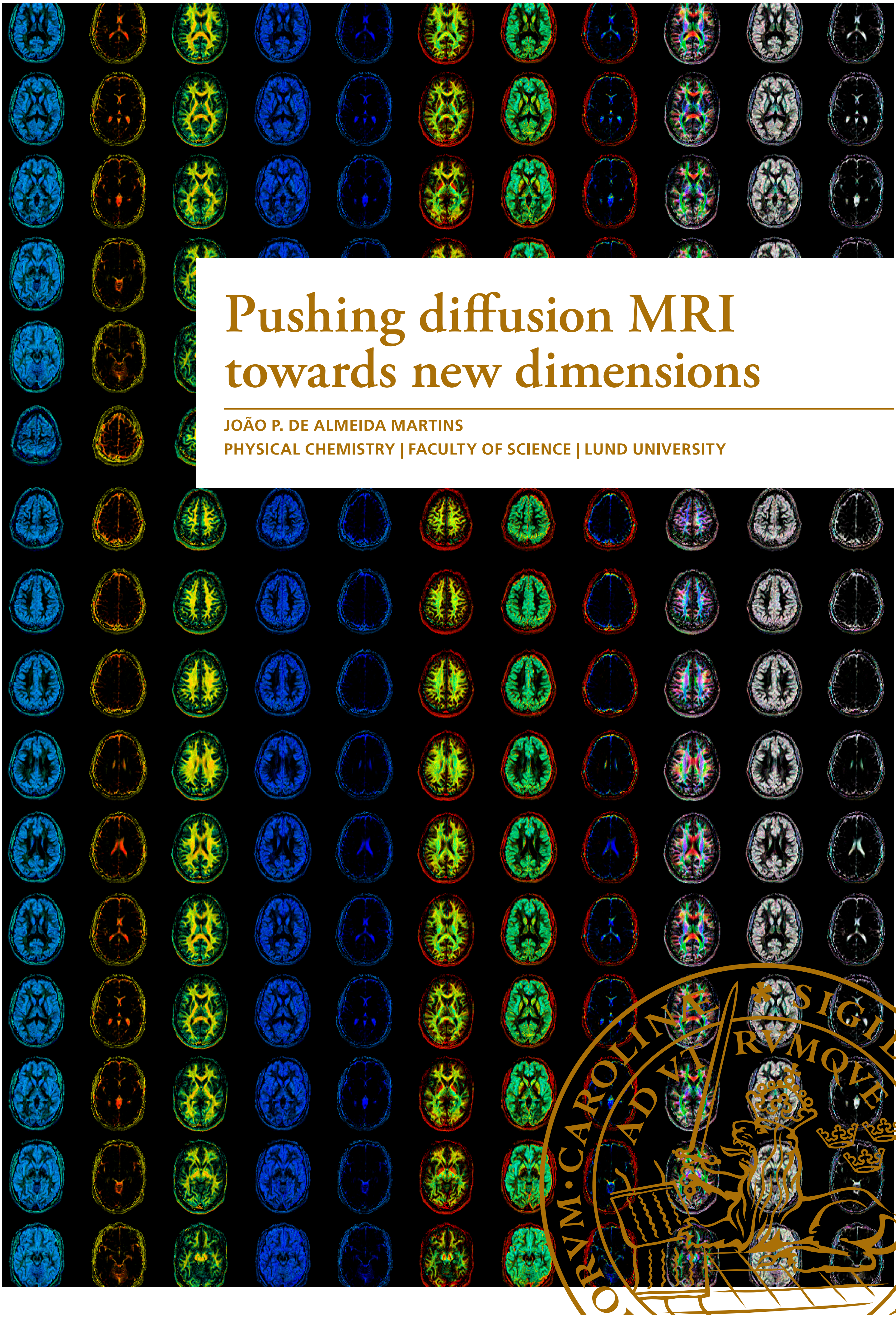

Pushing diffusion MRI towards new dimensions

JOÃO P. DE ALMEIDA MARTINS
PHYSICAL CHEMISTRY | FACULTY OF SCIENCE | LUND UNIVERSITY

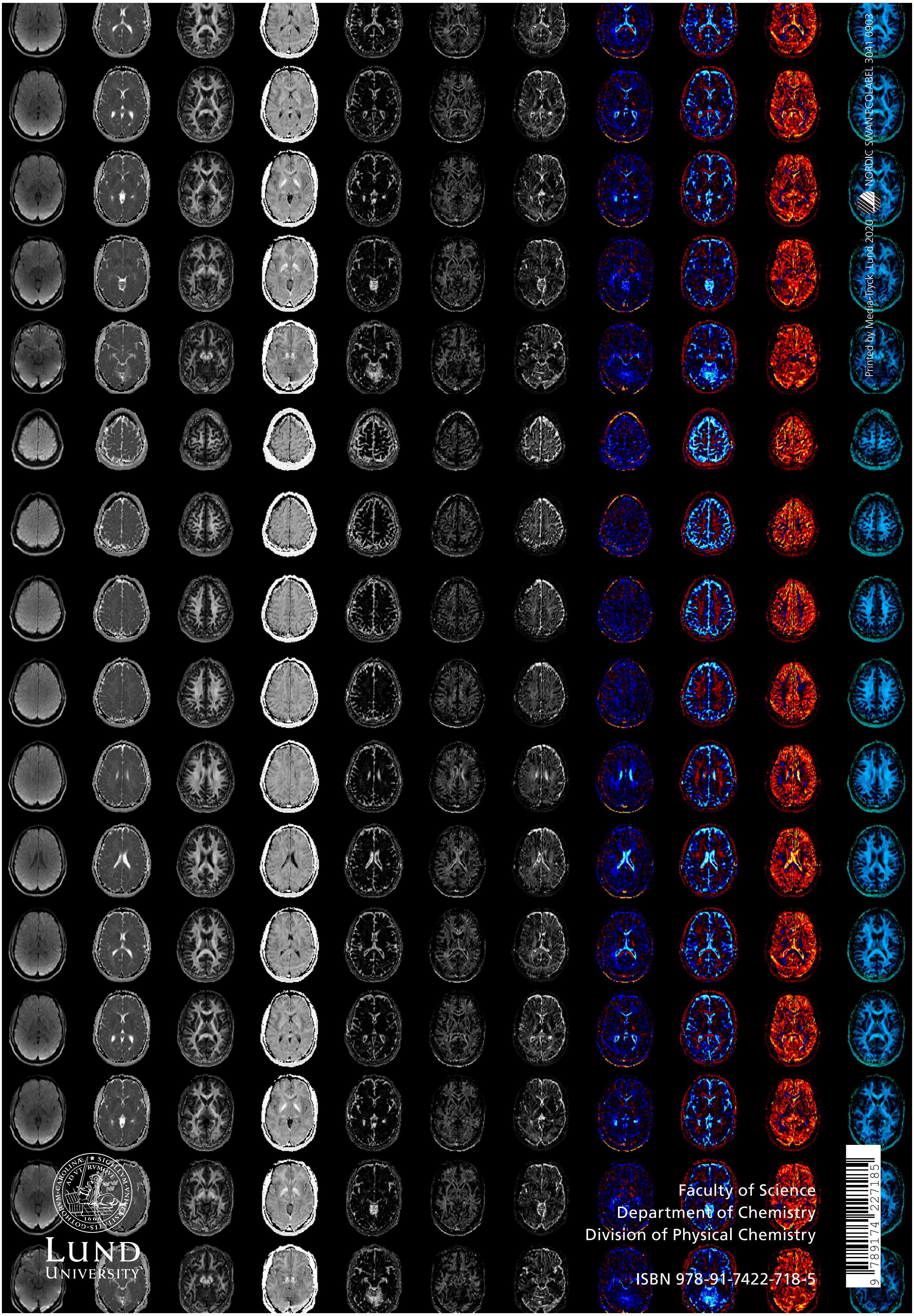

LUND
UNIVERSITY

Faculty of Science
Department of Chemistry
Division of Physical Chemistry

ISBN 978-91-7422-718-5

Printed by Media-Tryck, Lund 2020 NORDIC SWAN ECOLABEL 3041 0903

Pushing diffusion MRI towards new dimensions

Pushing diffusion MRI towards new dimensions

João P. de Almeida Martins

DOCTORAL DISSERTATION

by due permission of the Faculty of Science, Lund University, Sweden.
To be defended on Friday, the 31st of January 2020 at 13:15 in Lecture hall B at the Department of Chemistry, Lund University.

Faculty opponent

Professor Alex L. MacKay
University of British Columbia, Vancouver, Canada

DOKUMENTDATABLAD enl SIS 61 41 21

Organization
LUND UNIVERSITY
Department of Chemistry
Box 124
SE–221 00 LUND
Sweden

Document name
DOCTORAL DISSERTATION

Date of disputation
2020-01-31

Sponsoring organization
Swedish Foundation for Strategic Research

Author(s)
João P. de Almeida Martins

Title and subtitle
Pushing diffusion MRI towards new dimensions

Abstract

Diffusion-MRI techniques allow the non-invasive investigation of microstructural changes in living tissues. However, a detailed interpretation of the data is complicated by the fact that multiple microscopic environments with varying diffusion properties all contribute to the measured signal. To address this problem, we adapt strategies from solid-state NMR spectroscopy and magnetic resonance of porous media to design multidimensional diffusion MRI protocols that can establish correlations between distinct features of the underlying diffusion process. Inversion of the acquired data enables the quantification of tissue heterogeneity with non-parametric distributions of diffusion tensors. The size, shape, and orientation of the estimated diffusion tensors have direct relations to corresponding microstructural properties of biological tissues.

In Paper I, we introduced an experimental protocol to establish correlations between diffusion tensor eigenvalues. The proposed approach was extended in Paper II, where we correlated individual diffusion tensor parameters with both longitudinal and transverse relaxation rates. In both papers, experimental validation was conducted using spectroscopic experiments on a set of specially tailored synthetic samples. Multidimensional distributions retrieved from the correlated datasets were found to provide excellent resolution between microscopic environments with distinct diffusion properties.

In Paper III, we assessed the performance of our data inversion strategies within a clinical context using *in silico* data. We found that the proposed model-free algorithm preserves good contrast between systems with different microscopic structures, even though its accuracy is significantly affected by high-levels of experimental noise. The algorithm was also observed to exhibit no biases at infinite signal-to-noise ratios.

In Paper IV we combined our diffusion tensor correlation protocols with MRI sequences allowing for sub-millimetre imaging of living tissues. The method was demonstrated with measurements on *in vivo* mouse brain and was validated using a set of phantoms emulating the diffusion properties of brain tissues.

In Papers V and VI we investigated the microscopic heterogeneity of the living human brain with spatially resolved relaxation-diffusion distributions. The retrieved distributions allowed the resolution, characterisation, and mapping of distinct microscopic tissue environments.

Key words
NMR, MRI, diffusion, relaxation, multidimensional diffusion MRI, relaxation-diffusion correlations, Laplace NMR, porous media, tissue microstructure, heterogeneity, anisotropy

Classification system and/or index terms (if any)

Supplementary bibliographical information

Language
English

ISSN and key title

ISBN
978-91-7422-718-5 (print)
978-91-7422-719-2 (pdf)

Recipient's notes

Number of pages
91

Price

Security classification

I, the undersigned, being the copyright owner of the abstract of the above-mentioned dissertation, hereby grant to all reference sources the permission to publish and disseminate the abstract of the above-mentioned dissertation.

Signature João Pedro de Almeida Martins Date 2019-12-13

Pushing diffusion MRI towards new dimensions

João P. de Almeida Martins

LUND
UNIVERSITY

Cover illustration front and back: A brain pop art panel built from the novel parameter maps derived in this work.

Funding information: The thesis work was financially supported by the Swedish Foundation for Strategic Research.

Faculty of Science, Department of Chemistry, Division of Physical Chemistry

ISBN: 978-91-7422-718-5 (print)
ISBN: 978-91-7422-719-2 (pdf)

Printed in Sweden by Media-Tryck, Lund University, Lund 2020

Printed matter
3041 0903

Media-Tryck is an environmentally
certified and ISO 14001:2015 certified
provider of printed material.
Read more about our environmental
work at www.mediatryck.lu.se

MADE IN SWEDEN

Table of Contents

Acknowledgements

First of all, I would like to express my deepest gratitude to my supervisor, Daniel. Thank you very much for replying to the e-mail of an unknown student and giving me the opportunity to work on this project. I have learned a lot working under your supervision and for that I am very grateful.

Markus, thank you for always having an open door for me and being willing to discuss the various aspects of this work. Your constructive criticism has been both helpful and appreciated.

Alexis and Linn, I cannot find the words to thank you enough. Your suggestions, comments and revisions in these final weeks have been so precious and have really made this thesis possible. Plus, I have enjoyed your company so much, both in the Division and outside.

I would also like to extend my gratitude to all the past and present members of the NMR group: Stefanie, Mikael, Dat, Sarah and Simon, and the Master students I had the pleasure to supervise: Hong, Johnathan and Paolo.

During my time as a PhD student, I was also very lucky to work at Random Walk Imaging, a tiny company packed with wonderful people. Kajsa, thank you for being such an unconventional and fun boss. Samo, I will always remember our interesting discussions about work and life in general. Greta, you are just too cool and fun!

Special thanks to my co-authors Filip, Chantal and Maxime. Filip, thank you for the amazing data and the valuable advices. Also, let's not forget our impromptu trip to China. Chantal, thank you for introducing me to the world of brain MRI and for making my trips to Cardiff so pleasant. Maxime, our collaboration has been short but productive.

Göran, thanks you for all the assistance with the NMR spectrometer and for sitting down with me trying to figure out which gradient coil was busted.

I would also like to thank the past and present members of the Physical Chemistry Divisions for creating such a pleasant work environment. You have set a high bar for my future workplace. My sincerest gratitude to Helena, Maria and Chris, for making everything work so smoothly. Special thanks to those who shared with me the loud lunches, late fikas and late working hours. I truly enjoyed your company. Thiago, Janne-Mieke, Julien, Luigi, Ilaria and Andrea, you have been missed so much!

A shout-out to the Mölle people, for the crazy fun times.

Maria, Jordi, Maxime, Jojo, Jasper and Polina, I am looking forward to more laughs, drinks and adventures around the world!

To my parents and my sister, thank you for always being there for me and for the support from far-away Portugal. The silly WhatsApp messages really improved my mood in the toughest writing days.

Last, but certainly not least, Marta thank you very much for the unwavering support and love. I am incredibly lucky to have you on my team!

Popular summary in English

Since the ancient times, humans have been interested in studying biological tissues, their structures, and properties. In popular culture, an illustrious example of this thirst for knowledge is Leonardo da Vinci. During many years of research, not only did he meticulously investigate the architecture of the live human body, inventorying its muscles, tendons and visible subcutaneous structure, but he also accurately dissected the deceased human body to gain a deeper understanding of the skeleton and internal organs. These invasive studies were, for the most part of human history, the only opportunity for a systematic investigation of the internal tissues. The advent of magnetic resonance imaging (MRI) techniques in the 1970s has significantly contributed to changing this paradigm.

Through a clever manipulation of magnetic field gradients and pulses, MRI allows humans to non-invasively visualize the internal organs of living beings with a millimetre spatial resolution and without relying on ionizing radiation. Such technique could be applied on healthy subjects and on patients for pathology diagnosis, guaranteeing patient comfort. However, the remarkable achievements of MRI did not extinguish our scientific ambitions. Indeed, efforts were made to widen the range of biological length-scales accessible via MRI, to explore not only the macroscopic structure of the tissues under examination, but also their microstructure, *i.e.* the ensemble of properties characterising the cells comprising the tissue itself. This objective was achieved by diffusion MRI, which is able to capture the diffusion patterns of water molecules within cells.

However, the interpretation of the signals measured from diffusion NMR/MRI in terms of microscopic structures has remained rather unreliable for the past 30 years. This is due, on the one hand, to the many assumptions that are usually made to simplify the link between the measured signal and the underlying microstructure and, on the other hand, to the fact that complex information has to be extracted from few measured signals, especially when patient comfort imposes short MRI acquisition times. Nonetheless, pushing our mastery of diffusion MRI is crucial to biomedicine, as the subtlety and non-invasiveness of such technique are key to the proper understanding and diagnosing of live tissues.

The work within this thesis has tackled the difficulties in interpreting diffusion MRI. By drawing inspiration from magnetic resonance techniques designed to study materials such as polymers or rocks, we were able to devise new experimental strategies that enhance the amount of information attainable with diffusion MRI. The boost in information was then used to quantify new diffusion features that have an intuitive relationship with the microstructure of living tissues

List of Publications

This thesis is based on the following publications, referred to by their Roman numerals:

I **Two-Dimensional Correlation of Isotropic and Directional Diffusion Using NMR**
J. P. de Almeida Martins, D. Topgaard
Physical Review Letters **2016**, 116, 087601

II **Multidimensional correlation of nuclear relaxation rates and diffusion tensors for model-free investigations of heterogeneous anisotropic porous materials**
J. P. de Almeida Martins, D. Topgaard
Scientific Reports **2018**, 8, 2488

III **Trueness and precision of statistical descriptors obtained from multidimensional diffusion signal inversion algorithms**
A. Reymbaut, P. Mezzani, J. P. de Almeida Martins, D. Topgaard
Submitted to *NMR in Biomed.*

IV **Diffusion tensor distribution imaging of *in vivo* mouse brain at ultra-high magnetic field by spatiotemporal encoding**
M. Yon, J. P. de Almeida Martins, Q. Bao, M. D. Budde, L. Frydman, D. Topgaard
Manuscript in preparation

V **Transferring principles of solid-state and Laplace NMR to the field of *in vivo* brain MRI**
J. P. de Almeida Martins, C. M. W. Tax, F. Szczepankiewicz, D. K. Jones, C.-F. Westin, D. Topgaard
Submitted to *Magnetic Resonance*

VI **Mapping and visualizing fibres in heterogeneous brain voxels**
J. P. de Almeida Martins, C. M. W. Tax, F. Szczepankiewicz, D. K. Jones, D. Topgaard
Manuscript in preparation

All papers are reproduced with permission of their respective publishers.

Publications not included in this thesis:

Dynamics of binary mixtures of an ionic liquid and ethanol by NMR

A. Ordikhani Seyedlar, J. P. de Almeida Martins, P. J. Sebastião, M. J. Jardim Beira, S. Stapf, F. Vaca Chávez, C. Mattea
Magnetic Resonance in Chemistry **2018**, 56, 108

Abbreviations

CSF	CerebroSpinal Fluid
DTD	Diffusion Tensor Distribution
DTI	Diffusion Tensor Imaging
EPI	Echo-Planar Imaging
FA	Fractional Anisotropy
GM	Grey Matter
MR	Magnetic Resonance
MRI	Magnetic Resonance Imaging
NMR	Nuclear Magnetic Resonance
NNLS	Non-Negative Least Squares
ODF	Orientation Distribution Function
PAS	Principal Axis System
PGSE	Pulse Gradient Spin-Echo
SNR	Signal-to-Noise Ratio
SPEN	SPatiotemporal ENcoding
WM	White Matter

1 | Introduction

It is a well known fact that biological tissues naturally contain water molecules randomly moving through their cellular landscape. This cellular landscape poses as a hindrance to the translational motion of the molecules and thus the resulting diffusion pattern is intimately linked to the micrometer-scale structure and organization of the cell membranes. The close relationship between the diffusion pattern and the structure of the local tissue environment can be probed using diffusion magnetic resonance imaging (MRI) techniques where magnetic field gradients are applied to measure the mean squared displacement of the water molecules from which the diffusion can be derived.

Parameters derived from diffusion MRI measurements have been successfully used to quantify microstructural changes in both healthy and diseased tissues. However, despite their usefulness, conventional diffusion MRI techniques yield ambiguous results whenever the sample comprises multiple microscopic environments with distinct diffusion properties. Such ambiguities stem from the fact that the majority of diffusion measurements are performed with a set of gradients that are sensitive to an array of distinct properties such as local diffusivities, restrictions, anisotropy, flow, and ex- change. The sensitivity to a wide range of properties complicates the task of assigning the experimental observations to a specific diffusion mechanism.

In this thesis, we address this problem by using novel diffusion MRI acquisition- and analysis protocols to quantify the microscopic heterogeneity of the living human brain. The diffusion MRI framework presented in this thesis is based on data acquisition schemes from solid-state nuclear magnetic resonance (NMR) spectroscopy and Laplace NMR protocols from the field of porous media. Signal is acquired in a multidimensional space of experimental variables encoding for correlations between diffusivities, anisotropy, and pore orientation, and is then inverted into non-parametric distributions of diffusion tensors. This approach is fundamentally different from the current trend of microstructural in vivo MRI where sub-voxel composition is investigated by devising signal models with increasingly complex priors and constraints. Instead, we add complexity to the signal acquisition stage in order to quantify intra-voxel heterogeneity with non-parametric distributions that are retrieved from the data with minimal assumptions about the underlying tissue properties.

2 | Diffusion

Within Physical Chemistry, the term *diffusion* can be used to designate two processes of different physical origins: self- and mutual-diffusion. Self-diffusion refers to the stochastic motion of thermally excited particles; this process occurs at dynamic equilibrium and is driven by the internal kinetic energy of the system. In contrast, mutual diffusion describes the net particle movement towards equilibrium resulting from a chemical potential gradient. Diffusion magnetic resonance techniques measure the self- or translational diffusion of an ensemble of spin-bearing molecules. For this reason we focus on self-diffusion, which from this point onwards is merely referred to as *diffusion*.

The typical diffusion MRI experiment targets water molecules diffusing in a microscopically complex material such as biological tissue. The translational dynamics of water molecules is used as a probe of local structure, whose organization is inferred from the measured diffusion patterns. In this chapter we provide a basic conceptual description of diffusion in a complex heterogeneous structure, and describe how to quantify the diffusion process with distributions of diffusion tensors.

2.1 A simple picture of diffusion in complex media

The trajectory of a diffusing particle is defined by a series of inter-particle collisions. These collisions effectively make the diffusive motion a random process (Brownian motion) wherein the position $\mathbf{r}(t)$ of the individual particles cannot be predicted by deterministic dynamics. It is then convenient to characterize the system by its ensemble average properties. The fluctuations in $\mathbf{r}(t)$ can be quantified by the mean-square displacement, given for unrestricted diffusion by [1–3]

$$\left\langle (\mathbf{r}(t) - \mathbf{r}(0))^2 \right\rangle = 2\mathrm{d}D_0 t, \tag{2.1}$$

where $\mathrm{d} = 1, 2, 3$ describes the dimensionality of the system. The scalar D_0 is the free diffusion coefficient, a property specific to the medium through which the particles

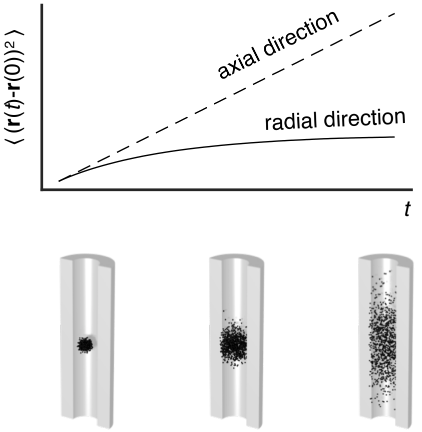

Figure 2.1: Brownian dynamics simulation of an ensemble of particles entrapped in an impermeable cylinder. The simulation was carried out as described in Ref. [6], where particle movement is reflected at the boundaries of the enclosing geometry. The top plot displays the mean-square displacement $\langle(\mathbf{r}(t) - \mathbf{r}(0))^2\rangle$ in directions parallel (axial direction) and perpendicular (radial direction) to the cylinder. The maximum displacement along the radial direction is limited by the radius of the cylinder.

diffuse.

Particles diffusing within a complex medium are bound to encounter obstacles that can either restrict or hinder their movement. The presence of these obstacles may not alter the intrinsic diffusivity of the system, but will reduce the average displacement registered for a given diffusion time. The extent to which the average displacement is reduced will depend on the geometry of the obstacles, their permeability, and the amount of time that particles are allowed to diffuse.

Hindrance and restriction effects can be quantified by solving Fick's diffusion equation with appropriate boundary conditions [4, 5]. However, such approach is beyond the scope of this thesis and we instead discuss the effects of restrictions in a qualitative fashion. An informative example is given in Figure 2.1, which displays an ensemble of Brownian particles diffusing within an impermeable cylinder of radius a [6]. The mean-square displacement along the cylinder (axial direction) is not affected by any obstacle and follows the linear trend predicted by Eq. 2.1. A different behaviour is observed for particle motion along the perpendicular (radial) direction. At very short diffusion times ($t \ll a^2/D_0$) most particles have not interacted with the cylinder wall and diffusion is essentially free. At longer times, the particles encounter the compartment boundary and their mean-square displacement is reduced in comparison to the free diffusion case. For sufficiently long times ($t \gg a^2/D_0$) the mean-square displacement plateaus at a value on the order of a^2.

The discussion in the previous paragraph shows that Eq. 2.1 is not formally applicable in the presence of restrictions, and different displacements may be probed depending on the time-scale of the measurement process [5, 7], *cf.* Figure 2.1. The measured diffusivities are thus unavoidably linked to the experimental design. This motivates the definition of an apparent diffusion coefficient D_{app} [8, 9] that depends on both the confining geometry and the complete set of relevant experimental parameters Ω:

$$D_{\mathrm{app}}(t_\Omega) = \frac{\langle ([\mathbf{r}(t_\Omega) - \mathbf{r}(0)] \cdot \mathbf{u}_\Omega)^2 \rangle}{2\mathrm{d}\, t_\Omega} \,, \tag{2.2}$$

where t_Ω and $\mathbf{u}_\Omega$ are the effective time-scale and directionality defined by the experimental setup, and $\langle \cdot \rangle$ denotes an ensemble average. Different values of D_{app} may be measured along different directions, a feature that indicates an anisotropic structural organization.

2.2 Diffusion tensors as probes of local structure

Water diffusion in tissues is typically an anisotropic process that can be approximated by a symmetric second-order tensor [10, 11]. The diffusion tensor $\mathbf{D}$ is written as a symmetric positive-semidefinite second-order tensor [10],

$$\mathbf{D} = \begin{pmatrix} D_{xx} & D_{xy} & D_{xz} \\ D_{yx} & D_{yy} & D_{yz} \\ D_{zx} & D_{zy} & D_{zz} \end{pmatrix} = \begin{pmatrix} D_{xx} & D_{xy} & D_{xz} \\ \cdot & D_{yy} & D_{yz} \\ \cdot & \cdot & D_{zz} \end{pmatrix} \,. \tag{2.3}$$

Symmetry requires $D_{ij} = D_{ji}$, meaning that $\mathbf{D}$ is fully described by 6 independent parameters. The various parameters of the diffusion tensor are interpreted as apparent diffusivities that reflect the restrictions and hindrances encountered by water molecules along a particular direction (see Eq. 2.2). Each microscopic $\mathbf{D}$ is then directly related to the geometry of the surrounding medium, and can be interpreted as a blurred representation of the local structure. The connection between the structure of the microscopic environment and the local diffusion pattern is illustrated in Figure 2.2, where diffusion tensors are visualized as superquadric tensor glyphs [12] with the lengths and directions of the principal axes given by the tensor eigenvalues and corresponding eigenvectors, respectively.

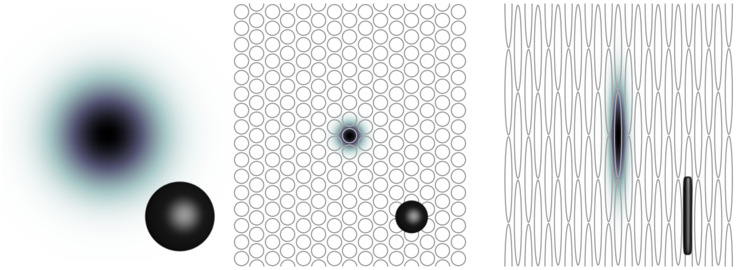

Figure 2.2: Schematic illustration of the link between tissue structure, diffusion patterns, and diffusion tensors. The underlying cellular architecture is observed to influence the size, shape, and orientation of water diffusion patterns, here represented as "ink stains". For example, densely packed spherical cells are observed to yield a small isotropic diffusion pattern. The corresponding diffusion tensors are depicted as superquadric tensor glyphs [12] with lengths and orientations of the semi-axes given by the diffusion tensor eigenvalues and eigenvectors. Adapted with permission from Ref.[13].

2.2.1 Tensor size and shape

In its principal axis system (PAS), a particular $\mathbf{D}$ can be represented by a diagonal matrix

$$\mathbf{D}^{\mathrm{PAS}} = \begin{pmatrix} D_{\mathrm{XX}} & 0 & 0 \\ 0 & D_{\mathrm{YY}} & 0 \\ 0 & 0 & D_{\mathrm{ZZ}} \end{pmatrix} , \tag{2.4}$$

whose elements correspond to the eigenvalues of Eq. 2.3 ordered according to the standard convention $|D_{\mathrm{ZZ}} - \mathrm{Tr}(\mathbf{D})/3| \geq |D_{\mathrm{XX}} - \mathrm{Tr}(\mathbf{D})/3| \geq |D_{\mathrm{YY}} - \mathrm{Tr}(\mathbf{D})/3|$ [14]. The three eigenvalues describe diffusion along the three orthogonal directions that define the PAS, with D_{ZZ} corresponding to eigenvalue furthest way from the isotropic average of $\mathbf{D}$, and D_{YY} the closest eigenvalue. Imposing an axial symmetry constraint ($D_{\mathrm{YY}} = D_{\mathrm{XX}}$), we can rewrite Eq. 2.4 as

$$\mathbf{D}^{\mathrm{PAS}} = \begin{pmatrix} D_{\perp} & 0 & 0 \\ 0 & D_{\perp} & 0 \\ 0 & 0 & D_{\|} \end{pmatrix} , \tag{2.5}$$

where $D_{\|} = D_{\mathrm{ZZ}}$ and $D_{\perp} = D_{\mathrm{YY}} = D_{\mathrm{XX}}$ are the axial and radial eigenvalues. The radial and axial diffusivities can be combined to define an alternative parametrization

$$\mathbf{D}^{\mathrm{PAS}} = D_{\mathrm{iso}} \left[\mathbf{I} + D_{\Delta} \begin{pmatrix} -1 & 0 & 0 \\ 0 & -1 & 0 \\ 0 & 0 & 2 \end{pmatrix} \right] , \tag{2.6}$$

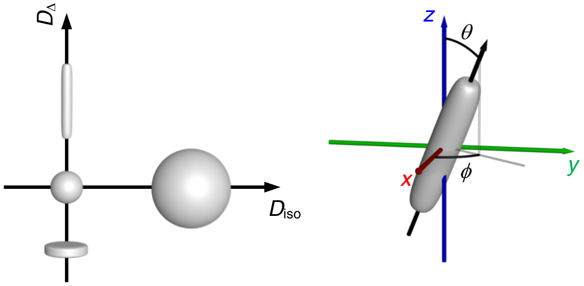

Figure 2.3: Quantitative measures of diffusion tensor size D_{iso}, shape D_Δ, and orientation (θ, ϕ). The D_{iso} and D_Δ parameters inform on the magnitude and anisotropy of the underlying diffusion process. Prolate, isotropic, and oblate tensors are characterized by $D_\Delta > 0$, $D_\Delta = 0$, and $D_\Delta < 0$, respectively. The polar θ and azimuthal ϕ parametrize the orientation of the diffusion tensor relative to the laboratory frame of reference.

where $\mathbf{I}$ is the identity matrix and

$$D_{\text{iso}} = \frac{\left(D_{\|} + 2D_{\perp}\right)}{3}\,, \tag{2.7}$$

$$D_\Delta = \frac{1}{3D_{\text{iso}}}\left(D_{\|} - D_{\perp}\right) \in [-0.5, 1]\,. \tag{2.8}$$

The D_{iso} parameter corresponds to the average across eigenvalues and represents an isotropic diffusivity while the D_Δ parameter informs on the anisotropy of the diffusion process. Oblate, spherical, and prolate diffusion tensors yield $D_\Delta < 0$, $D_\Delta = 0$, and $D_\Delta > 0$, respectively.

2.2.2 Tensor Orientation

The orientation of the PAS relative to the laboratory frame of reference can be expressed as a product of consecutive rotations [15, 16]. Starting from an axisymmetric tensor initially aligned with the laboratory frame, rotations along the y- and z- axes of the laboratory frame

$$\mathbf{D} = \mathbf{R}_z(\phi) \cdot \mathbf{R}_y(\theta) \;\cdot \mathbf{D}^{\text{PAS}} \;\cdot \mathbf{R}_y^{\text{T}}(\theta) \cdot \mathbf{R}_z^{\text{T}}(\phi) \tag{2.9}$$

yield a non-diagonal tensor

$$\mathbf{D} = D_{\text{iso}}\left[\mathbf{I} + D_\Delta \begin{pmatrix} l_x^2 - 1 & 3l_xl_y & 3l_xl_z \\ 3l_yl_x & l_y^2 - 1 & 3l_yl_z \\ 3l_zl_x & 3l_zl_y & l_z^2 - 1 \end{pmatrix}\right]\,, \tag{2.10}$$

whose orientation is defined in terms of azimuthal ϕ and polar θ angles by a set of direction cosines

$$\begin{aligned} l_x &= \cos\phi\sin\theta \ , \\ l_y &= \sin\phi\sin\theta \ , \\ l_z &= \cos\theta \ . \end{aligned} \tag{2.11}$$

The set of $(D_{\text{iso}}, D_\Delta, \theta, \phi)$ parameters provides a complete description of an axisymmetric diffusion tensor with each parameter characterizing a separate aspect of the tensor geometry; D_{iso} and D_Δ describe the size and shape of $\mathbf{D}$, while the (θ, ϕ) angles describe its orientation. Figure 2.3 illustrates the parametrization of $\mathbf{D}$ according to the various $(D_{\text{iso}}, D_\Delta, \theta, \phi)$ measures.

2.3 Capturing heterogeneity with Diffusion Tensor Distributions

Biological tissues comprise different types of cells arranged in a wide array of structures. Given that the typical diffusion MRI experiment requires tens to hundreds of milliseconds to encode the signal for diffusion and that the free diffusion coefficient of water is on the order of $D_0 \approx 10^{-9}\ \text{m}^2\text{s}^{-1} = 1\ \mu\text{m}^2\text{ms}^{-1}$ [17, 18], each water molecule has time to explore a micrometre-scale environment. Different sub-ensembles of water molecules are thus expected to interact with distinct macromolecules and partially permeable membranes, and to reside in intra- or extra-cellular environments of varying geometry [19, 20]. This implies a complex diffusion process that reflects the underlying tissue heterogeneity.

To model diffusion within tissues it is useful to picture the underlying structure as a collection of independent microscopic environments. Each microenvironment is interpreted as a segment of coherent tissue whose structure is characterized by a local $\mathbf{D}$ [11, 21]. Within this approximation, the composition of a given voxel is captured as an ensemble of microscopic diffusion tensors $\mathbf{D}$, as illustrated in Figure 2.4, and quantified by a continuous diffusion tensor distribution (DTD) [11, 22]. The DTD provides a simple, yet experimentally accessible, representation of the underlying heterogeneity and allows the resolution of microscopic tissue environments with distinct structural properties.

2.3.1 Distributions of axially symmetric tensors

For simplicity, we hereafter assume axial symmetry of the diffusing medium. This assumption reduces the number of independent elements contained in each $\mathbf{D}$ from six

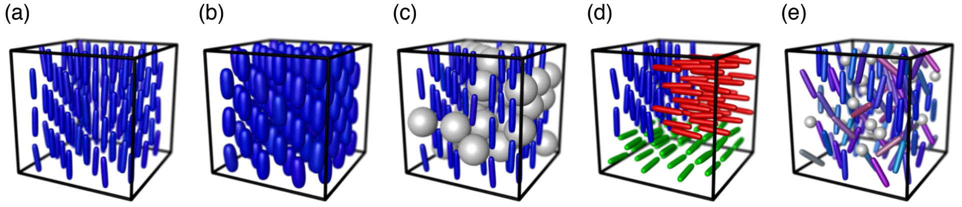

Figure 2.4: Voxel content displayed as an ensemble of microscopic diffusion tensors. The diffusion tensor glyphs are coloured according to: $[\mathrm{R},\mathrm{G},\mathrm{B}] = (1+|D_\Delta|)\cdot(2\,[\cos\phi\sin\theta,\sin\phi\sin\theta,\cos\theta]-1)$. Within a Neuroimaging setting, the voxel contents can be interpreted as representations of aligned white matter (WM) (a), WM demyelination (b), WM inflammation (c), WM three-fibre crossings (d), and tumour infiltration in WM (e).

to four (the four parameters of Section 2.2.2). As shown by Figure 2.3, it is intuitive to parametrize the distribution of tensors with two parameters describing the size and shape, as well as two parameters defining the orientation. The DTD can then be reported as a four-dimensional (4D) distribution of diffusion tensor sizes D_{iso}, shapes D_Δ, and orientations (θ,ϕ), $P(\mathbf{D}) \equiv P(D_{\mathrm{iso}}, D_\Delta, \theta, \phi)$, normalized as

$$\int_0^\infty \int_{-1/2}^1 \int_0^\pi \int_0^{2\pi} P\left(D_{\mathrm{iso}}, D_\Delta, \phi, \theta\right)\, \sin\theta \,\mathrm{d}\theta\,\mathrm{d}\phi\,\mathrm{d}D_\Delta\,\mathrm{d}D_{\mathrm{iso}} = 1\ . \tag{2.12}$$

There are other options to quantify the shape of $\mathbf{D}$ [16]. Following Ref. [13], we reserve the D_Δ notation for equations and report the tensor shape as $D_\parallel/D_\perp$ in graphs. To map between the two representations one simply uses the relation $D_\parallel/D_\perp = (1+2D_\Delta)/(1-D_\Delta)$. The $P(\mathbf{D})$ notation is used to denote the general DTD and, whenever necessary, we explicitly write the arguments of the distribution to clarify the parametrization in use.

2.3.2 Statistical descriptors of the distribution

One of the main goals of this thesis is to estimate the complete 4D DTD or a 2D size-shape projection of it, $P(D_{\mathrm{iso}}, D_\Delta)$. However, as we shall see in the following sections, the estimation of $P(\mathbf{D})$ from a noisy dataset is a challenging task. This has inspired a number of analysis protocols that target statistical descriptors of $P(\mathbf{D})$ rather than the full distribution itself.

Informative and accessible descriptors include the means

$$\mathrm{E}[x] = \int x\,P(\mathbf{D})\,\mathrm{d}\mathbf{D}\ , \tag{2.13}$$

variances

$$\mathrm{Var}[x] = \mathrm{E}[x^2] - \mathrm{E}[x]^2\ , \tag{2.14}$$

and covariances

$$\mathrm{Cov}[x,y] = \mathrm{E}[xy] - \mathrm{E}[x]\mathrm{E}[y] \ , \tag{2.15}$$

of the various dimensions of the $\left(D_{\mathrm{iso}}, D_{\Delta}^{2}\right)$ space [13]. The integration in Eq. 2.13 spans over the space of axisymmetric positive-semidefinite tensors. Measures such as the mean isotropic diffusivity $\mathrm{E}[D_{\mathrm{iso}}]$ and the mean squared diffusion anisotropy $\mathrm{E}[D_{\Delta}^{2}]$ inform on the average diffusion tensor size and shape. $\mathrm{E}[D_{\mathrm{iso}}]$ is recognized as the classical mean diffusivity [23, 24], while $\mathrm{E}[D_{\Delta}^{2}]$ provides similar information as other anisotropy metrics such as the microscopic anisotropy index (MA)[25], the fractional eccentricity (FE) [26], the microscopic fractional anisotropy (µFA)[27], the anisotropic variance V_{A} and anisotropic mean kurtosis (MKA) [21, 28, 29], and the microscopic anisotropy C_{μ} [11]. Previous works have demonstrated a positive correlation between $\mathrm{E}[D_{\Delta}^{2}]$ and the anisotropy of brain tumour cells [29]. Note that the mean squared anisotropy metric probes the shape of the underlying DTD without the confounding effects of orientation; this is in contrast with the widely-used fractional anisotropy (FA) metric [23, 24], which convolves the effects of anisotropy and orientational order [30–32]. The variance measures, $\mathrm{Var}[D_{\mathrm{iso}}]$ and $\mathrm{Var}[D_{\Delta}^{2}]$, capture the spread in diffusion tensor sizes and shape, while $\mathrm{Cov}[D_{\mathrm{iso}}, D_{\Delta}^{2}]$ carries information about correlations between the isotropic and anisotropic dimensions. $\mathrm{Var}[D_{\mathrm{iso}}]$ in particular has been shown to correlate with cell density heterogeneity in brain tumours [29], and similar metrics have been introduced in the diffusion MRI literature: the isotropic second moment μ_{2}^{iso}[27], the isotropic variance V_{I} and isotropic mean kurtosis (MKI)[28, 29], and the normalized isotropic variance C_{MD} [11].

3 | Diffusion Magnetic Resonance

Diffusion magnetic resonance experiments use magnetic field gradients to encode the signal for information about the translational motion of a selected molecular species. More importantly, different gradient designs can be used to target specific aspects of the translational motion of diffusing molecules. According to Paul Callaghan, the challenge of the experimentalist is then "*(...) to devise the gradient waveform best suited to elucidating the structural and dynamical parameters of interest, and to choose the theoretical framework which most aptly describes that choice*" [2]. This chapter focuses on such challenge. Following a brief introduction to the basic theory of magnetic resonance at the microscopic scale, we show how diffusion Magnetic Resonance (MR) techniques can be used to probe microscopic tissue structure, and elucidate the relationship between the acquired signal and the diffusion tensor distribution approximation introduced in Chapter 2. Special attention is given to experimental protocols that can separate and correlate different properties of microscopic tissue heterogeneity, as approximated by a distribution of MR observables such as nuclear relaxation rates or diffusion tensors.

3.1 Magnetic resonance at the microscopic scale

MR techniques measure the electromagnetic signal resulting from the interaction between an external magnetic field and a sample containing an ensemble of spin-bearing nuclei. The measured signal depends on interactions between the nuclei and external magnetic fields, and local interactions involving magnetic and electric fields originating from the sample's nuclear environment. A quantum-mechanical treatment is therefore needed in order to describe the MR signal in terms of intra- and intermolecular interactions such as chemical shifts, dipole-dipole couplings, and interactions between nuclear quadrupole moments and local electric field gradients [33, 34]. While comprehensive, this quantum picture is not commensurate with the micrometre-scale volume explored by the diffusing molecules throughout the MR experiment. Consequently, we adopt a classical description in which the signal arises from a magnetisation vector $\mathbf{M}(\mathbf{r}, t)$ evolving under the influence of external magnetic fields and locally varying MR observables. The Bloch-Torrey equation gives an accurate microscopic description of the evolution of $\mathbf{M}(\mathbf{r}, t)$ as a function of time t and position $\mathbf{r}$ [35]:

$$\frac{\partial M_x}{\partial t}(\mathbf{r}, t) = \gamma(\mathbf{M} \times \mathbf{B})_x - R_2\, M_x(\mathbf{r}, t) + \nabla \cdot \mathbf{D} \cdot \nabla M_x(\mathbf{r}, t)\,, \tag{3.1}$$

$$\frac{\partial M_y}{\partial t}(\mathbf{r}, t) = \gamma(\mathbf{M} \times \mathbf{B})_y - R_2\, M_y(\mathbf{r}, t) + \nabla \cdot \mathbf{D} \cdot \nabla M_y(\mathbf{r}, t)\,, \tag{3.2}$$

$$\frac{\partial M_z}{\partial t}(\mathbf{r}, t) = \gamma(\mathbf{M} \times \mathbf{B})_z - R_1\, (M_z(\mathbf{r}, t) - M_0(\mathbf{r})) + \nabla \cdot \mathbf{D} \cdot \nabla M_z(\mathbf{r}, t)\,, \tag{3.3}$$

where γ is the gyromagnetic ratio of the investigated nuclear species (typically ^{1}H), ∇ is the gradient operator, $M_0(\mathbf{r})$ is the initial magnetization set by the local nuclear density, and $\cdot$ and $\times$ denote the scalar and cross products, respectively. The system of Bloch-Torrey equations comprises contributions from three distinct physical mechanisms:

- The cross products describe a Larmor precession around an external magnetic field $\mathbf{B}$. The angular frequency of the precession movement is given by $\omega = \gamma B$.
- Relaxation towards an equilibrium state. For reasons that will be elaborated below, we assume that the equilibrium state is defined by a bulk magnetization along the z-axis $\mathbf{M}_{\mathrm{eq}}(\mathbf{r}) = (0, 0, M_0(\mathbf{r}))$. The evolution towards equilibrium is regulated by two relaxation rates; the transverse relaxation rate R_2 describes the decay of magnetization components orthogonal to $\mathbf{M}_{\mathrm{eq}}(\mathbf{r})$, while the longitudinal rate R_1 reflects the relaxation mechanisms influencing the magnetisation components parallel to $\mathbf{M}_{\mathrm{eq}}(\mathbf{r})$.
- Anisotropic diffusion of nuclei as described by a microscopic diffusion tensor $\mathbf{D}$.

In the following sub-sections we explore the effects of each of those terms on the detected magnetisation.

3.1.1 Magnetic field pulses and gradients

The **B** term in the Bloch-Torrey equations describes the various external magnetic field that are used to both create and manipulate the magnetisation vector **M**. Typically, this term comprises a linear combination of static magnetic fields, oscillating magnetic fields in the radio-frequency range, and spatially varying magnetic field gradients.

The magnetisation is typically created by subjecting the sample to a static magnetic field $\mathbf{B}_0$ throughout the entire experiment time. This field defines an equilibrium state in which the sample displays a bulk magnetisation $\mathbf{M}_{\mathrm{eq}}(\mathbf{r})$ along $\mathbf{B}_0$. By convention, the z-axis of the laboratory frame of reference is defined to point in the direction of $\mathbf{B}_0$. The resulting magnetisation is commonly manipulated through the application of oscillating magnetic field pulses $\mathbf{B}_1(\omega)$ with a frequency similar to the Larmor frequency of $\mathbf{B}_0$ ($\omega \approx \omega_0 = \gamma B_0$). Because ω is usually in the radio-frequency range, these magnetic field pulses are referred to as RF pulses. The effects of RF pulses are more conveniently analysed in a frame of reference that rotates around $\mathbf{B}_0$ with a frequency $\omega_0 = \gamma B_0$. When working in the rotating frame, $\mathbf{B}_1(\omega)$ appears stationary and the effect of an RF pulse is then a simple rotation of $\mathbf{M}$ around $\mathbf{B}_1(\omega)$. The RF pulses are traditionally named after the rotation they produce; a 90°_x pulse denotes an RF pulse producing a 90° rotation along the (rotating frame) x-axis.

Spatially varying magnetic field gradients $\mathbf{G}(t)$ are an essential component of diffusion and imaging MR experiments. The gradients are used to label the position of the various nuclei by means of producing a spatially dependent precession frequency

$$\omega(\mathbf{r}) = \gamma B_0 + \gamma \mathbf{G}(t) \cdot \mathbf{r} \,. \tag{3.4}$$

As already mentioned in the beginning of this chapter, the temporal profile of the gradient waveforms $\mathbf{G}(t)$ can be tailored to encode the signal for information about the underlying diffusion processes. Within an MRI setting, magnetic field gradients are used to selectively excite the nuclei within a small region of the sample (voxel). Typical voxel sizes range from millimetre in clinical scanners (*e.g.* $1 \times 1 \times 1$ mm^3) to sub-millimetre in research micro-imaging systems.

3.1.2 Relaxation encoding

The ^{1}H relaxation rates of water molecules are exquisitely sensitive to the molecular composition and structural organization of the local tissue environment. The longitudinal relaxation rate R_1 is highly dependent on dipolar interactions and exchange processes between water and other molecular species [36–38]; R_1 is thus determined by water content, the concentration of other molecular constituents such as proteins or lipids, and water binding [39]. The transverse relaxation rate R_2 is equally sensitive to the local chemical compositions and additionally carries information about micro- and meso-scale tissue structures [40, 41]. Motivated by these relationships, water relaxation rates have been widely used as quantitative markers of tissue composition and structure. [42].

For the particular case of *in vivo* human brain, the measured ^{1}H MRI signal includes contributions from water molecules as well as macromolecules. The nonaqueous ^{1}H signals are observed to decay 100 times faster than the signal of water in tissue [43], and

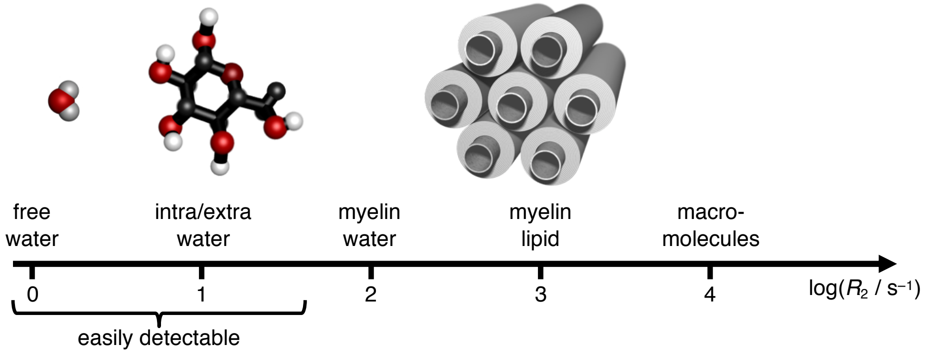

Figure 3.1: Different transverse relaxation R_2 components found in typical healthy brain tissues. The displayed values are based on the data from Refs. [43, 45]. The curly bracket identifies R_2 rates that can be easily detected with MRI protocols allowing for both relaxation- and diffusion-encoding (Paper V).

the measured signal will therefore comprise an insignificant contribution from the fast-relaxing nonaqueous components. Owing to the heterogeneous nature of brain tissues, we can detect microscopic environments with distinct water relaxation properties, see Figure 3.1. Three microscopic components are typically observed in the healthy human brain: a slow-relaxing component corresponding to cerebrospinal fluid, a component with intermediate relaxation corresponding to water in intra- or extracellular environments, and a fast relaxing component attributed to water trapped within the myelin bilayers [44, 45]. To account for tissue heterogeneity, the measured signal is typically expressed in terms of a probability distribution of relaxation rates. MRI methods that can quantify relaxation rate distributions have been classically used to map the volume fraction of myelin water in both healthy [43–45] and diseased [46, 47] human brain, providing estimates that correlate well with histopathology [47].

The scheme of most relaxation techniques can be decomposed into three simple steps: i) create a perturbed state where $\mathbf{M} \neq \mathbf{M}_{\text{eq}}$, ii) allow the magnetisation to evolve towards equilibrium for a given time τ, iii) record the signal. The process is repeated at different times τ in order to record a series of $\mathbf{M}(\tau)$ values modulated by R_1 and/or R_2. Below, we present two basic relaxation measurement methods.

- *Saturation recovery*. This sequence comprises two 90° pulses separated by a time delay τ_{R}. The first 90° pulse brings the equilibrium magnetisation $\mathbf{M}_{\text{eq}} = (0, 0, M_0)$ down to the *x*-*y* (transverse) plane, from which it relaxes back to equilibrium. Due to R_1 relaxation, the evolution towards equilibrium is characterized by a build-up of magnetisation along the *z*-axis (longitudinal direction). A second 90° pulse is applied after a time τ_{R} in order to flip the longitudinal components to the transverse plane, where the signal is detected. The amplitude of the recorded magnetisation is determined as a solution of Eq. 3.3

$$M(\tau_{\mathrm{R}}) = M_0 \left[1 - \exp(-\tau_{\mathrm{R}} R_1)\right] \,. \tag{3.5}$$

The experiment is repeated for different values of τ_{R} and R_1 is determined by fitting Eq 3.5 to the measured data.

- *Spin-echo*. This sequence is based on two different RF pulses: a 90° and a 180° pulses. The 90° pulse rotates the equilibrium magnetisation into the transverse plane, where the signal is left to precess for a time $\tau_{\mathrm{E}}/2$. Due to field inhomogeneities, nuclear populations in different parts of the sample may precess at different speed. This introduces a dephasing that causes the signal to decay at a faster rate than R_2. The application of a 180° pulse inverts the magnetisation and reserves the phase of the various precessing nuclei. If the nuclei are left to precess under the same conditions as before the 180° pulse, the signal will be refocused and an echo will be formed after a time τ_{E}. Neglecting the effects of diffusion, the amplitude of the transverse magnetisation at τ_{E} is modulated by R_2

  $$M(\tau_{\mathrm{E}}) = M_0 \exp(-\tau_{\mathrm{E}} R_2) \,. \tag{3.6}$$

  $M(\tau_{\mathrm{E}})$ is measured as a function of τ_{E} and R_2 is determined by comparing the data to Eq. 3.6.

3.1.3 Diffusion encoding

In diffusion MR experiments magnetic field gradients are used to sensitize the transverse magnetization to the diffusive motion of a selected nucleus. Due to the natural abundance of water in biological tissues and its consequent easiness of detection, the vast majority of *in vivo* MRI literature concentrates on the ^{1}H nuclei of water molecules. The dynamics of the transverse magnetization are well described by Eqs. 3.1 and 3.2, which can be written in the rotating frame of reference as a single compact equation by combining M_x and M_y into a single complex-valued variable $m_{xy} = M_x + iM_y$ [3, 48]:

$$\frac{\partial m_{xy}(\mathbf{r},t)}{\partial t} = -R_2\, m(\mathbf{r},t) - i\gamma \left[\mathbf{G}(t)\cdot\mathbf{r}\right] m(\mathbf{r},t) + \nabla\cdot\mathbf{D}\cdot\nabla m(\mathbf{r},t) \,. \tag{3.7}$$

As discussed in Chapter 2, the translational motion of water molecules within tissues is affected by a variety of semi-permeable membranes that form compartments with barrier spacings ranging from nanometres to micrometres. The effects of interactions with the various membranes on $m_{xy}(\mathbf{r},t)$ can be explicitly modelled by incorporating a series of appropriate boundary conditions into Eq. 3.7 [5, 48]. For simplicity, we instead choose to average these complex effects into a set of effective relaxation rates and apparent diffusion tensors, and approximate the underlying diffusion process as being Gaussian, *i.e.* the diffusion process is functionally equivalent to the one occurring in an unrestricted medium and is described by a Gaussian distribution. Under these assumptions we neglect the explicit effect of the additional boundary conditions and obtain the following solution for Eq. 3.7 [2, 3]

$$m_{xy}(\mathbf{r},t) = m_0(\mathbf{r})\,\exp\left(-R_2\,t - i\mathbf{q}(t)\cdot\mathbf{r} - \int_0^t \mathbf{q}^{\mathrm{T}}(t')\cdot\mathbf{D}\cdot\mathbf{q}(t')\,\mathrm{d}t'\right)\,, \tag{3.8}$$

where $m_0(\mathbf{r})$ is the initial magnetization, and $\mathbf{q}(t)$ is the dephasing vector defined as

$$\mathbf{q}(t) = \gamma\int_0^t \mathbf{G}(t')\,\mathrm{d}t'\,. \tag{3.9}$$

It is important to recognize that Eq. 3.8 provides a coarse approximation that does not explicitly account for the various complex interactions that shape the translational motion of water inside biological tissues. However, this approximation holds for the experimental timings of typical diffusion MRI studies [20], and, as we shall see in the following sections, provides a useful point of departure for the analysis of data from microscopically heterogeneous materials.

The typical diffusion MRI experiment measures the radio-frequency signal generated by the precessing transverse magnetization at a time τ where the echo condition $\mathbf{q}(\tau) = 0$ is fulfilled, thus nulling the imaginary term of Eq. 3.8. The magnetization is measured over a millimetre-scale volume and the resulting signal, $S = \int_V m(\mathbf{r},t)\mathrm{d}\mathbf{r}$, is an average of the contributions from multiple microscopic environments with potentially distinct chemical and structural properties. For a sample comprising non-exchanging microscopic environments with equivalent R_2 rates but distinct $\mathbf{D}$, the macroscopic signal can be written as an integral transformation of $P(\mathbf{D})$ [22]

$$S(\{\mathbf{q}(t)\}_{0\leq t\leq\tau}) = S_0\int\exp\left(-\int_0^\tau \mathbf{q}^{\mathrm{T}}(t)\cdot\mathbf{D}\cdot\mathbf{q}(t)\,\mathrm{d}t\right)\,P(\mathbf{D})\,\mathrm{d}\mathbf{D}\,, \tag{3.10}$$

where S_0 is the signal obtained when $\mathbf{G}(t) = 0$ throughout the time interval $0 \leq t \leq \tau$. Introducing the diffusion-encoding tensor $\mathbf{b}$ [2, 3, 49],

$$\mathbf{b} = \int_0^\tau \mathbf{q}(t)\cdot\mathbf{q}^{\mathrm{T}}(t)\,\mathrm{d}t, \tag{3.11}$$

and assuming that $\mathbf{D}$ is time-independent, we rewrite Eq. 3.10 as

$$\frac{S(\mathbf{b})}{S_0} = \int\exp(-\mathbf{b}:\mathbf{D})\,P(\mathbf{D})\,\mathrm{d}\mathbf{D}\,. \tag{3.12}$$

where $\mathbf{b} : \mathbf{D}$ symbolizes a generalized scalar product between two tensors (Frobenius inner product), $\mathbf{b} : \mathbf{D} = \sum_{ij} b_{ij} D_{ij}$. For homogeneous samples, the $P(\mathbf{D})$ translates mathematically as a delta distribution and Eq. 3.12 yields a mono-exponential signal decay. Conversely, heterogeneous samples exhibiting a dispersion of values along at least one dimension of the DTD space are characterized by a multi-exponential signal decay.

3.2 Multidimensional diffusion encoding

There exists a large number of MR pulse sequences that have been developed to study diffusion in anisotropic systems. A very popular experiment is the pulsed gradient spin-echo (PGSE) sequence displayed in Figure 3.2(a), which was originally introduced by Stejskal and Tanner in 1965 [50]. In such sequence, the signal is encoded for diffusion by a pair of collinear magnetic field gradient pulses that are applied along a single direction. Sequences based on the PGSE design have been the working horse of *in vivo* diffusion MRI studies that have provided valuable contributions to our understanding of the living human brain [32, 51–54]. However, despite its usefulness, the PGSE experiment is known to suffer from poor specificity as the acquired data contains information about an array of distinct structural properties such as restrictions [8], anisotropy [55], and heterogeneity [56]. A particularly relevant limitation of the Stejskal-Tanner experiment is the fact that diffusion encoding along a single direction entangles the contributions from compartment size, anisotropy, and orientation [57, 58], thus preventing the unambiguous quantification of microscopic environments within biological tissues. In this thesis, we use the term *conventional* to refer to protocols where diffusion encoding is exclusively performed by a set of collinear gradients applied over any given single direction.

Several works have demonstrated that the specificity of diffusion MR experiments can be boosted by using more complex schemes where the magnitude and orientation of the magnetic field gradients are varied within a single encoding block [57, 58, 60–64]. Multidimensional diffusion MRI methods [59] in particular, design gradient waveforms that allow for signal acquisition in a multidimensional space of b-tensors with arbitrary shapes in order to isolate or remove specific measures of the underlying DTD [11, 16, 59]. Such methodology bears great resemblance with multidimensional solid-state NMR techniques [65] relying on sample reorientation [66–69] to target particular tensorial aspects of the relevant interaction (*e.g.* chemical shift, dipolar coupling, quadrupolar coupling). An example of a pulse sequence for multidimensional diffusion encoding is presented in Figure 3.2(b); notice that both the conventional and the multidimensional sequences are based on the same spin-echo skeleton, the distinctive trait between the two sequences lies in the design of the gradient waveforms.

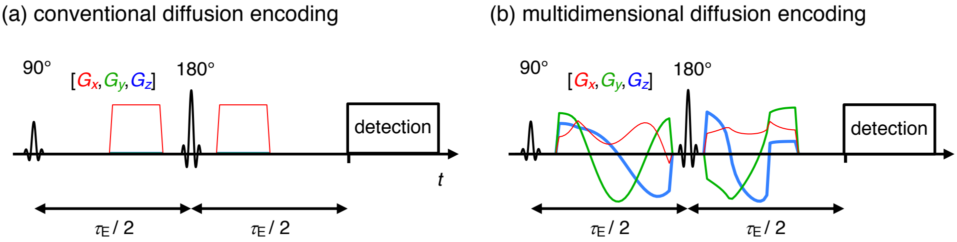

Figure 3.2: MRI sequences for conventional (a) and multidimensional (b) diffusion encoding. The pair of slice-selective 90° and 180° radio-frequency pulses produce a spin-echo that is detected by an image read-out block. The 180° pulse is bracketed by a pair of gradient waveforms (red, green, and blue lines) encoding the signal for information about the translation motion of water molecules. The gradients in (b) are designed to allow a separate control over the trace b, normalized anisotropy b_Δ, and orientation (Θ, Φ) of the diffusion-encoding tensor (b-tensor) [59]. The measured signal can be additionally encoded for transverse relaxation R_2 by varying the τ_E delay.

While multidimensional diffusion encoding schemes can be used to generate symmetric second-order b-tensors with six arbitrary independent elements, only axially-symmetric diffusion-encoding tensors are considered in this thesis. Using a similar convention as that introduced in Chapter 2, we parametrize a given b-tensor by its trace (b), normalized anisotropy (b_Δ), and orientation (Θ, Φ) [58]

$$\mathbf{b} = \frac{b}{3}\left[\mathbf{I} + b_\Delta \begin{pmatrix} l_x^2 - 1 & 3l_xl_y & 3l_xl_z \\ 3l_yl_x & l_y^2 - 1 & 3l_yl_z \\ 3l_zl_x & 3l_zl_y & l_z^2 - 1 \end{pmatrix}\right], \tag{3.13}$$

where the various l_i are defined by Eq. 2.11, with the (θ, ϕ) variables replaced by (Θ, Φ). The b_Δ parameter distinguishes between conventional and multidimensional diffusion schemes; protocols relying on collinear gradient waveforms are limited to a single b-tensor shape ($b_\Delta = 1$), while multidimensional diffusion protocols can sample b-tensors with arbitrary shapes.

The relationship between the b-tensor and $\mathbf{D}$ is made more explicit by expanding the product $\mathbf{b} : \mathbf{D}$ in terms of individual tensor parameters

$$\mathbf{b} : \mathbf{D} = bD_{\mathrm{iso}}[1 + 2b_\Delta D_\Delta P_2(\cos\beta)], \tag{3.14}$$

where $P_2(x) = (3x^2 - 1)/2$ denotes the second Legendre polynomial, and β is the arc-angle between the major symmetry axes of $\mathbf{b}$ and $\mathbf{D}$ given by

$$\cos\beta = \cos\theta\cos\Theta + \sin\theta\sin\Theta\cos(\phi - \Phi). \tag{3.15}$$

As clarified by Eq. 3.14, diffusion encoding with $b_\Delta = 0$ is able to select the effects of D_{iso} on the acquired signal. An entirely different outcome is attained with conventional

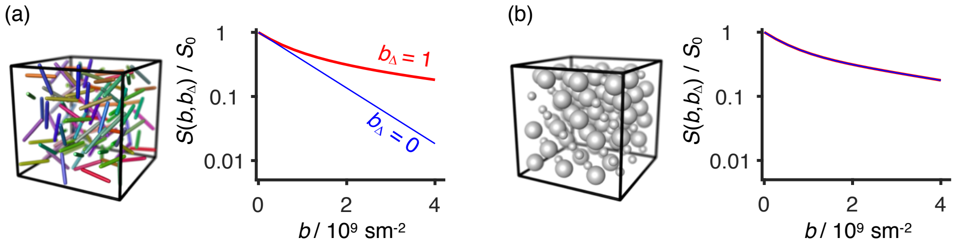

Figure 3.3: Contrast between signals acquired with different b-tensor shapes. The two boxes represent heterogeneous voxels comprising a mixture of randomly oriented identical prolate tensors (a), and a mixutre of two isotropic diffusion tensors of different size (b). The red and blue curves display *in silico* signal data $S(b,b_\Delta)/S_0$ acquired with linear ($b_\Delta = 1$) and spherical ($b_\Delta = 0$) b-tensors, respectively. Despite their obvious structural differences, both voxels yield indistinguishable linearly encoded data. Consequently, both voxels cannot be teased apart when using conventional diffusion encoding schemes. Non-overlapping linearly and spherically encoded signals are observed for the anisotropic system, voxel (a); conversely, the anisotropy of the b-tensor seems to have no effect in the isotropic system, voxel (b).

diffusion encoding ($b_\Delta = 1$), where the effects of D_Δ and orientation are convolved within a single scalar D_{eff} [58]. This shows that b_Δ is a separate experimental dimension that regulates the influence of diffusion anisotropy on the acquired signal.

For completeness, we combine Eqs. 3.14 and Eq. 3.12:

$$\begin{aligned}\frac{S(b,b_\Delta,\Theta,\Phi)}{S_0} = &\int_0^{2\pi}\int_0^{\pi}\int_{-0.5}^{1}\int_0^{+\infty} \exp(-bD_{\text{iso}}[1+2b_\Delta D_\Delta P_2(\cos\beta)]) \\ &\times P(D_{\text{iso}},D_\Delta,\theta,\phi)\mathrm{d}D_{\text{iso}}\,\mathrm{d}D_\Delta\,\sin\theta\,\mathrm{d}\theta\,\mathrm{d}\phi\,.\end{aligned} \tag{3.16}$$

The above equation clarifies that the various dimensions of the acquisition space (b,b_Δ,Θ,Φ) match those of the sought-for distributions $P(D_{\text{iso}},D_\Delta,\theta,\phi)$. Consequently, acquiring data at various combinations of (b,b_Δ,Θ,Φ) facilitates the inspection of specific features of the underlying DTD.

3.2.1 Inferring composition from diffusion-weighted signal patterns

To better understand the advantages of multidimensional diffusion encoding, let us consider the two heterogeneous voxels displayed in Figure 3.3. Despite possessing different microscopic structures, the two voxels yield virtually indistinguishable linearly encoded ($b_\Delta = 1$) signals [57]. However, clearly distinct signals are observed when the effects of diffusion tensor anisotropy and orientation are removed from the data by using a spherical ($b_\Delta = 0$) encoding scheme. Since the left-side voxel does not exhibit a dispersion in D_{iso}, its spherical encoded signal will exhibit the mono-exponential behaviour characteristic of homogeneous samples; in contrast, the right-side voxel com-

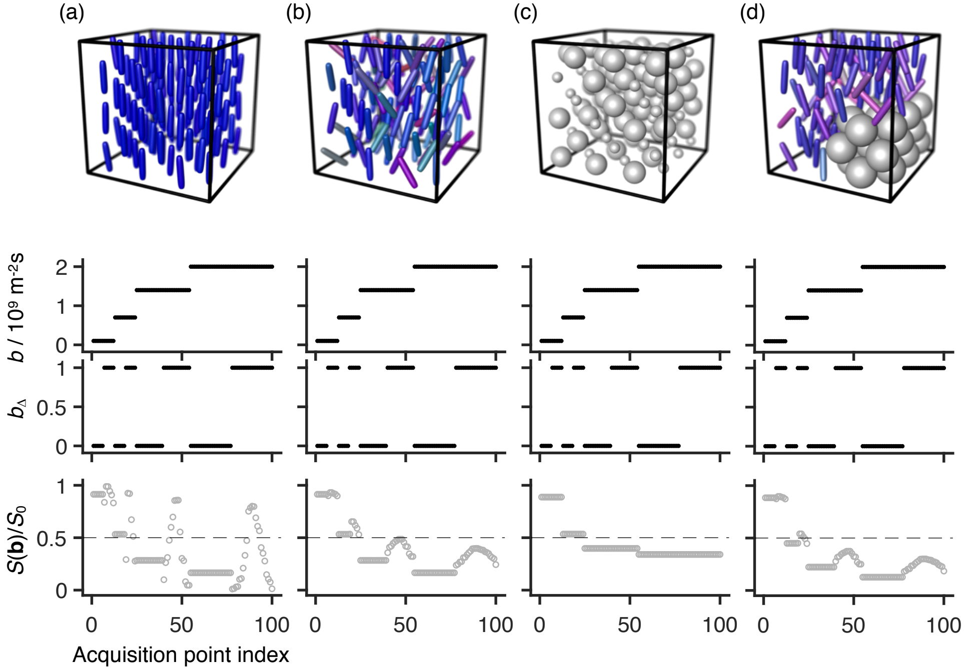

Figure 3.4: *In silico* signal patterns from four voxels with different microscopic compositions. The top boxes display the contents of the various voxels: orientationally ordered anisotropic **D** (a), orientationally disordered **D** (b), mixture of two isotropic **D** with different sizes (c), mixture of orientationally disordered anisotropic **D** with isotropic **D** of larger size (d). The simulated acquisition protocol (black points) and corresponding normalized signal data $S(b)/S_0$ (grey circles) are displayed below. The acquired b-tensor magnitudes b and normalized anisotropy values b_Δ are displayed as a function of the acquisition point index. The $S(\mathbf{b})/S_0$ data is displayed on the same horizontal axis as the acquisition scheme. Notice that clearly distinct signal patterns are observed for the different voxels.

prises isotropic domains characterized by different values of D_{iso}, and is consequently characterized by a multi-exponential spherically encoded signal curve.

Additional insight on the connection between multidimensional diffusion-weighted data and sample structure can be attained from the inspection of Figure 3.4. There, we display the signal patterns simulated for a set of voxels with varying degrees of diffusion anisotropy, orientational order, and D_{iso} heterogeneity. The displayed data was simulated using linear ($b_\Delta = 1$) and spherical ($b_\Delta = 0$) b-tensors of different sizes b and orientations (Θ, Φ). Whenever diffusion anisotropy is present — voxels (a), (b), and (d) — the signal patterns are observed to be sensitive to b_Δ. Signal sensitivity to b_Δ is thus interpreted as the hallmark of diffusion anisotropy. The linearly encoded data of voxel (a) exhibits a sharp "peak pattern" that is modulated by the acquired (Θ, Φ) values. For the orientationally disordered voxels (b) and (d), the signal sensitivity to (Θ, Φ) is reduced and the "peak pattern" observed for voxel (a) is highly attenuated.

The signal sensitivity to b-tensor orientation thus informs on the orientational order of the underlying structure. Notice that voxels (a) and (b) yield the same $(b_\Delta = 0)$ signal pattern, which indicates that they comprise an array of $\mathbf{D}$ with similar isotropic diffusivity $(\mathrm{Tr}(\mathbf{D})/3)$ but different orientations. As voxels (b) and (d) both comprise anisotropic domains with similar degrees of orientational order, their respective $(b_\Delta = 1)$ signals exhibit a similar pattern. The most noticeable difference between the two voxels is the more rapid signal decay registered for voxel (d), consistent with the presence of fast-diffusing isotropic components in voxel (d).

The various patterns observed in Figure 3.4 showcase the specificity of multidimensional diffusion datasets to the sample's structure. The observation of distinctive signal decay curves, specific to the underlying DTD, is crucial to both resolve and quantify microscopic heterogeneity.

3.2.2 Powder-averaging

The dimensionality of Eq. 3.16 can be reduced by rendering the acquired signal insensitive to the details of sample orientation. A practical way to achieve this is to take the arithmetic average of data acquired at a comprehensive set of $\mathbf{b}$ orientations [26, 27, 70]

$$\overline{S}(b, b_\Delta) = \frac{1}{4\pi} \int_0^{2\pi} \int_0^{\pi} S(b, b_\Delta, \Theta, \Phi)\ \sin\Theta\ \mathrm{d}\Theta\ \mathrm{d}\Phi\,. \tag{3.17}$$

This technique has been independently introduced in the field of diffusion MRI as "powder-averaging" [26, 27] and "spherical mean" [71, 72]. In this work we opt for the "powder-averaging" terminology in order to highlight the analogy with solid-state NMR techniques for calculating the spectroscopic line shapes of samples comprising a large number of randomly oriented crystallites (powder samples) [73]. To assure that the powder-averaged signal is indeed rotationally invariant one must probe a sufficient number of uniformly distributed b-tensor orientations. The minimum number of required orientations depends on both the anisotropy of the sample, the anisotropy of $\mathbf{b}$, and the magnitude of the encoding tensor [74].

General analytical expressions of the powder-averaged signal have been derived recently [75]. For axially symmetric $\mathbf{b}$ and $\mathbf{D}$, we can write (Paper I)

$$\frac{\overline{S}(b, b_\Delta)}{S_0} = \int_0^{\infty} \int_{-1/2}^{1} K(b, b_\Delta, D_\mathrm{iso}, D_\Delta) P(D_\mathrm{iso}, D_\Delta)\ \mathrm{d}D_\Delta\ \mathrm{d}D_\mathrm{iso}\,, \tag{3.18}$$

where $P(D_\mathrm{iso}, D_\Delta)$ is a joint distribution of isotropic and anisotropic diffusivities and the inversion kernel is given by [58]

$$K(b, b_\Delta, D_\mathrm{iso}, D_\Delta) = \frac{\sqrt{\pi}}{2} \frac{\mathrm{erf}(\sqrt{3bb_\Delta D_\mathrm{iso} D_\Delta})}{\sqrt{3bb_\Delta D_\mathrm{iso} D_\Delta}} \exp(-bD_\mathrm{iso}[1 - b_\Delta D_\Delta]) \tag{3.19}$$

with erf(·) denoting the error function. The $(D_{\mathrm{iso}}, D_\Delta)$ basis provides a sparse representation of the data wherein each distinct diffusion tensor component gives rise to a 2D delta function that simultaneously describes its size and shape.

The powder-averaged signal measured at a specific b_Δ coordinate can be expressed as the Laplace transform of a 1D distribution of effective diffusion coefficients $\overline{P}(D|b_\Delta)$

$$\overline{S}(b) = S_0 \int_0^{+\infty} \overline{P}(D|b_\Delta)\ \exp(-bD)\,\mathrm{d}D\,. \tag{3.20}$$

The functional form of $\overline{P}(D|b_\Delta)$ is defined as [58]

$$\overline{P}(D|b_\Delta) = \frac{1}{2\sqrt{3D_{\mathrm{iso}}b_\Delta D_\Delta[D - D_{\mathrm{iso}}(1 - b_\Delta D_\Delta)]}} \tag{3.21}$$

in the range

$$\begin{aligned} D &> \min[D_{\mathrm{iso}}(1 - b_\Delta D_\Delta), D_{\mathrm{iso}}(1 + 2b_\Delta D_\Delta)]\ , \\ D &< \max[D_{\mathrm{iso}}(1 - b_\Delta D_\Delta), D_{\mathrm{iso}}(1 + 2b_\Delta D_\Delta)]\ , \end{aligned} \tag{3.22}$$

and $\overline{P}(D|b_\Delta) = 0$ otherwise. According to Eq. 3.21, a single anisotropic component gives rise to a broad $\overline{P}(D|b_\Delta)$ distribution of complex shape whenever data is acquired with a linear b-tensor ($b_\Delta = 1$) [28, 58, 76]. This broadening is a consequence of the entanglement between diffusion tensor anisotropy and orientation expressed by Eq. 3.14.

3.3 Multidimensional relaxation and diffusion correlation MR

Within the field of NMR of porous media, microscopically heterogeneous materials such as food products [77], colloidal systems [78], or porous rocks [79] are typically investigated with multidimensional techniques that combine multiple relaxation- and diffusion-encoding blocks. The acquisition principles of multidimensional correlation experiments are analogous to those of multidimensional NMR spectroscopy methods in which signal data is recorded as a function of different evolution time periods [80]. As illustrated in Figure 3.5, the overall strategy is to apply a sequence of different encoding blocks between magnetization excitation and signal detection in order to establish correlations between different MR observables. The acquired signal data is approximated as a multidimensional integral transform of joint distributions of relaxation rates and/or diffusivities [81], which can then be estimated from the data using non-parametric Laplace inversion techniques [82, 83].

Different number and combinations of encoding blocks can be used depending on which MR observables provide a more detailed characterization of the investigated material, *e.g.* R_1-R_2 [84], R_2-D [85, 86], or D-D [61, 87]. A survey of multidimensional

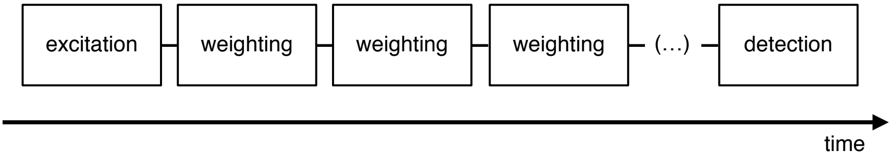

Figure 3.5: Schematic diagram of a multidimensional correlation MR experiment. A variety of relaxation and/or diffusion weighting blocks is applied between an excitation and a signal detection block in order to establish correlations between different MR observables.

Laplace experiments can be found in the reviews by Galvosas and Callaghan [88], and Gladden and Mitchell [89].

To this date, Laplace correlation studies have relied on the Stejskal-Tanner experiment [50] to encode for diffusion. For materials comprising anisotropic domains with multiple orientations, diffusion-encoding along a single direction gives rise to broad distributions of effective diffusivities (see Eq. 3.21), which are not only challenging to retrieve with nonparametric Laplace inversion but also impossible to differentiate from a dispersion in isotropic diffusivities [57]. Consequently, the inherent limitations of the Stejskal-Tanner experiment prevent the discrimination between isotropic and anisotropic contributions to the underlying DTD, as well as the resolution of microscopic environments within heterogeneous anisotropic materials such as biological tissues.

3.3.1 Diffusion tensor correlations

To overcome the difficulties described above, one needs to progress beyond the traditional Stejskal-Tanner design and devise experimental protocols that can disentangle the effects of diffusion tensor size, anisotropy, and orientation. Only by achieving this can one unambiguously resolve and quantify isotropic and anisotropic environments within orientationally dispersed materials.

Previous contributions have shown that the field of multidimensional solid-state NMR spectroscopy is a fertile source of inspiration for the design of diffusion MR methods for investigations of microscopically anisotropic materials [27, 28, 58, 63]. Building upon that line of work, we translated solid-state NMR techniques for correlating isotropic and anisotropic molecular sites [67, 69] into the field of diffusion MR, and devised a family of protocol that quantify microscopic heterogeneity with nonparametric distributions wherein different microscopic environments are resolved based on their respective $(D_{\text{iso}}, D_{\Delta}, \theta, \phi)$ properties. The key insight from solid-state methodology is that isotropic and anisotropic diffusion contributions can be resolved by selectively controlling the influence of diffusion anisotropy and orientation on the acquired signal.

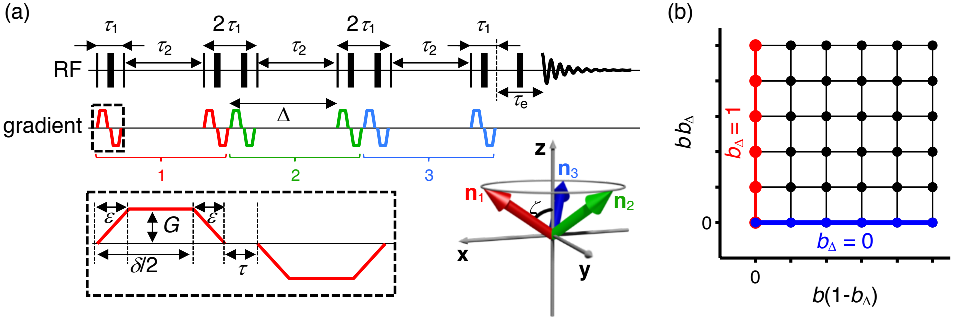

Figure 3.6: Diffusion NMR protocol for establishing correlations between diffusion tensor eigenvalues. (a) Spectroscopic NMR pulse sequence for multidimensional diffusion encoding. The thin vertical lines denote 90°_x radio-frequency pulses while the thick vertical lines represent 180°_y pulses. The dashed box shows a magnification of the first bipolar gradient pulse. The gradient amplitude G and the Δ, δ, τ, and ϵ timings define the magnitude of the b-tensor through Eq. 3.23. The bottom panel illustrates the unit vectors $(\mathbf{n}_1, \mathbf{n}_2, \mathbf{n}_3)$ of the three sets of gradient pulses allowing for diffusion encoding with variable b-tensor anisotropy (b_Δ). The anisotropy of the b-tensor is tuned by changing the angle ζ between the $\mathbf{n}_i$ vectors and the z-axis of the laboratory frame (see Eq. 3.24). (b) Data acquisition protocol for 2D correlations between the size and shape of microscopic diffusion tensors. 2D space spanned by combinations of linear ($b_\Delta = 1$) and spherical ($b_\Delta = 0$) b-tensors. Adapted with permission from Ref. [90] (Paper I).

The proposed protocols rely on signal acquisition in a multidimensional $(b, b_\Delta, \Theta, \Phi)$ space encoding for correlations between the size, shape, and orientation of the underlying $\mathbf{D}$. The resulting information-rich datasets can be converted to DTDs without relying on *a priori* assumptions on the number or properties of the individual microscopic components.

In Paper I, we implemented a spectroscopic version of a diffusion tensor correlation protocol using the triple-stimulated echo sequence introduced in Ref. [91] and displayed in Figure 3.6(a). Diffusion encoding was performed by a sequence of bipolar gradient pulses oriented along three distinct directions $\mathbf{n}_1$, $\mathbf{n}_2$, $\mathbf{n}_3$, defined by three azimuthal angles consecutively rotated by $2\pi/3$ radians and a constant polar angle ζ. The magnitude of the b-tensor is given by [91]:

$$b = 3(\gamma G \delta)^2 (\Delta - \delta/3 - \tau/2 - \epsilon/2 - \epsilon^2/6\delta + \epsilon^3/15\delta^2)\,, \tag{3.23}$$

where G is the gradient amplitude, and Δ, δ, τ, and ϵ are the timing variables defined in Figure 3.6(a). The angle ζ defines the normalized anisotropy of $\mathbf{b}$

$$b_\Delta = P_2(\cos\zeta)\,, \tag{3.24}$$

and assumes a similar role to that of the angle between the main magnetic field and the rotor spinning axis in variable angle spinning techniques [69]. A set of spherical and prolate b-tensors was sampled by varying the gradient amplitude and ζ from $\zeta =$

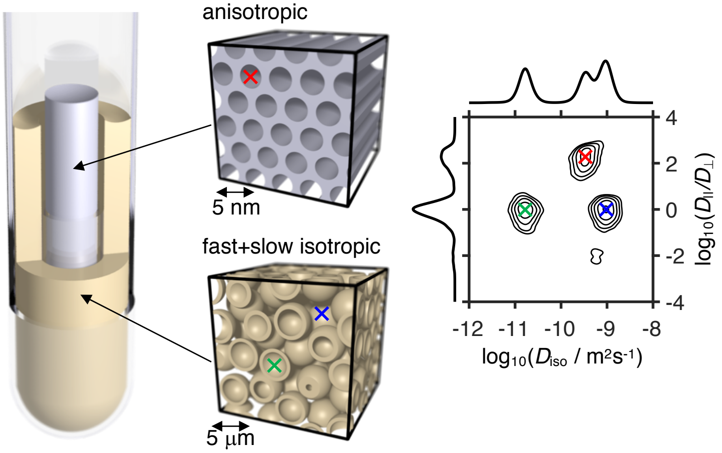

Figure 3.7: 2D size-shape diffusion tensor distribution estimated for a three-component colloidal sample. The sample was assembled by placing a 5 millimetre NMR tube containing a liquid crystal inside a 10 millimetre tube filled with a yeast cell suspension. The two boxes illustrate the anisotropic structure of a single microdomain in the liquid crystal and the microscopic structure of the yeast suspension. The spherical shells represent the cell membranes separating between the intra- and the extra-cellular environments. Diffusion NMR data was acquired from the sample, and then transformed into a 2D distribution of diffusion tensor sizes and shapes (see text for further details). The resulting distribution is displayed as a contour plot of isotropic diffusivities D_{iso}, and axial-radial diffusivity ratios $D_{\|}/D_{\perp}$. The lines above and to the left of the contour plot represent the 1D projections of $P(D_{\mathrm{iso}}, D_{\Delta})$ onto the respective axis. The coloured crosses identify the three microscopic water environments found in the composite sample: anisotropic liquid crystal (red), intracellular yeast (green), and extracellular yeast (blue). Adapted with permission from Ref. [90] (Paper I).

$\arccos(1/3^{1/2}) \approx 54.74°$ ($b_{\Delta} = 0$) to $\zeta = 0°$ ($b_{\Delta} = 1$). The resulting (b, b_{Δ}) grid (see Figure 3.6(b)) allowed for correlations between the size D_{iso} and shape D_{Δ} dimensions of the underlying DTD.

Experimental validation was conducted on a colloidal sample where a central core filled with a liquid crystal in the reverse hexagonal phase [92] is surrounded by a yeast suspension with two isotropic diffusion components (see Figure 3.7). The sample was constructed to mimic the nerve tissue model proposed by Stanisz *et al.* [93]; the liquid crystalline and intracellular yeast components resemble water within axons and glial cells respectively, while the extracellular environment of the yeast suspension replicates the diffusion properties of the extracellular tissue environment. To verify that the protocol can indeed resolve isotropic and anisotropic components even in the presence of orientational disorder, an isotropic orientation distribution was enforced by powder-averaging data collected over multiple (Θ, Φ) orientations. This resulted in a 2D $\overline{S}(b, b_{\Delta})$ dataset that is related to the 2D size-shape $P(D_{\mathrm{iso}}, D_{\Delta})$ distributions via Eq. 3.18. Non-parametric inversion of the data and subsequent estimation of $P(D_{\mathrm{iso}}, D_{\Delta})$ was achieved using the numerical approaches discussed in Chapter 4. The resulting distribution is

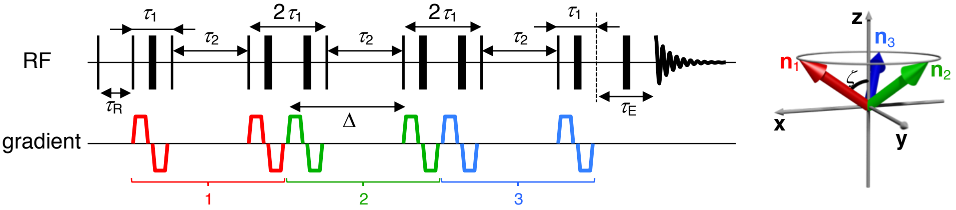

Figure 3.8: Spectroscopic NMR pulse sequence allowing for 6D relaxation- and diffusion-encoding. The sequence consists of an extension of the triple stimulated-echo sequence displayed in Figure 3.6, and follows the same diffusion-encoding strategy. The radio-frequency pulses, gradients, and $(\mathbf{n}_1, \mathbf{n}_2, \mathbf{n}_3)$ unit vectors follow the same labelling of Figure 3.6. Longitudinal R_1 and transverse R_2 relaxation encoding is performed by varying the τ_R and τ_E delays, respectively. The signal is further affected by R_1 and R_2 during the constant τ_2 and τ_1 delays, respectively. Taken with permission from Ref. [98] (Paper II).

shown in Figure 3.7. The inspection of the contour maps reveal that the proposed correlation protocol can indeed resolve and characterize the three components that comprise the composite sample: two isotropic ones at $\log_{10}(D_\text{iso}/\text{m}^2\text{s}^{-1}) \approx -9$ and -11, corresponding to the extra- and intracellular yeast water, as well as an anisotropic component with $\log_{10}(D_\text{iso}/\text{m}^2\text{s}^{-1}) \approx -9.5$ and $\log_{10}(D_\parallel/D_\perp) \approx 2$ originating from the liquid crystal.

3.3.2 Relaxation and diffusion tensor correlations

In deriving Eq. 3.12 we assumed a constant transverse relaxation rate throughout the investigated sample volume. Whenever this assumption does not hold and R_2 differences can be observed between different microscopic environments, the estimated DTD will be biased towards slow-relaxing populations. This issue is particularly relevant for biological samples, as they are known to comprise microscopic tissue environments with distinct R_2 rates [41, 43, 45]. Consequently, one should account for and quantify R_2 heterogeneity in order to estimate accurate component fractions. Moreover, nuclear relaxation rates are known to be exquisitely sensitive to the local chemical composition of tissue [44, 45, 94, 95] and can provide complementary information to diffusion MR experiments [96, 97].

Motivated by the reasons outlined in the previous paragraph, we have extended our DTD correlation approach to a 6D dimensional $(R_1, R_2, D_\text{iso}, D_\Delta, \theta, \phi)$ space (Paper II). To allow for correlations between relaxation rates and diffusion tensors, the pulse sequence introduced in Ref. [91] and used in Paper I was augmented with time periods encoding for transverse and longitudinal relaxation (see Figure 3.8). Diffusion encoding was performed as explained in Section 3.3.1, while R_1- and R_2-weighting was enforced by varying the τ_R and τ_E delays, respectively. Within the DTD approxima-

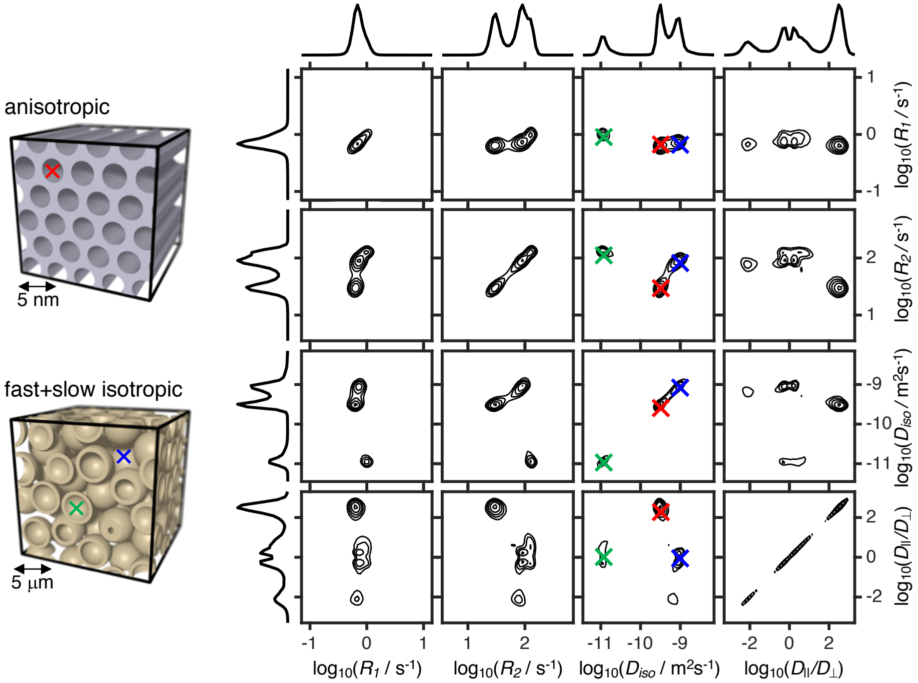

Figure 3.9: 6D relaxation-diffusion distribution $P(R_1, R_2, \mathbf{D})$ estimated for a three-component colloidal sample. The side boxes display the structure of the liquid crystalline solution and the yeast suspension that compose the sample, and are explained in detail in Figure 3.7. The set of 4×4 contour maps displays projections of the full $P(R_1, R_2, \mathbf{D})$ distribution onto 2D subsets of the space defined by longitudinal relaxations R_1, transverse relaxations R_2, isotropic diffusivities D_{iso}, and axial-radial diffusivity ratios $D_{\|}/D_{\perp}$. The black lines on the top and left side of the set display 1D projections of the various distributions $P(R_1, R_2, D_{\mathrm{iso}}, D_{\|}/D_{\perp})$. As in Figure 3.7, the coloured crosses establish the correspondence between sample and distributions components. Adapted with permission from Ref. [98] (Paper II).

tion, the resulting 6D signal writes as

$$\frac{S(\tau_\mathrm{R}, \tau_\mathrm{E}, \mathbf{b})}{S_0} = \iiint [1 - \exp(-\tau_\mathrm{R} R_1)] \exp(-\tau_\mathrm{E} R_2) \exp(-\mathbf{b} : \mathbf{D}) \times P(R_1, R_2, \mathbf{D}) \, \mathrm{d}R_1 \, \mathrm{d}R_2 \, \mathrm{d}\mathbf{D} \,, \tag{3.25}$$

where $P(R_1, R_2, \mathbf{D})$ is the joint probability distribution that captures the underlying R_1, R_2, and $\mathbf{D}$ heterogeneity.

The proof-of-principle experiments were carried out on the colloidal phantom displayed in Figure 3.7. Spectroscopic NMR data was collected for an exhaustive set of $(\tau_\mathrm{R}, \tau_\mathrm{E}, b, b_\Delta, \Theta, \Phi)$ parameters, and subsequently inverted using a non-parametric Monte Carlo inversion algorithm (see Chapter 4 for further details). Figure 3.9 displays the resulting 6D $P(R_1, R_2, \mathbf{D})$ distribution as a set of 2D contour plots. The three components resolved in Figure 3.7 can be also observed in Figure 3.9. The separation and correlation of the various $(D_{\text{iso}}, D_{\Delta}, \theta, \phi)$ dimensions facilitate the resolution of microscopic environments with relaxation rates too similar to be resolved with standard relaxation Laplace protocols. For example, the two yeast components are characterized by similar R_2 rates and thus could not be separated in conventional 1D relaxation measurements [45, 82]. Moreover, the intracellular yeast environments was found to be characterized by a slightly higher R_2 rate when compared to the extracellular environment; this observation indicates an excellent component resolution and is consistent with previous studies relying on constrained fitting approaches to analyse R_2 yeast data [99].

4 | From the signal to diffusion tensor distributions

The diffusion-encoded MR signal of a heterogeneous material can be written as an integral transform of a continuous DTD

$$S(\mathbf{b}) = \int K(\mathbf{b}, \mathbf{D}) P(\mathbf{D}) \, \mathrm{d}\mathbf{D} \,. \tag{4.1}$$

The distribution is mapped into the signal by a generalized kernel $K(\mathbf{b}, \mathbf{D})$ whose functional form is determined by the experimental design and the working approximation. Typically, the kernel is set as $K(\mathbf{b}, \mathbf{D}) = \exp(-\mathbf{b} : \mathbf{D})$. In Chapter 3 we discussed multidimensional encoding strategies that render the acquired $S(\mathbf{b})$ specific to different features of the sought-for DTD. The boost in data specificity was shown to facilitate the quantification of microscopic heterogeneity with $P(\mathbf{D})$ distributions, but the details of the data inversion process were left unclear. Here, we discuss the inverse problem of retrieving microstructural information from a diffusion-encoded signal, describing the most commonly used analysis strategies and limitations inherent to the various inversion methods. The focus is on non-parametric techniques that can either retrieve the full DTD or infer relevant statistical descriptors from it.

4.1 Non-parametric estimation of diffusion distributions

For analysis purposes, it is convenient to approximate the underlying distribution as a sum of N delta functions with unknown "area" w_n. This allows the discretization of Equation 4.1 as

$$S_m = \sum_{n=1}^{N} w_n \exp(-\mathbf{b}_m : \mathbf{D}_n) \,, \tag{4.2}$$

where S_m is the m-th signal amplitude measured with the encoding tensor $\mathbf{b}_m$, and w_n is the weight of the n-th microscopic diffusion tensor $\mathbf{D}_n$. When dealing with real data, each measurement S_m comprises a finite amount of noise ϵ_m. To explicitly account for this fact, Eq. 4.2 is rewritten

$$\mathbf{s} = \mathbf{K} \cdot \mathbf{w} + \boldsymbol{\epsilon}, \tag{4.3}$$

where $\mathbf{w}$ denotes the $N \times 1$ sought-for probability vector, $\mathbf{s}$ is the column vector containing the M signal amplitude measurements, and $\mathbf{K}$ is the $M \times N$ kernel matrix whose elements are defined by the exponential term in Eq. 4.2. The vector $\boldsymbol{\epsilon}$ describes the experimental noise from each of the M measured datapoints.

The presence of noise advises against attempts to search for the exact solution of Eq. 4.2. Instead, a proposed solution should misfit the primary data by an amount consistent with the noise, *i.e.* we seek for a solution $\mathbf{w}$ such that $||\mathbf{s} - \mathbf{K} \cdot \mathbf{w}||_2 \leq \sigma$, where $|| \cdot ||_2$ is the Euclidean norm and σ is the standard deviation of the noise [79, 83, 100]. Unfortunately, the inversion of Eq. 4.3 is an infamous ill-conditioned problem where a small error in $\mathbf{s}$ introduces a large error in the solution $\mathbf{w}$. This means that the same primary noisy dataset accommodates a large number of different solutions within the same noise statistics.

4.1.1 Regularized approaches

The conditioning of the inverse problem can be improved through the incorporation of constraints. A natural and widely used constraint is to restrict the solution space to real and positive w_n weights; this is consistent with the interpretation of $\mathbf{w}$ as a discrete probability density. The estimation of $\mathbf{w}$ is then cast as a non-negative linear least squares (NNLS) problem

$$\mathbf{w} = \underset{\mathbf{w} \geq 0}{\operatorname{argmin}} ||\mathbf{s} - \mathbf{K} \cdot \mathbf{w}||_2 \,, \tag{4.4}$$

The problem stated by Eq. 4.4 can be efficiently solved with classical NNLS algorithms [101]. Distributions estimated from these algorithms will generally comprise a sparse set of delta functions at various $\mathbf{D}_n$ points, and may constitute a reasonable solution provided that the true $P(\mathbf{D})$ is itself composed of a few isolated peaks and that the experimental signal-to-noise ratio (SNR) is sufficiently high [102, 103]. However, the amplitudes and positions of the various peaks are observed to be rather sensitive to noise, and significantly different solutions are typically estimated over different noise realizations. This indicates that a positivity constraint is not by itself a sufficiently strong constraint, and it may be necessary to further reduce the space of possible distributions in order to improve the inversion stability.

A common approach in the analysis of multi-exponential diffusion and relaxation data is to incorporate a regularization term $\Psi(\mathbf{w})$ into the optimization problem

$$\mathbf{w} = \underset{\mathbf{w} \geq 0}{\operatorname{argmin}} \left[\, \|\mathbf{s} - \mathbf{K} \cdot \mathbf{w}\|_2 + \alpha \Psi(\mathbf{w}) \right] \, . \tag{4.5}$$

The regularization term constrains the solution space and its functional form is defined to favour distributions with a pre-defined set of properties; typically, $\Psi(\mathbf{w})$ is defined to promote smoothness [84, 104–106], sparsity [102, 107, 108], or to select the **w** solution yielding the maximum information entropy [109, 110]. Comprehensive reviews on the various regularization strategies used in the MR literature can be found in [82, 83, 111].

It is important to recognize that the regularization term stabilizes the solution but it also increases the residual error of **w**

$$\chi = \|\mathbf{s} - \mathbf{K} \cdot \mathbf{w}\|_2 \, . \tag{4.6}$$

The balance between the least squares misfit and the regularization term is determined by the parameter α. For $\alpha = 0$, Eq. 4.5 is reduced to a standard NNLS problem, and the attained solution will be unstable to noise but also exhibit the maximum accordance to the acquired data. Conversely, a high α parameter results in a stable solution that yields a significantly higher residual error [112]. The selection of an optimal α parameter is then crucial to assure a good trade-off between data consistency and stability.

Although capable of mitigating the influence of noise or reducing over-fitting, regularization strategies yield well-known artefacts that affect the shape of the retrieved distribution [2, 83]. As an example, let us consider the popular ℓ_2 regularization strategy, $\Psi(\mathbf{w}) = \|\mathbf{w}\|_2$. This regularization strategy has been observed to yield an oversmoothed solution whenever the true $P(\mathbf{D})$ distribution is sparse [102, 107], or split intrinsically broad distributions into a series of narrow peaks (the so-called "pearling" artefact) [106]. These artefacts, along with the ill-conditioned nature of Eq. 4.3, should always be kept in mind when attempting to extract relaxation or diffusion distributions form multi-exponential magnetic resonance data.

4.1.2 Monte Carlo approaches

As highlighted in the previous section, conventional regularized approaches estimate a single solution that is selected based on an *ad-hoc* mathematical criterion. However, the estimated solution is just one among the collection of **w** solutions that are consistent with the experimental data. By focusing on a single solution, regularized inversion methods ignore a vast range of plausible **w** and are thus not suitable to assess the uncertainty of the estimated distributions.

The variability between solutions can be explored through a statistical procedure wherein distributions are randomly sampled and compared against the data on the basis

Discretization	1	$S_m = \sum_{n=1}^{N} w_n \exp(-\mathbf{b}_m : \mathbf{D}_n)$	$(\mathbf{s} = \mathbf{K} \cdot \mathbf{w})$
Initialization	2.1	Generate random set $\{\mathbf{D}_n\}_{1 \leq n \leq N_{\mathrm{in}}}$	
	2.2	Obtain **w** via NNLS fit	
	2.3	Save D_n with $w_n > 0$	
Proliferation	3.1	Generate random temporary set $\{\mathbf{D}_n\}_{1 \leq n \leq N_{\mathrm{in}}}$	Repeat N_{p} times
	3.2	Merge temporary and saved sets	
	3.3	Obtain **w** via NNLS fit	
	3.4	Save D_n with $w_n > 0$	
Mutation	4.1	Perturb saved configuration	Repeat N_{m} times
Extinction	4.2	Obtain **w** via NNLS fit	
	4.3	Save D_n with $w_n > 0$	
Final Step	5	Save N configurations with largest weights	

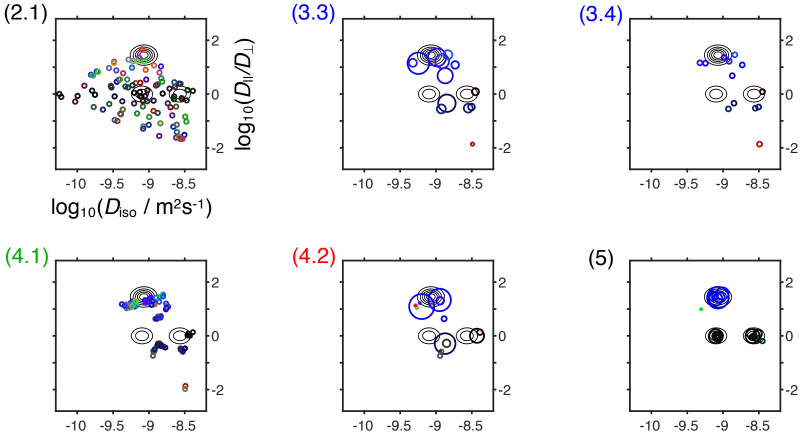

Figure 4.1: Schematic illustration of the Monte Carlo inversion algorithm developed within this thesis. The top panel lists the main steps of the algorithm. The bottom panel shows a practical example of the inversion algorithm for a voxel containing one anisotropic component and two isotropic components with distinct diffusivities. The solutions obtained in different steps of the algorithm are shown as 2D logarithmic scatter plots of isotropic diffusivities D_{iso} and axial-radial diffusivity ratios $D_{\|}/D_{\perp}$. Colour-coding informs on diffusion tensor orientation (θ, ϕ) ($[\mathrm{R}, \mathrm{G}, \mathrm{B}] = [\cos\phi \sin\theta, \sin\phi \sin\theta, \cos\theta] \cdot |D_{\|} - D_{\perp}|/\max(D_{\|}, D_{\perp})$) and circle area is proportional to the weight of the corresponding component. The black contour lines show the ground-truth DTD.

of their residual errors. Distributions yielding a residual compatible with the experimental noise are interpreted as plausible solutions. Sampling and collecting a sufficient

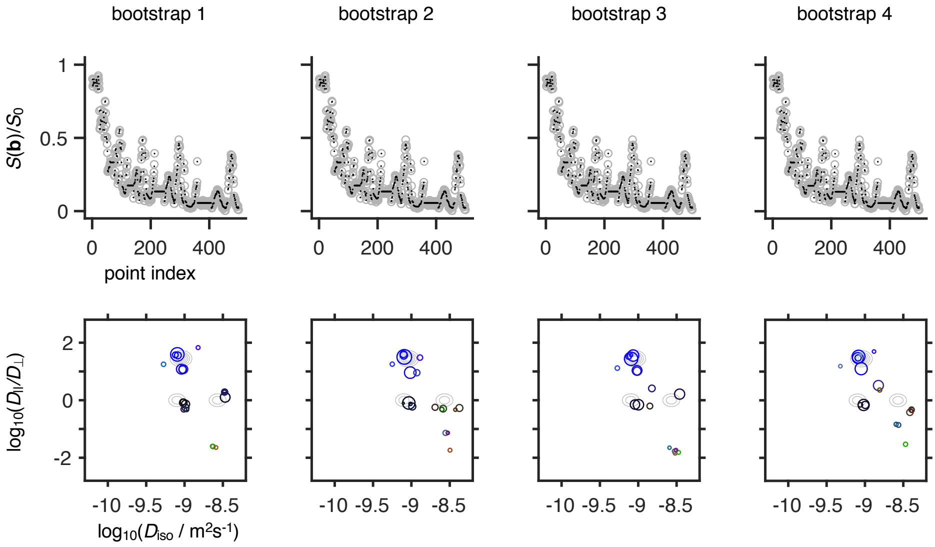

Figure 4.2: Ensemble of DTD solutions estimated for a single *in silico* dataset. Each column displays a Monte Carlo solution obtained with the algorithm schematized in Figure 4.1. The top panel shows the simulated (grey circles) and fitted (black points) normalized signal profiles $S(\mathbf{b})/S_0$. The bottom panel displays the estimated DTD as logarithmic scatter plots similar to the ones introduced in Figure 4.1. Noticeably different solutions are estimated without a marked effect on the fit quality. This evidences the non-unique nature of the inverse problem.

number of plausible distributions generates an ensemble of solutions that reflects the statistical properties of the entire solution space.

Monte Carlo inversion algorithms build on the ideas presented in the previous paragraph in order to quantify the ensemble of solutions that can fit a single noisy dataset. Pioneered by Prange and Song [113, 114], these algorithms were initially developed for the analysis of 1D multi-exponential R_2 relaxation data. An efficient Gibbs sampler was used to generate an ensemble of solutions that was subsequently converted into an ensemble of scalar properties and used to estimate uncertainty metrics. Unfortunately, the proposed sampler has yet to be extended to higher dimensional problems. A practical Monte Carlo approach has been more recently proposed for the analysis of D-T_2 correlated data [115]. Bootstrap data resampling was combined with a standard Laplace inversion algorithm [105] in order to estimate an ensemble of distributions and derive confidence intervals. While individual bootstrapped solutions were observed to comprise several spurious peaks, averaging the distinct solutions allowed the estimation of a smooth distribution with no discernible artefacts. Moreover, bootstrapping was shown to provide an effective method of stabilizing the inversion.

In this thesis, we extend the Monte Carlo analysis to up to six-dimensional correlation spaces. Papers II and IV provide a detailed description of a Monte Carlo algorithm that was specially designed for the analysis of high-dimensional relaxation-diffusion correlated datasets. As a non-limiting example, let us consider an implementation of the algorithm for 4D diffusion tensor correlated data; this particular example is schematized in Figure 4.1. The continuous DTD is approximated as a set of N discrete configurations $\{\mathbf{D}_n\}_{1\leq n\leq N}$ and their respective weights $\{w_n\}_{1\leq n\leq N}$. A plausible solution $\{w_n, \mathbf{D}_n\}_{1\leq n\leq N}$ is estimated using a stochastic iterative procedure in which configurations are continuously sampled in a random fashion, fitted to the data using the classical active-set method described by Lawson and Hanson in [101], and compared with previously generated configurations on a basis of lowest residual sums of squares. Ensembles of plausible discrete distributions are subsequently generated by simply repeating the stochastic inversion procedure (Papers III and V) or using bootstrap with replacement (Papers I, II, IV, and VI).

Figure 4.2 displays individual Monte Carlo solutions estimated with the proposed algorithm. Owing to the non-unique character of Eq. 4.3, noticeably different solutions are obtained without a clear effect on the fitting quality. The individual Monte Carlo solutions are also characterized by the presence of spurious components that disappear upon computing the average of the various bootstraps. This behaviour is in agreement with the results of de Kort *et al.* [115].

4.1.3 Ensembles of statistical descriptors

The multiplicity of Monte Carlo solutions characterizes the uncertainty of the inverse problem. However, it may prove challenging to either capture or visualize the wealth of information contained within the ensembles of distributions, a problem that is accentuated in high-dimensional correlation spaces. A practical solution to this problem was suggested in [113], where functionals were used to map each Monte Carlo distribution into scalar quantities. Ensembles of physically relevant quantities such as porosity or fraction of bound fluid were shown to provide useful insight into the statistical properties of the ensemble of distributions.

Here, we follow a similar approach to the one explained in the previous paragraph, and convert each Monte Carlo solution to a set of statistical descriptors quantifying the means $\mathrm{E}[x]$, variances $\mathrm{Var}[x]$, and covariances $\mathrm{Cov}[x,y]$ of the various dimensions of the distribution space. This procedure is illustrated in Figure 4.3, where the $\mathrm{E}[D_{\mathrm{iso}}]$, $\mathrm{E}[D_{\Delta}^2]$, $\mathrm{Var}[D_{\mathrm{iso}}]$, $\mathrm{Var}[D_{\Delta}^2]$, and $\mathrm{Cov}[D_{\mathrm{iso}}, D_{\Delta}^2]$ descriptors are computed from an ensemble of DTD solutions. The ensembles of statistical descriptors are compactly visualized as a set of histograms. Inspection of the width of the histogram distributions reveals that different descriptors carry different uncertainties; in particular, it is observed that $\mathrm{Var}[D_{\Delta}^2]$ and $\mathrm{Cov}[D_{\mathrm{iso}}, D_{\Delta}^2]$ have a higher uncertainty when compared to the remaining parameters. This observation is in agreement with previous studies [13],

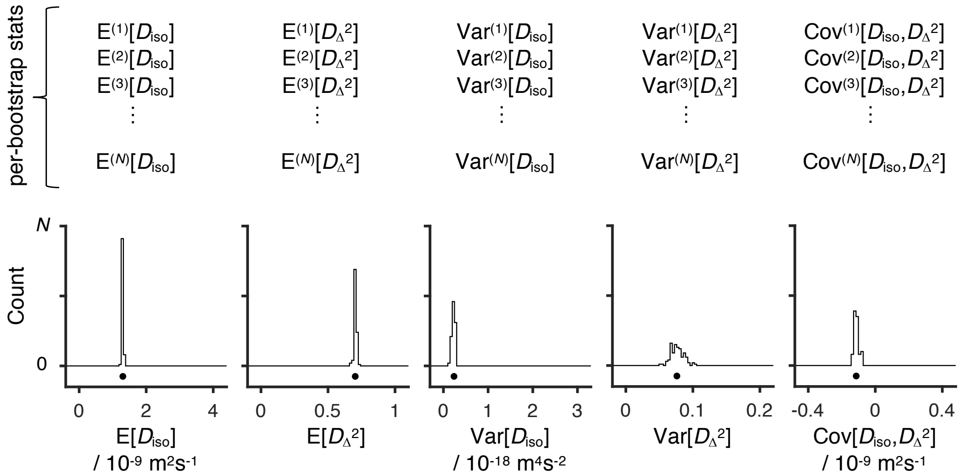

Figure 4.3: Ensembles of statistical descriptors estimated from the ensembles of DTD solutions. Each Monte Carlo DTD is converted to a set of statistical descriptors such as the mean E[*x*], variance Var[*x*], and covariance Cov[*x*,*y*] of isotropic diffusivities D_{iso} and squared normalized diffusion anisotropy D_{Δ}^2. The ensembles of statistical descriptors can be compactly displayed as histograms. For the purpose of calculating parameter maps, it is convenient to reduce the ensembles of statistical descriptors to a single average measure (as estimated from the median). The black dots under the histograms indicate the median of the corresponding statistical descriptor ensemble.

and suggests that different descriptors require different SNR ratios in order to be accurately quantified, *i.e.*, we expect that a higher amount of noise will have a more adverse effect on $\mathrm{Var}[D_{\Delta}^2]$ and $\mathrm{Cov}[D_{\mathrm{iso}}, D_{\Delta}^2]$ than on $\mathrm{E}[D_{\mathrm{iso}}]$, $\mathrm{E}[D_{\Delta}^2]$, and $\mathrm{Var}[D_{\mathrm{iso}}]$.

4.2 Avoiding the ill-conditioned inverse problem: the cumulant expansion

The challenges posed by the inversion of Eq. 4.3 have motivated the development of signal inversion techniques that obviate the need to estimate the full underlying distribution. It turns out that a rather straightforward alternative — the method of cumulants — is based on one of the most basic and overused elements of any physicist's toolkit: the Taylor expansion. The method of cumulants expands the logarithm of the signal in powers of the relevant experimental variable and relates different elements of the series to specific features of the underlying distribution [116–118]. To understand this approach, it is instructive to consider the cumulant expansion of Eq. 3.20 [21, 27]

$$\ln\left(\frac{\overline{S}(b)}{S_0}\right) = -b\overline{D} + \frac{1}{2}b^2\mu_2 - \frac{1}{6}b^3\mu_3 + \cdots . \tag{4.7}$$

The parameters $\overline{D}$, μ_2, and μ_3 correspond to the mean, variance, and skewness, respectively, of $\overline{P}(D|b_\Delta)$ and are defined by

$$\overline{D} = \int_0^{+\infty} D\,\overline{P}(D|b_\Delta)\mathrm{d}D\,, \tag{4.8}$$

and

$$\mu_n = \int_0^{+\infty} (D-\overline{D})^n\,\overline{P}(D|b_\Delta)\,\mathrm{d}D \quad \text{for } n \in \{2,3\}\,. \tag{4.9}$$

Eq. 4.7 clearly shows that different cumulants affect the signal over different ranges of b. At low b-values, the first cumulant dominates and $\ln(\overline{S}/S_0)$ is well captured by a straight line whose slope is equal to $-\overline{D}$. At higher b, the width and then the asymmetry of $\overline{P}(D|b_\Delta)$ become more relevant due to the b^2 and b^3 terms, respectively.

The various terms of the cumulant expansion can be estimated by regressing Eq. 4.7 onto the acquired data. Since different cumulants provide quantitative measures of different aspects of the underlying distribution, this approach allows us to quantify microscopic heterogeneity without having to explicitly address an ill-conditioned inverse problem.

4.2.1 The two-term cumulant expansion and the gamma distribution approximation

In practice, the cumulant expansion is truncated at a given term before being fit to the signal. As different cumulants describe different features of the distribution, the truncation process defines which subset of the information contained within the full distribution is carried to the analysis process. The question then arises of where to truncate Eq. 4.7.

A two-term expansion provides the simplest cumulant-based model capable of quantifying the non-monoexponential signal decay curves measured for heterogeneous media [119, 120]. The first cumulant captures the initial slope of $\ln\overline{S}(b)/S_0$ and is identified as the mean isotropic diffusivity introduced in section 2.3

$$\overline{D} = \mathrm{E}[D_{\mathrm{iso}}]\,. \tag{4.10}$$

For the powder-averaged distribution defined in Eq. 3.21, the second cumulant reports on the curvature of the corresponding signal curve and can be written as [16, 121]

$$\mu_2 = \mathrm{Var}[D_{\mathrm{iso}}] + \frac{4b_\Delta^2}{5}\,\mathrm{E}[D_{\mathrm{aniso}}^2]\,, \tag{4.11}$$

where $D_{\mathrm{aniso}} = D_{\mathrm{iso}}D_\Delta$. Eq. 4.11 shows that the initial deviation from monoexponentiality can be related to well-defined statistical measures that inform on the spread of sizes and the mean shape of the microscopic diffusion tensor components. As shown in [27], acquiring data at two different values of b_Δ allows to tease apart the contributions from $\mathrm{Var}[D_\mathrm{iso}]$ and $\mathrm{E}[D^2_\mathrm{aniso}]$.

To terminate the cumulant approximation at the second term is equivalent to considering a normal distribution of diffusivities. Such a distribution yields a non-monotonically decreasing signal curve and comprises negative diffusivities, implying that non-physical negative statistical descriptors might be estimated from a two-term cumulant expansion. To address these undesirable features, it might prove valuable to consider an alternative functional form of $\overline{P}(D|b_\Delta)$. A viable distribution should promote an analytical signal model that is described by a minimal number of parameters [19] and should constrain the solution space to positive diffusivities [118]. The gamma distribution fulfils those requirements and has been shown to provide a suitable alternative to the two-term cumulant approach [122, 123]. Approximating $\overline{P}(D|b_\Delta)$ as a gamma distribution provides a simple signal model [27]

$$\frac{\overline{S}(b)}{S_0} = \left(1 + b\,\frac{\mu_2}{\overline{D}}\right)^{-\overline{D}^2/\mu_2}, \tag{4.12}$$

that can be used to estimate the relevant terms $\overline{D}$ and μ_2. It should be noted that the main objective of the Gamma distribution is to provide a practical way to extract physical parameters by means of devising a representation that does not predict increasing signals at high b-values and that can be used to represent a wide range of diffusion distributions with just two degrees of freedom [123].

Figure 4.4 illustrates some of the limitations of the gamma approach. The gamma approximation can only capture the first two cumulants of $\ln(\overline{S}(b)/S_0)$, which is but a small fraction of the information contained in the original $\overline{P}(D|b_\Delta)$. Whenever the contribution from higher-order terms is non-negligible, systematic deviations are found between the predicted and the measured signal. The differences indicate that the simulated system contains more information than that captured by the first two cumulants. The inability to accurately model the powder-averaged signal introduces significant biases in the estimation of μ_2 and, consequently, on the estimation of $\mathrm{Var}[D_\mathrm{iso}]$ and $\mathrm{E}[D^2_\mathrm{aniso}]$.

4.2.2 Covariance tensor approximation

The covariance tensor approximation provides a tensor-based generalization of the two-term cumulant expansion [11]

$$\ln\left(\frac{S(\mathbf{b})}{S_0}\right) \underset{\mathbf{b}:\langle\mathbf{D}\rangle\to 0}{\simeq} -\mathbf{b} : \langle\mathbf{D}\rangle + \frac{1}{2}\,\mathbf{b}^{\otimes 2} : \mathbb{C}\,, \tag{4.13}$$

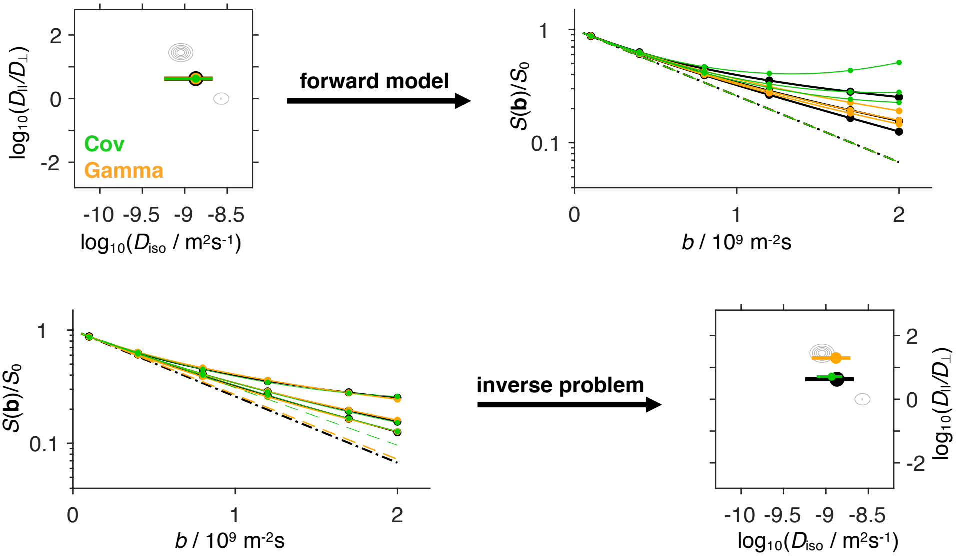

Figure 4.4: Performance of the gamma distribution fitting (orange) and the covariance tensor approximation (green) in capturing the signals/statistical descriptors (black) obtained for a heterogeneous voxel containing both orientationally disordered anisotropic **D** and fast-diffusing isotropic **D**. The performance was assessed for both the forward (top panel) and inverse (bottom panel) problems, using an *in silico* dataset with infinite SNR. The simulated voxel content is equivalent to that shown in Figure 3.4(d). In the signal $S(\mathbf{b})/S_0$ panels, the coloured lines denote the signal decays estimated from the various methods and the coloured dashed lines correspond to their initial slopes, $S(\mathbf{b})/S_0 = \exp(-b\,\mathrm{E}[D_{\rm iso}])$ with $\mathrm{E}[D_{\rm iso}]$ denoting the mean isotropic diffusivity. The different solid lines indicate data simulated with b-tensors of varying anisotropy; from top to bottom: $b_\Delta = 0$, 0.5 and 1. In the square DTD panels, coloured points represent the logarithms of $\mathrm{E}[D_{\rm iso}]$ and (1-2$\sqrt{X}$)/(1-$\sqrt{X}$), where $X = \mathrm{E}[D^2_{\rm aniso}]/\mathrm{E}[D_{\rm iso}]^2$, and the horizontal lines inform on the standard deviation of isotropic diffusivities. The grey contour lines show the ground-truth distribution.

where $\langle\mathbf{D}\rangle$ is the ensemble-averaged diffusion tensor, $\otimes$ denotes the tensor outer product ($\mathbf{b}^{\otimes 2} = \mathbf{b}\otimes\mathbf{b}$), and $\mathbb{C}$ is the fourth-order covariance tensor $\mathbb{C} = \langle\mathbf{D}^{\otimes 2}\rangle - \langle\mathbf{D}\rangle^{\otimes 2}$. The various covariance tensor elements $C_{ij,kl}$ quantify the correlations between the D_{ij} and D_{kl} elements of the microscopic $\mathbf{D}$. While individual elements of $\mathbb{C}$ are challenging to interpret in terms of microscopic structural properties, familiar statistical measures can be obtained through combinations of the elements of $\langle\mathbf{D}\rangle$ and $\mathbb{C}$

$$\mathrm{E}[D_{\rm iso}] = \mathrm{Tr}[\langle\mathbf{D}\rangle]\,/3\,, \tag{4.14}$$

$$\mathrm{Var}[D_{\rm iso}] = \frac{1}{9}(C_{xx,xx} + C_{yy,yy} + C_{zz,zz} + 2C_{xx,yy} + 2C_{xx,zz} + 2C_{yy,zz})\,, \tag{4.15}$$

$$\begin{aligned}\mathrm{E}[D^2_{\text{aniso}}] = \frac{1}{9}\Big[&(C_{xx,xx} + \langle D_{xx}\rangle^2) + (C_{yy,yy} + \langle D_{yy}\rangle^2) + (C_{zz,zz} + \langle D_{zz}\rangle^2) \\ &- (C_{xx,yy} + \langle D_{xx}\rangle\langle D_{yy}\rangle) - (C_{xx,zz} + \langle D_{xx}\rangle\langle D_{zz}\rangle) - (C_{yy,zz} + \langle D_{yy}\rangle\langle D_{zz}\rangle) \\ &+ 3(C_{xy,xy} + \langle D_{xy}\rangle^2) + 3(C_{xz,xz} + \langle D_{xz}\rangle^2) + 3(C_{yz,yz} + \langle D_{yz}\rangle^2)\Big] \,, \end{aligned} \tag{4.16}$$

where $\langle D_{ij}\rangle$ is the ij element of $\langle \mathbf{D}\rangle$. The listed statistical descriptors can be estimated by rearranging Eq. 4.13 as a linear equation system and solving for 28 unknown elements corresponding to the initial signal amplitude S_0 (1 element), $\langle \mathbf{D}\rangle$ (6 independent elements) and $\mathbb{C}$ (21 independent elements) [11]. The elevated number of unknown parameters requires data to be acquired over a wide range of $\mathbf{b}$ sizes, shapes, and orientations in order to reliably estimate $\langle \mathbf{D}\rangle$ and $\mathbb{C}$ from $S(\mathbf{b})$ [11]. Notice that Eq. 4.13 can be recast as a linear system whose least-squares solution can be quickly computed through a matrix pseudoinversion [11].

When using the covariance approximation it is important to consider that a two-term expansion is only valid in the $\mathbf{b} : \langle \mathbf{D}\rangle \to 0$ limit. As shown in Figure 4.4, the covariance tensor approximation provides a rather poor prediction of the measured signal at higher b-values, where clear discrepancies can be observed between the measured and predicted signals. This mismatch between the data and the forward model introduces biases in the quantification of the desired microstructural information (see lower panel of Figure 4.4). Consequently, care has to be taken to exclude data points wherein the covariance approximation no longer holds. Another limitation of the covariance tensor approximation is that it cannot describe systems where higher-than-second-order cumulants are significant, such as anisotropic systems with low orientational order.

4.3 Inversion of noisy datasets

In practical applications, the analysis of the experimental data will be challenged by a finite SNR and a limited number of acquisition points. To acquire an intuitive understanding on the limitations imposed by the experimental noise, let us consider Figure 4.5. There, we display a set of *in silico* datasets at both infinite and finite SNRs. The noise-free dataset was initially simulated (grey circles), and Gaussian distributed noise with an amplitude of 1/SNR (SNR = 30) was subsequently added to generate the noisy dataset (red points). The noise is observed to conceal the overall signal pattern and to consequently hinder the visual inspection of the trends discussed in Section 3.2.1. The effects of noise are most visible in voxel (c), where the small random fluctuations destroy the insensitivity to b_Δ that characterizes the signal patterns of isotropic samples. As differences between data acquired at different b_Δ are interpreted as an indication

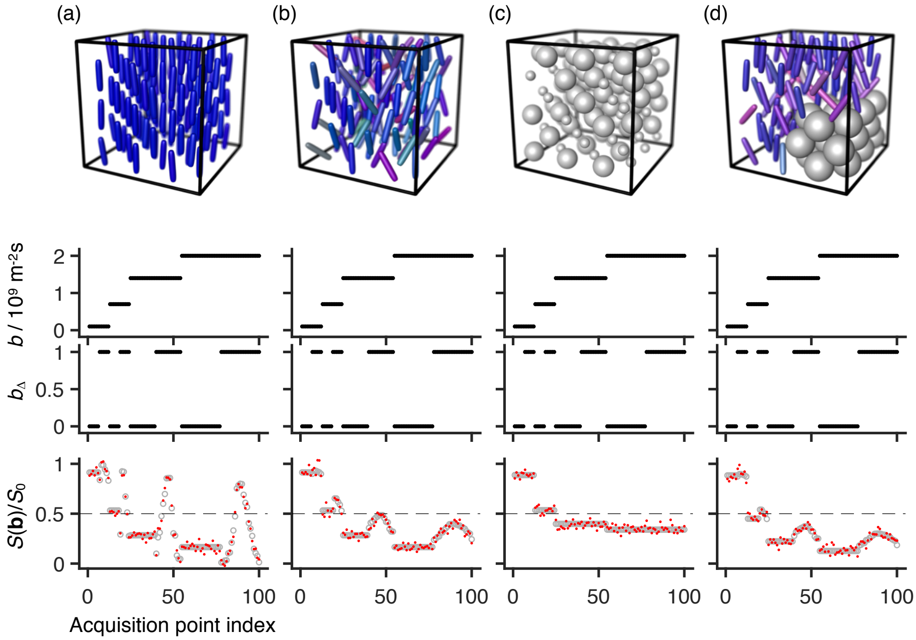

Figure 4.5: *In silico* noisy signal patterns from four voxels with different microscopic compositions. The boxes in the top panel display the diffusion tensor distributions originally shown in Figure ??. Signal data $S(\mathbf{b})/S_0$ with both infinite (grey circles) and finite (red points) SNR was generated using an acquisition protocol comprising 100 *b*-tensors with 4 different traces *b*, and two distinct values of normalized anisotropy ($b_\Delta = 0$ and 1). The noisy dataset was created by adding Gaussian distributed noise with an amplitude of $1/\mathrm{SNR} = 1/30$ to the noise-free data.

of anisotropy, the noise-induced fluctuations are thus expected to introduce a bias towards anisotropic solutions. This effect is similar to the "eigenvalue repulsion" artefact in conventional Diffusion Tensor Imaging (DTI), where experimental noise introduces a discrepancy in the eigenvalues of the voxel-averaged diffusion tensor that gives rise to a positive bias in FA [124].

Multi-exponential signal inversion approaches are widely recognized as being particularly sensitive to both the experimental noise and the sampling density. The already mentioned variability of the solution space is known to increase when either the experimental SNR or the number of acquired data points decrease [113, 125, 126]. Theoretical studies have additionally shown that the ability to resolve different microscopic components is intrinsically linked to the experimental noise [81], and limited SNR values are known to preclude the resolution of microscopic tissue environments with similar MR properties [43, 125]. Within MRI, these observations imply that low spatial resolution and/or long scan times are required in order to retrieve a stable and accurate solution. Consequently, multi-exponential analysis approaches are traditionally considered impractical within a clinical setting.

To assess the performance of our Monte Carlo algorithms within a clinical setting, we investigated the accuracy and precision of their estimations of different statistical descriptors (Paper III). The assessment was performed using a variety of *in silico* datasets probed with a clinically feasible acquisition protocol at both finite ($\mathrm{SNR} = 30$) and infinite SNR levels. The performance of the non-parametric Monte Carlo (MC4D) inversion was compared to that of a gamma distribution approximation (Gamma) and of a covariance tensor approximation (Cov). As expected, the more constrained methods (Gamma and Cov) were observed to be more robust to experimental noise. However, unlike the MC4D approach, they exhibited biases at infinite SNR levels; the Gamma approach was observed to be unsuited to describe systems exhibiting either high anisotropy or high isotropic heterogeneity, and Cov exhibited a particularly poor performance in anisotropic systems with low orientational order. For datasets with limited SNR, MC4D was found to result in significant biases with a clear tendency to overestimate the underlying anisotropy. The finite-SNR biases of MC4D advise against a quantitative interpretation of its derived metrics whenever the primary experimental data is characterized by a low SNR. Despite the finite-SNR biases, MC4D was observed to preserve a good contrast between systems with distinct microstructure and to accurately detect a variation in any of the estimated descriptors. Consequently, MC4D seems to be a feasible choice for comparative clinical studies of tissue microstructure.

5 *In vivo* multidimensional correlation MRI

Papers I and II introduced signal encoding and data inversion strategies to quantify microscopic heterogeneity with non-parametric relaxation and diffusion tensor distributions. Proof-of-principle experiments were carried out on specially tailored colloidal samples using spectroscopic experiments that did not provide spatially resolved information. These works were translated into an *in vivo* imaging setting by redesigning the experimental implementation using smooth gradient waveforms for multidimensional diffusion encoding [15, 127] and single-shot MRI techniques for the signal read-out. This chapter focuses on the results from two experiments designed to resolve sub-voxel environments in living brain tissues: a 4D DTD imaging protocol and a 5D R_2-$\mathbf{D}$ protocol. The diffusion tensor imaging protocol was implemented on a preclinical animal system and used to study the *in vivo* mouse brain. The joint relaxation-diffusion protocol was employed to investigate the sub-voxel composition of living human brain using a standard whole-body clinical scanner.

5.1 Diffusion tensor distribution imaging

In Paper IV, we combined multidimensional diffusion encoding with a spatiotemporal encoding (SPEN) imaging sequence [128–130] to probe the microscopic heterogeneity of *in vivo* brain tissues at sub-millimetre spatial resolution. Data was acquired using b-tensors of varying size b, shape b_Δ, and orientation (Θ, Φ), and then converted into spatially-resolved DTDs using the Monte Carlo algorithm detailed in Section 4.1.2. The proposed acquisition and analysis pipelines were first validated on a set of complementary synthetic samples and then tested on living mouse specimens. In this section we briefly review and discuss the main findings of that work.

5.1.1 Phantom validation

When designing novel MR methods, the use of a standard sample during pulse sequence validation, scanner implementation, and data analysis strategy development is absolutely crucial. Thus, a wide array of samples with stable and well-defined diffusion properties have been engineered to test the precision and accuracy of diffusion MRI protocols [131]. Known in the MRI lingo as "phantoms", these samples can be manufactured from a wide range of materials, assembled to exhibit distinct properties such as a single well-calibrated diffusion coefficient [18, 132], a dispersion of isotropic diffusivities [133–135], or to mimic diffusion in fibrous tissues with both high [136, 137] and low [92, 138–140] orientational order. Anisotropic surfactant solutions in particular have been instrumental in the early development of multidimensional diffusion MR protocols for quantifying the anisotropy of microscopically heterogeneous tissues [27, 58, 63].

To implement and validate the diffusion tensor distribution imaging protocol reported in Paper IV, we used three synthetic phantoms mimicking the diffusion properties of healthy white matter (WM), grey matter (GM), and cerebrospinal fluid (CSF). Pure water and neat liquid hydrocarbon dodecane [18] were used to mimic the fast isotropic diffusion of CSF and slow isotropic diffusion in GM tissues, respectively. Anisotropic water diffusion within WM was emulated by a liquid crystal phantom prepared according to the protocol in [92]. The liquid crystal is nicknamed "hex" due to its reverse hexagonal phase structure wherein water is confined to nanometre-diameter channels in a matrix of detergent and oil.

Figure 5.1 shows the diffusion-encoded SPEN data from four voxels containing hex (two voxels), dodecane, or water. Distinct signal patterns are observed for the different voxels. The signal from the hex voxels is observed to vary significantly with both the anisotropy b_Δ and orientation (Θ, Φ) of the b-tensor, a trend that indicates anisotropic diffusion in orientationally ordered domains. The distinct patterns observed in the hex signals indicate that the two voxels contain data from crystallites oriented along two different directions. The dodecane and water signals are observed to be rather insensitive to both b_Δ and (Θ, Φ), a feature that is consistent with isotropic diffusion. The faster decay with increasing b observed for the water phantom indicates that this sample is characterized by a higher diffusivity. Non-parametric inversion of the data yields DTDs that are consistent with the diffusion features inferred from simple visual inspection of the raw signal patterns. Namely, hex yields a DTD characterized by highly anisotropic components ($\log_{10}(D_\|/D_\perp) \approx 2$) and intermediate-to-low diffusivity ($\log_{10}(D_\mathrm{iso}/\mathrm{m}^2\mathrm{s}^{-1}) \approx -9.4$), dodecane is characterized by isotropic components with intermediate diffusivity ($\log_{10}(D_\mathrm{iso}/\mathrm{m}^2\mathrm{s}^{-1}) \approx -9$), and water gives a DTD composed of fast diffusing isotropic components ($\log_{10}(D_\mathrm{iso}/\mathrm{m}^2\mathrm{s}^{-1}) \approx -8.5$).

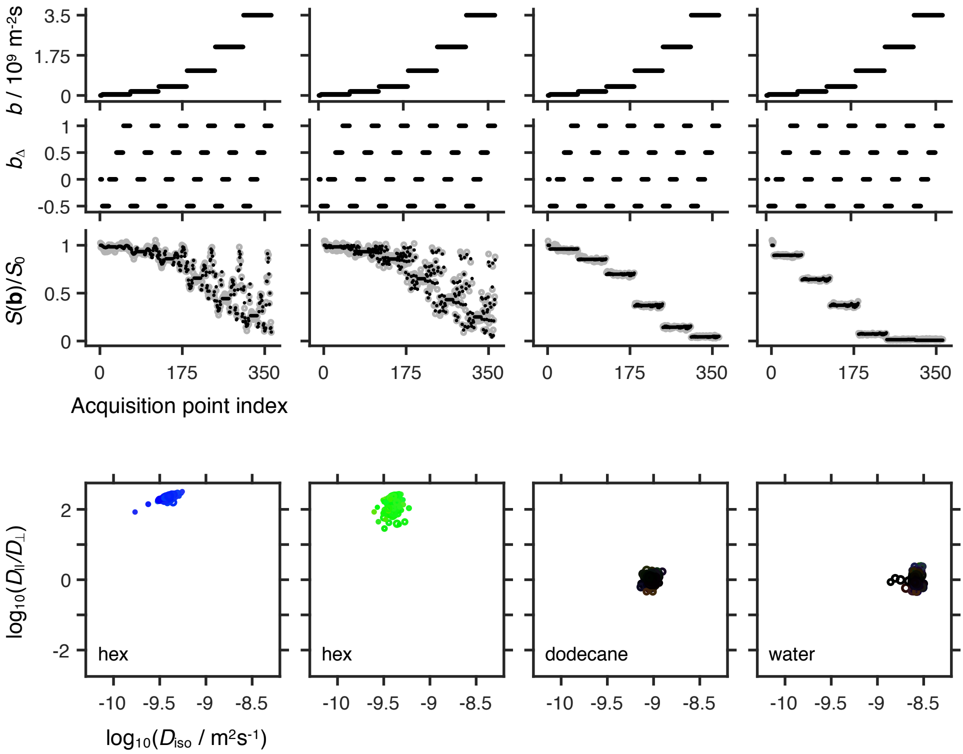

Figure 5.1: Representative 4D diffusion encoded signal data and diffusion tensor distributions (DTDs) for four selected voxels containing hex (column 1 and 2), dodecane (column 3), or water (column 4). (Top panel) Acquisition protocol with b-tensor magnitude b and normalized anisotropy b_Δ displayed as a function of acquisition point index, and corresponding normalized signal data $S(\mathbf{b})/S_0$. In the $S(\mathbf{b})/S_0$ plot, the grey circles and the black points distinguish between experimental and fitted signal profiles, respectively. (Lower panel) DTDs obtained by non-parametric inversion of the signal data in the top panel. The DTDs are displayed as 2D logarithmic scatter plots of isotropic diffusivities D_{iso} and axial-radial diffusivity ratios $D_{||}/D_{\perp}$. The diffusion tensor orientation (θ, ϕ) is color-coded as $[\text{R}, \text{G}, \text{B}] = [\cos\phi \sin\theta, \sin\phi \sin\theta, \cos\theta] \cdot |D_{||} - D_{\perp}|/\max(D_{||}, D_{\perp})$ and the circle area is proportional to the weight of the corresponding component.

As expected, the two hex voxels are distinguished by the orientation of their respective anisotropic components.

The estimated DTDs all feature broad clusters of points. Because the chemical composition and microstructure are constant throughout each phantom, the observed spread of points reflects the uncertainty of the inversion process and the low SNR characteristic of high-resolution diffusion MRI experiments [13]. The low experimental SNR in particular also explains the non-negligible discrepancies between measured and predicted signals observed in the top panel of Figure 5.1.

5.1.2 High-resolution imaging of the living mouse brain

We used the pipelines validated with phantom measurements to acquire and analyse an *in vivo* mouse brain dataset. Pure component voxels containing either WM, GM, or CSF were observed to yield DTDs similar to those obtained for the hex, dodecane, and water phantoms, respectively. Namely, WM is characterized by high $D_{\|}/D_{\perp}$ components, while GM and CSF both exhibit low anisotropy, with CSF being differentiated by its high D_{iso}. While the estimated DTDs were able to accurately capture the diffusion hallmarks of the main components of the healthy living brain, they were also observed to comprise biologically implausible spurious components and to yield significantly higher residuals than the phantom experiments. These undesirable features were attributed to a low SNR (SNR $\approx$ 26) and other uncertainty sources such as motion and eddy current artefacts. Consistent with the findings of Paper III, the higher amount of noise was observed to induce a positive bias in the anisotropy metric.

The voxel-wise DTDs were converted to ensembles of S_0, $\mathrm{E}[D_{\mathrm{iso}}]$, $\mathrm{E}[D_{\Delta}^2]$, $\mathrm{Var}[D_{\mathrm{iso}}]$, $\mathrm{Var}[D_{\Delta}^2]$, and $\mathrm{Cov}[D_{\mathrm{iso}}, D_{\Delta}^2]$ by following the procedure described in Section 4.1.3. For the purpose of calculating parameter maps, it is useful to condense each statistical descriptor ensemble to a single average measure $\langle\cdot\rangle$. The average is measured as a median and not as a mean in order to increase its robustness to outliers. The resulting parameter maps are compiled in Figure 5.2, which also displays the $\langle S_0\rangle$, $\langle \mathrm{E}[x]\rangle$, $\langle \mathrm{Var}[x]\rangle$, and $\langle \mathrm{Cov}[x,y]\rangle$ maps obtained for the diffusion phantoms.

As evidenced by the phantom results, the $\langle \mathrm{E}[D_{\mathrm{iso}}]\rangle$ map distinguishes between environments with a fast mean diffusion and environments with a slow mean diffusion. For the living mouse brain, the overall $\langle \mathrm{E}[D_{\mathrm{iso}}]\rangle$ map was found to be in excellent agreement with mean diffusivity maps estimated from high-resolution DTI protocols [141], and high $\langle \mathrm{E}[D_{\mathrm{iso}}]\rangle$ values were found to correlate well with the expected spatial distribution of CSF. High $\mathrm{E}[D_{\Delta}^2]$ values were concentrated in WM-rich structures such as the cerebellum and the olfactory bulb, while smaller, yet non-negligible, $\mathrm{E}[D_{\Delta}^2]$ values were found spread throughout the brain. This is in contrast with high-resolution DTI studies of the *in vivo* mouse brain, which only report a significant anisotropy in coherently aligned WM tracts [141, 142]. The differences between our method and DTI studies can be explained by the fact that, unlike Fractional Anisotropy (FA), $\mathrm{E}[D_{\Delta}^2]$ quantifies anisotropy independently from orientational coherence, as discussed in Section 2.3.2. However, the existence of a noise induced bias towards anisotropic components makes it unclear if the higher $\mathrm{E}[D_{\Delta}^2]$ values do in fact reflect the tissue properties of the mouse brain. While further work is needed to elucidate this point, microscopic anisotropy has been detected in *ex vivo* GM tissue [26, 139, 143], an observation that supports a widespread non-zero anisotropy.

The (co)variance maps report on intra-voxel heterogeneity. Vanishingly low values

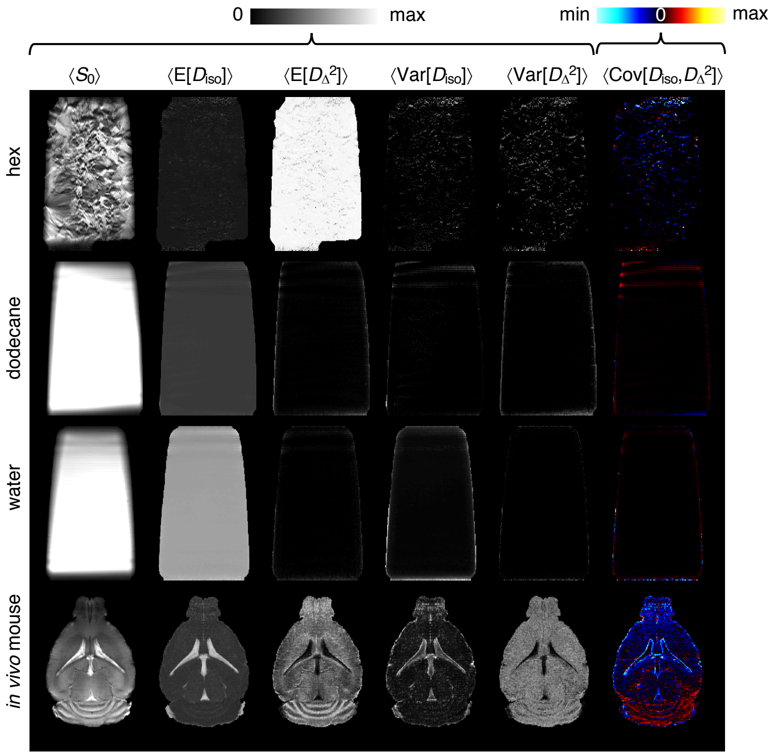

Figure 5.2: DTD parameter maps of phantoms and living mouse brain. Row 1: hex phantom [92] (anisotropic), row 2: dodecane (slow isotropic), row 3: water (fast isotropic), and row 4: living mouse brain. The parameter maps were derived from the 4D diffusion tensor distributions, and inform on the bootstrap averages of different descriptors: total signal amplitude $\langle S_0 \rangle$, and the mean $\langle \mathrm{E}[x] \rangle$, variance $\langle \mathrm{Var}[x] \rangle$, and covariance $\langle \mathrm{Cov}[x,y] \rangle$ of isotropic diffusivities D_{iso} and squared normalized diffusion anisotropy D_Δ^2. The numerical values of the linear color scales are identical to the horizontal axes of the histograms in Figure 4.3.

of $\mathrm{Var}[D_{\mathrm{iso}}]$, $\mathrm{Var}[D_\Delta^2]$, and $\mathrm{Cov}[D_{\mathrm{iso}}, D_\Delta^2]$ are found for the homogeneous phantoms. In the mouse brain, elevated $\mathrm{Var}[D_{\mathrm{iso}}]$ and negative $\mathrm{Cov}[D_{\mathrm{iso}}, D_\Delta^2]$ were detected in voxels containing both GM and CSF. These trends indicate a mixture of slow- and fast-diffusing components [27, 28] wherein low D_{iso} values are correlated with higher values of diffusion anisotropy [13].

To separate the signal contributions from WM, GM, and CSF we sorted the spatially resolved DTD components into three coarse bins named *Thin*, *Thick*, and *Big*. The bin names describe the visual appearance of the corresponding diffusion tensor glyphs; the Thin and Thick bins capture slow-diffusing anisotropic and isotropic components, respectively, and the Big bin selects fast-diffusing components. Figure 5.3 shows the limits and fractional signal contributions of the various bins. The additive color map reveals that binning can demarcate distinct anatomical structures based on their micro-

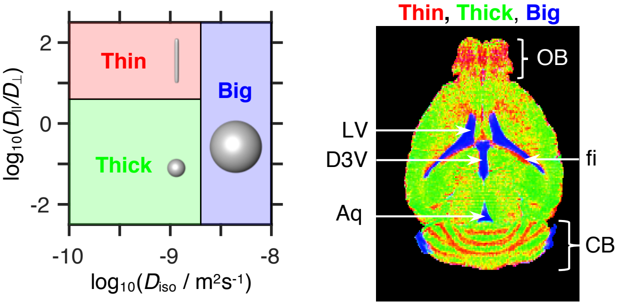

Figure 5.3: Division of the DTD space into the Thin, Thick, and Big bins. The colour-coded composite map shows the signal contributions from the fractional populations in the Thin (red), Thick (green), and Big (blue) bins. Voxels containing more than one fraction are visible as mixed colours, *e.g.* equal proportions of Thin and Thick populations result in a yellow voxel. The various legends identify anatomical features of interest [144]: LV: lateral ventricles, D3V: dorsal third ventricle, Aq: sylvius aqueduct, OB: olfactory bulb, fi: fimbria and CB: cerebellum.

scopic diffusion properties. For example, the Big bin (blue voxels) teases apart CSF-rich areas such as the ventricles (LV and D3V) or the sylvius aqueduct (aq), while the Thin bin (red voxels) captures the fibrous tissues found in structures such as the cerebellum (CB), the fimbria (fi), or the olfactory bulb (OB) [144]. The binning process was also observed to be useful in the detection of WM/GM partial volume effects (yellow voxels) such as those observed at the interface of white and grey matter areas of the cerebellum.

The diffusion properties of the various bin-resolved components can be inspected through mean parameter maps of diffusion tensor size, shape, and orientation (see Figure 5.4). Multiple voxels with low brightness can be found in the Thin $\langle \mathrm{E}[x] \rangle$ maps. This results in a noisy appearance that hinders the analysis of the Thin maps. However, the overall green appearance of the composite map in Figure 5.3 indicates that the darker Thin voxels have a small contribution to the retrieved DTDs. Figure 5.4 additionally shows that the DTD components of the various phantoms fall cleanly within the intended bins (hex – Thin, dodecane – Thick, water – Big), thus providing further evidence that the defined bins can both separate and capture the diffusion properties of WM, GM, and CSF.

5.2 5D relaxation-diffusion correlation MRI

Spectroscopic MR experiments combining both diffusion- and relaxation- encoding have been routinely used since the early 2000s to characterize the microscopic heterogeneity of a wide array of porous materials [85, 86, 112, 145–147]. As explained in Section 3.3, these experiments yield multidimensional correlated datasets that can be converted to joint probability distributions of relaxation rates and diffusivities through

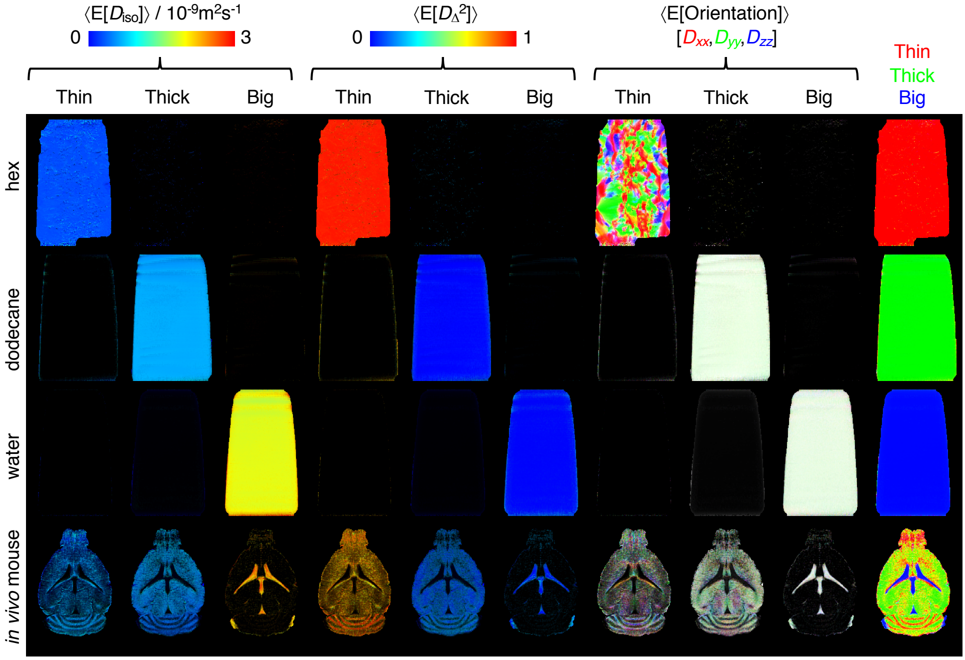

Figure 5.4: Bin-resolved DTD parameter maps of phantoms and living mouse brain. Row 1: hex phantom [92] (anisotropic), row 2: dodecane (slow isotropic), row 3: water (fast isotropic), and row 4: living mouse brain. The parameter maps were derived from the fractional populations in the Thin, Thick, and Big bins defined in Figure 5.3. Columns 1-9 show the per-bin signal fractions (brightness) and per-bin average mean values (color) of isotropic diffusivity ⟨E[D_{iso}]⟩, squared normalized diffusion anisotropy ⟨E[D_Δ^2]⟩, and diffusion tensor orientation ⟨E[Orientation]⟩. The ⟨E[Orientation]⟩ maps are color-coded as [R,G,B] = [D_{xx},D_{yy},D_{zz}]/max(D_{xx},D_{yy},D_{zz}), where D_{ii} are the i-th diagonal elements of the diffusion tensor as measured in the laboratory frame of reference. Column 10 shows colour-coded composite maps of the various bin populations: [R,G,B] = [Thin,Thick,Big].

a non-parametric inversion algorithm [83, 105, 148]. Diffusion-relaxation correlation protocols have been recently combined with imaging pulse sequences and used to investigate the sub-voxel composition of both fixated [149, 150] and living tissues [151]. The combination of diffusion with other MR observables was found to improve the ability to resolve microscopic tissue environments. Despite their improved resolution, these approaches relied on a PGSE experiment for diffusion encoding and thus suffer from the limitations discussed in Section 3.2.

In order to extend relaxation-diffusion correlation MRI protocols to studies of heterogeneous anisotropic materials, we have devised a protocol that resolves microscopic heterogeneity in a five-dimensional space of transverse relaxation rates and axisymmetric diffusion tensors. The method follows the same MR physics as the spectroscopic experiment presented in Paper II and was implemented within a spin-echo with an echo-planar imaging (EPI) read-out [152]. Diffusion encoding was performed with a

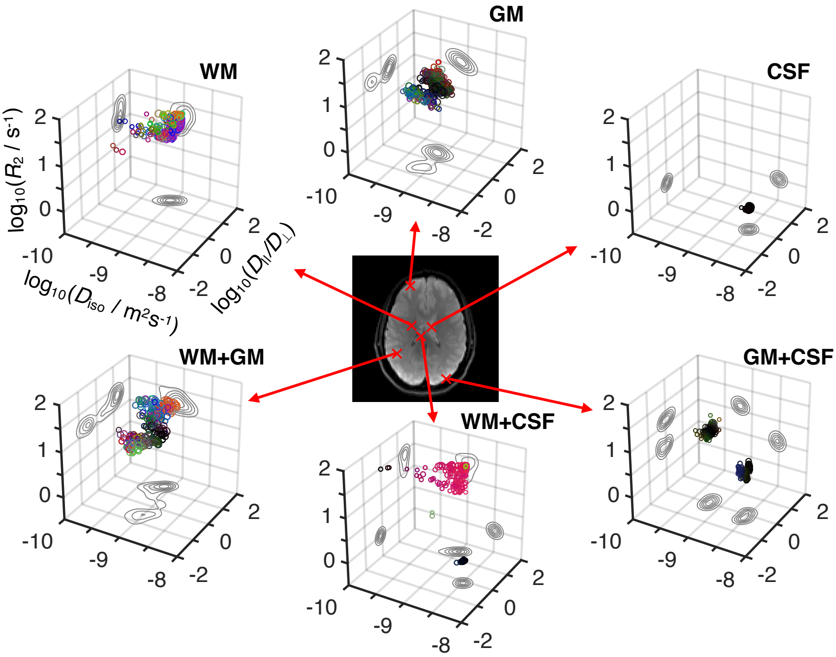

Figure 5.5: 5D R_2-**D** distributions estimated for six representative voxels in the living human brain. The selected voxels contain white matter (WM), gray matter (GM), and cerebrospinal fluid (CSF), as well as binary combinations of the same components: WM+GM, WM+CSF, and GM+CSF. The distributions are shown as 3D logarithmic scatter plot of transverse relaxation rates R_2, isotropic diffusivities D_{iso}, and axial-radial diffusivity ratios $D_{\|}/D_{\perp}$, with circle area proportional to the weight of the corresponding R_2-**D** coordinates. The colour coding is defined as: $[\mathrm{R}, \mathrm{G}, \mathrm{B}] = [\cos\phi \sin\theta, \sin\phi \sin\theta, \cos\theta] \cdot |D_{\|} - D_{\perp}|/\max(D_{\|}, D_{\perp})$, where (θ, ϕ) corresponds to the orientation of each **D**.

set of numerically optimized gradient waveforms [127], and relaxation-weighting was achieved by varying the echo-time (τ_{E}). Images with different b-tensors and τ_{E} were acquired yielding a 5D dataset that was converted to spatially-resolved R_2-**D** distributions using the unconstrained Monte-Carlo algorithm discussed in Section 4.1.2. The spatially resolved R_2-**D** distributions were used to derive a comprehensive set of parameter maps reporting on intra-voxel heterogeneity (Paper V), and to isolate and visualize fibre-specific information on relaxation and diffusion properties (Paper VI).

5.2.1 Voxel-wise distributions

Pure component voxels containing either WM, GM, or CSF are characterized by R_2-**D** distributions that accurately reflect the distinguishing microscopic features of the various tissues (see Figure 5.5). Both WM and GM yield fast-relaxing components ($\log_{10}(R_2/\mathrm{s}^{-1}) > 1$) of low isotropic diffusivity ($\log_{10}(D_{\mathrm{iso}}/\mathrm{m}^2\mathrm{s}^{-1}) \approx -9$), with

WM being differentiated by its high diffusion anisotropy ($\log_{10}(D_{\parallel}/D_{\perp}) > 1$); CSF exhibits slow-relaxing ($\log_{10}(R_2/\mathrm{s}^{-1}) \approx 0$), fast-diffusing ($\log_{10}(D_{\mathrm{iso}}/\mathrm{m}^2\mathrm{s}^{-1}) \approx -8.5$) isotropic components. The distributions obtained for mixed component voxels comprise a linear combination of the R_2-$\mathbf{D}$ properties that tease apart the individual WM, GM, and CSF distributions. For example, a voxel containing both WM and CSF yields a distribution with isotropic fast-diffusing components with low R_2 and anisotropic slow-diffusing components with higher R_2 rates (see WM+CSF distribution in Figure 5.5).

The distributions displayed in Figure 5.5 all feature broad clusters of points that cover a significant range of the R_2-$\mathbf{D}$ space. Similar broad distributions were also observed for discrete component phantoms (see Figure 5.1), where the spread of components was attributed to the inversion and measurement uncertainties. The various sources of uncertainty obscure any subtle differences in R_2-$\mathbf{D}$ properties and challenge the resolution of fine microanatomical details such as those assumed in biophysical models of brain tissue [19, 20, 93, 153–155]. Focusing on the GM voxel of Figure 5.5, we notice a nearly symmetric spread of components around the $\log_{10}(D_{\parallel}/D_{\perp}) = 0$ plane. The bimodal “butterfly” pattern reflects the bias towards anisotropic components discussed in Section 4.3 (Paper III) and gives rise to an overestimation of $\mathrm{E}[D_{\Delta}^2]$.

5.2.2 Parameter Maps

Parameter maps of average statistical descriptors were estimated as described in the previous section. The additional R_2 dimension translates into new descriptors informing on the mean relaxation value $\mathrm{E}[R_2]$, the underlying dispersion in relaxation rates $\mathrm{Var}[R_2]$, and correlations between relaxation and diffusion properties $\mathrm{Cov}[R_2, x]$. It should be mentioned that the $\mathrm{E}[R_2]$ and $\mathrm{Var}[R_2]$ parameters can also be retrieved with classical quantitative MRI protocols [42], or estimated from 1D R_2 distributions obtained through the inversion of multi-echo MRI data [41, 44]. However, the covariance measures require correlations between R_2 and the four distinct parameters of $\mathbf{D}$, and its estimation constitutes a novel contribution of this thesis.

Figure 5.6 displays the various maps computed from the entirety of the R_2-$\mathbf{D}$ space. In line with classical results [30, 42], CSF regions exhibit low $\mathrm{E}[R_2]$ and high $\mathrm{E}[D_{\mathrm{iso}}]$ when compared to WM and GM areas. The $\langle \mathrm{E}[D_{\Delta}^2] \rangle$ allows the distinction between WM (high $\langle \mathrm{E}[D_{\Delta}^2] \rangle$) and GM (low $\langle \mathrm{E}[D_{\Delta}^2] \rangle$) regions. High $\mathrm{E}[D_{\Delta}^2]$ values were found across the expected spatial distribution of WM, even in regions of crossing pathways, where conventional diffusion anisotropy metrics such as FA yield low values. This finding is in agreement with those from previous studies [28, 29, 70, 156], and indicates that — unlike the FA metric [23] — $\mathrm{E}[D_{\Delta}^2]$ measures anisotropy independently of tissue orientational coherence.

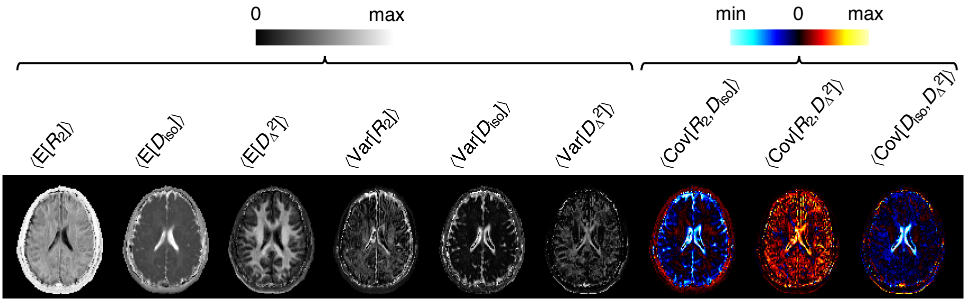

Figure 5.6: Statistical descriptors derived from the 5D relaxation-diffusion distributions $P(R_2,\mathbf{D})$. An ensemble of distinct $P(R_2,\mathbf{D})$ solutions was used to calculate the means E[x], variances Var[x] and covariances Cov[x,y] of all combinations of transverse relaxation rate R_2, isotropic diffusivity D_{iso}, and squared anisotropy D_Δ^2. The ensemble averages of the various statistical descriptors, ⟨E[x]⟩, ⟨Var[x]⟩ and ⟨Cov[x,y]⟩, are displayed as parameter maps.

While mean parameter maps were observed to provide valuable insight on the main features of the human brain, they cannot quantify a dispersion of sub-voxel components. To investigate microscopic heterogeneity we resort to the various (co)variance elements. For example, the high $\mathrm{Var}[D_{\mathrm{iso}}]$ values found in voxels surrounding the ventricles indicate mixtures of CSF with other components. GM+CSF voxels can be distinguished from WM+CSF voxels by inspecting the $\mathrm{Var}[D_\Delta^2]$ descriptor, which captures heterogeneous voxels comprising both isotropic and anisotropic components. As CSF and GM are both characterized by a low anisotropy, partial volume effects involving these two components do not result in a significant dispersion in D_Δ^2; conversely, WM+CSF voxels are characterized by elevated values of $\mathrm{Var}[D_\Delta^2]$ and finite negative values of $\mathrm{Cov}[D_{\mathrm{iso}},D_\Delta^2]$, as lower isotropic diffusivities are correlated with higher values of diffusion anisotropy (see WM+CSF distribution in Figure 5.5). Consequently, the low $\mathrm{Var}[D_\Delta^2]$ in the lateral ventricular regions suggests the existence of deep gray matter, while a combination of high $\mathrm{Var}[D_\Delta^2]$ and negative $\mathrm{Cov}[D_{\mathrm{iso}},D_\Delta^2]$ identifies WM+CSF voxels.

Following the same procedure used for the analysis of the mouse brain dataset, we classified the detected R_2-$\mathbf{D}$ components into the Thin, Thick, and Big bins. In Figure 5.7, we compare the spatial distribution of the various bin populations with a high-resolution R_1-weighted image segmented in three tissue classes: WM, GM (cortical+deep), and CSF [157]. The binning of components based on their $(D_{\mathrm{iso}},D_\Delta)$ properties is observed to agree well with the R_1-based segmentation, with the Thin, Thick, and Big populations resolving the signal contributions from WM, GM, and CSF. While deep GM was for the most part captured by the Thick bin, certain structures such as the pallidum or the thalamus were observed to yield anisotropic components that fall within the Thin bin (Paper V). This is attributed to the presence of myelinated axons within those structures.

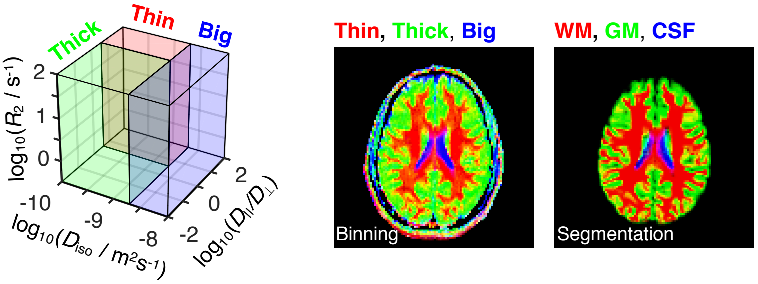

Figure 5.7: Division of the R_2-**D** space into the Thin, Thick, and Big bins. The contributions from different bins are compared with a high-resolution R_1-weighted image segmented into three different tissues: white matter WM, grey matter GM (cortical+deep), and cerebrospinal fluid CSF [157]. Colour-coded composite maps display the spatial distribution of the bin fractions, [R,G,B] = [Thin,Thick,Big], and of the segmentation labels, [R,G,B] = [WM,GM,CSF].

Figure 5.8 shows the bin-resolved $\langle \mathrm{E}[R_2] \rangle$, $\langle \mathrm{E}[\mathrm{Orientation}] \rangle$, and per-bin signal contribution maps for a number of selected slices. The displayed average mean parameter maps provide a clean visualization of the relaxation and diffusion properties of distinct microscopic tissue environments. For example, the $\langle \mathrm{E}[\mathrm{Orientation}] \rangle$ map allows us to easily tease out the orientation of WM pathways close to the cortical surface. Also noteworthy is the detection of sub-voxel mixtures of anisotropic (Thin bin) and isotropic (Thick bin) components within the thalamus (arrows in the first row of Figure 5.8). This observation is in agreement with previous studies, where a reduced microscopic anisotropy was observed in the thalamus and interpreted as a consequence of mixtures between WM and GM [28].

The $\mathrm{E}[R_2]$ values of WM components were found to be higher than those of cortical GM voxels, see the first two columns of Figure 5.8. This behaviour is in accordance with classical relaxometry literature [42] and was consistently observed across the entire dataset, even in voxels containing WM+GM mixtures (Paper V). It is important to note that the subtle differences between the R_2 rates of WM and GM are challenging to separate with classical 1D distribution protocols [43, 45]. Here, the resolving power is boosted by the correlations across the various dimensions of the diffusion space, which spread the various sub-voxel components across a vast high-dimensional space [79, 88]. Different R_2 populations were also detected within the Thin and Thick bins. The fast-relaxing voxels found in the midbrain region of the Thin $\langle \mathrm{E}[R_2] \rangle$ maps identify the myelinated axons that transverse the *globus pallidus*, an iron-rich basal ganglia structure that is characterized by particularly high R_2 rates [158, 159]. Within the Thick bin, we find significant $\mathrm{E}[R_2]$ differences between cortical (lower R_2) and subcortical (higher R_2) GM structures.

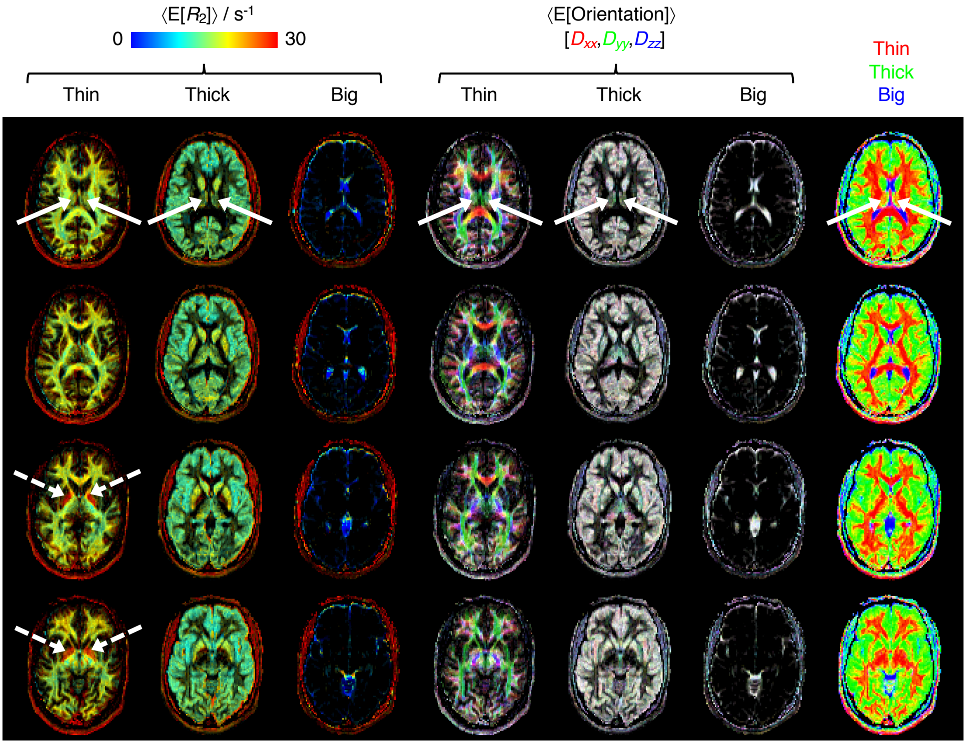

Figure 5.8: Parameter maps derived from the R_2-**D** bins defined in Figure 5.7. Columns 1-6 show the per-bin average mean values (colour) of transverse relaxation rate $\langle \mathrm{E}[R_2]\rangle$ and diffusion tensor orientation ⟨E[Orientation]⟩. The ⟨E[Orientation]⟩ maps are color-coded as [R,G,B] = $[D_{xx},D_{yy},D_{zz}]/\max(D_{xx},D_{yy},D_{zz})$, where D_{ii} are the i-th diagonal elements of the laboratory-framed average diffusion tensors estimated from the various distribution bins. Column 10 shows colour-coded composite maps of the various bin populations: [R,G,B] = [Thin,Thick,Big]. The various arrows identify anatomical regions singled-out in the main text.

5.2.3 Orientation Distribution functions

The various maps of Figure 5.8 show that the Thin bin provides a clean 3D mapping of sub-voxel fibrous tissues. Here, we concentrate on the solutions that are contained within that bin, $\{w_n, D_{\|,n}, D_{\perp,n}, \theta_n, \phi_n\}_{\text{Thin}}$, and inspect their orientation-specific properties.

The orientational information of fibres is often described by a smooth Orientation Distribution Function (ODF) $P(\theta,\phi)$ that is visualized as a directionally coloured surface with a local radius given by $P(\theta,\phi)$ [160, 161]. To obtain a smooth ODF, we convolve $\{w_n\}_{\text{Thin}}$ with a Watson distribution kernel [162, 163]:

$$P(\theta,\phi) = \zeta \sum_{i\in\text{Thin}} w_i \exp\left[\kappa\left(\boldsymbol{\mu}(\theta,\phi)\cdot\mathbf{u}_i\right)^2\right] , \tag{5.1}$$

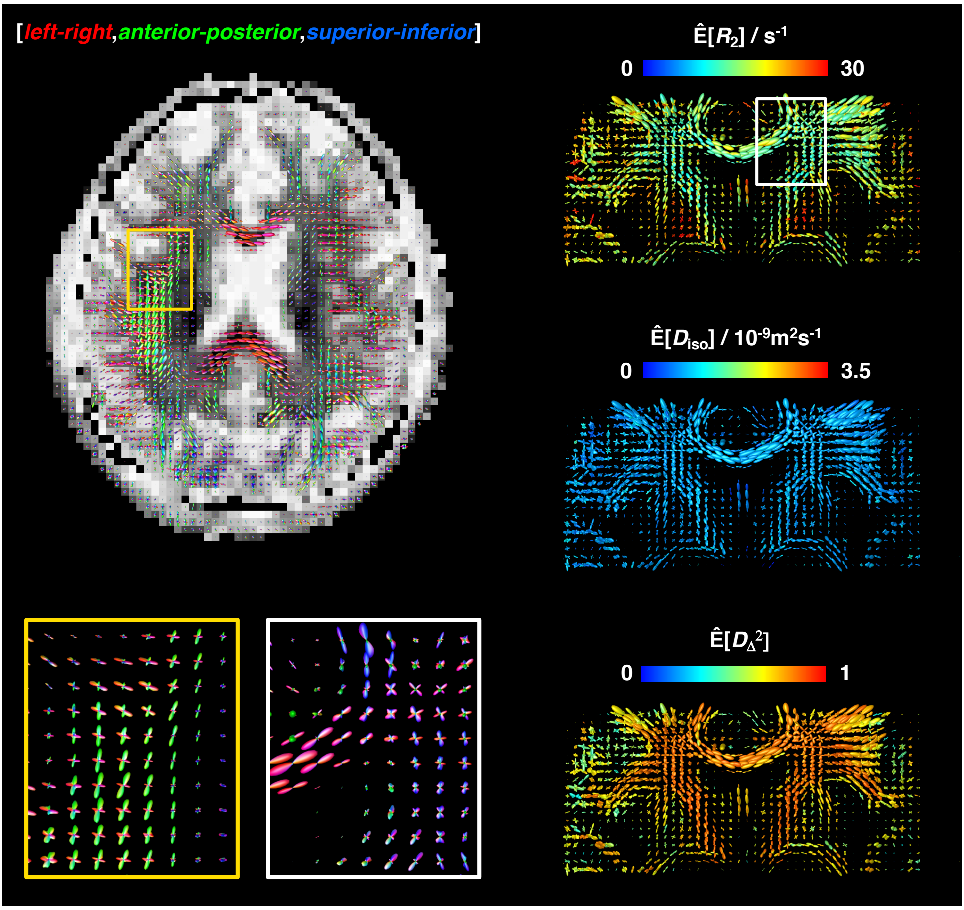

Figure 5.9: Per-voxel Orientation Distribution Functions (ODFs) estimated from bin-resolved R_2-**D** distributions. All ODFs were calculated following a separation and selection of components within the Thin bin, see Figure 5.7. (Left panel) Arrays of ODF glyphs color-coded as $[\mathrm{R},\mathrm{G},\mathrm{B}] = [\mu_{xx},\mu_{yy},\mu_{zz}]$, where μ_{ii} are the elements of the unitary vector $\boldsymbol{\mu}(\theta,\phi)$ (see Eq. 5.1 for more details). The sets of ODF glyphs are superimposed on a grey-scaled map that shows the signal contributions from the Thick and Big populations. The zoom-ins in the lower part of the panel offer a more detailed look into selected fibre-crossing regions. The spatial location of the rightmost zoom-in is indicated by the white square at the top right coronal map. (Right Panel) ODF maps coloured according to the orientation-specific mean values of transverse relaxation $\hat{\mathrm{E}}[R_2]$, isotropic diffusivity $\hat{\mathrm{E}}[D_{\mathrm{iso}}]$, and squared normalized diffusion anisotropy $\hat{\mathrm{E}}[D_\Delta^2]$ (see Eq. 5.2 for more details).

where $\mathbf{u}_i$ is the unit vector describing the orientation of the i-th discrete solution, $\boldsymbol{\mu}(\theta,\phi)$ is the unit mean direction vector of the Watson kernel, and ζ is a normalization constant. The variable κ denotes a concentration parameter that regulates the amount of orientation dispersion around $\boldsymbol{\mu}(\theta,\phi)$. A different ODF was calculated for each bootstrap solution, and a final $P(\theta,\phi)$ was then estimated as the average of the per-boostrap ODFs.

The left panel of Figure 5.9 shows the directionally coloured ODFs estimated for an axial slice and zoom-ins on two selected crossing regions. The estimated ODFs were able to capture major WM tracts, and were observed to resolve crossings between more than two fibre populations (Paper VI). More importantly, anatomically plausible ODFs were also estimated for heterogeneous voxels containing not only WM, but also GM and CSF; the low fraction of Thin components did not affect the orientation of the corresponding ODF lobes.

The comprehensive correlations across the R_2-$\mathbf{D}$ space allow us to investigate the relaxation and orientation properties along different fibre orientations. To do so, we assign mean values of R_2, D_{iso}, and D_Δ^2 to the various coordinates of the smooth ODF space. Taking R_2 as an example, the mean value per orientation, $\hat{\mathrm{E}}[R_2](\theta,\phi)$, is calculated as

$$\hat{\mathrm{E}}[R_2](\theta,\phi) = \frac{\zeta \sum_{i \in \mathrm{Thin}} w_i R_{2,i} \, \exp\left[\kappa \left(\boldsymbol{\mu}(\theta,\phi) \cdot \mathbf{u}_i\right)^2\right]}{P(\theta,\phi)} \,. \tag{5.2}$$

ODF glyphs coloured according to $\hat{\mathrm{E}}[R_2]$, $\hat{\mathrm{E}}[D_{\mathrm{iso}}]$, and $\hat{\mathrm{E}}[D_\Delta^2]$ are shown in Figure 5.9. Note that ODFs close to ventricles do not reveal an increased $\hat{\mathrm{E}}[D_{\mathrm{iso}}]$ or decreased $\hat{\mathrm{E}}[R_2]$, which indicates a successful separation of distinct tissue components.

Previous *in vivo* MRI works have shown that fibres orientated along different directions are characterized by distinct R_2 rates [159, 164, 165]. However, the maximum difference between fibre-specific R_2 rates was of approximately 2.5 s^{-1} [164], a value that is significantly smaller than the uncertainty of the estimated distributions. Consequently, no interdependence between orientation and R_2 can be immediately discerned in the $\hat{\mathrm{E}}[R_2]$-coloured ODFs displayed in Figure 5.9.

6 | Concluding remarks

This thesis introduces a novel diffusion MRI framework to resolve and characterize microscopic tissue environments in a multidimensional space of isotropic diffusivities D_{iso}, normalized diffusion anisotropy values D_Δ, and $\mathbf{D}$ orientations (θ, ϕ). The developed acquisition and analysis protocols are inspired by signal encoding and data inversion strategies from solid-state NMR spectroscopy and multidimensional Laplace NMR. Gradient waveforms designed according to the principles of multidimensional solid-state NMR enable the separation and correlation of different dimensions of the $(D_{\mathrm{iso}}, D_\Delta, \theta, \phi)$ space. Ensembles of DTDs are then retrieved from the correlated datasets using Monte Carlo inversion algorithms from Laplace NMR. The attained distributions allow for the quantification of microscopic tissue heterogeneity without relying on assumptions about the number or properties of the underlying microscopic environments.

The development of this protocol spanned a number of papers dealing with the theoretical aspects of the framework (Papers I and II), the assessment of the inversion algorithm (Paper III), and the translation to *in vivo* studies (Papers IV, V and VI). The individual conclusions from those papers are summarized below:

I Signal acquisition strategies of multidimensional solid-state NMR protocols for isotropic-anisotropic correlations can be transferred to the field of diffusion MR, and used to design protocols establishing correlations between diffusion tensor eigenvalues. The resulting data can be used to estimate non-parametric 2D distributions wherein the microscopic environments of heterogeneous anisotropic materials are resolved on the basis of the size and shape of their respective diffusion tensors.

II The multidimensional diffusion encoding strategies introduced in Paper I can be combined with relaxation encoding. This allows one to resolve microscopic heterogeneity on a six-dimensional space that combines the intuitive relation between structure and diffusion patterns with the chemical sensitivity of relaxation rates. Moreover, the unprecedented resolution in the diffusion dimensions was observed to facilitate the separation of components with similar relaxation rates.

III In silico work shows that the non-parametric inversion of diffusion-correlated datasets is significantly challenged by the experimental noise, whose main effect is the introduction of bias in the estimated diffusion anisotropy. Despite its sensitivity to noise, we observed that model-free inversion preserves a good contrast at low SNR and exhibits a perfect accuracy at infinite SNR. When comparing the model-free algorithm with inversion approaches that directly target statistical measures of the underlying DTD, we found that the latter are more robust to noise but exhibit inherent limitations in the estimation of statistical descriptors. In order to increase the reliability of model-free inversion in clinical studies, future efforts should be spent in mitigating the bias towards anisotropy or the overall influence of noise.

IV The combination of multidimensional diffusion encoding with a SPEN MRI sequence enables diffusion tensor distribution imaging of the living mouse brain at a sub-millimetre resolution. The presented protocol shows promise for model-free investigations of microscopic tissue heterogeneity in animal models.

V Non-parametric five-dimensional R_2-$\mathbf{D}$ distributions were estimated voxel-wise for the living human brain. The distributions facilitated the resolution and subsequent characterization of microscopic brain tissue environments. The properties and localization of the estimated sub-voxel environments were found to agree well with the anatomy of the healthy brain.

VI Spatially-resolved R_2-$\mathbf{D}$ distributions can be used to map and visualize fibre-specific information. While no fibre-specific microstructural differences were immediately observed in the healthy brain, we nonetheless expect our approach to be useful in pathology studies dealing with fibre-specific microstructural changes.

References

[1] A. Einstein, *Investigations on the Theory of the Brownian Movement* (Courier Corporation, 1956).

[2] P. T. Callaghan, *Translational dynamics & magnetic resonance* (Oxford University Press, Oxford, 2011).

[3] W. S. Price, *NMR studies of translational motion* (Cambridge University Press, Cambridge, 2009).

[4] J. Crank *et al.*, *The mathematics of diffusion* (Oxford university press, 1979).

[5] D. S. Grebenkov, NMR survey of reflected Brownian motion, *Reviews of Modern Physics* **79**, 1077 (2007).

[6] P. Linse and O. Söderman, The validity of the short-gradient-pulse approximation in NMR studies of restricted diffusion, simulations of molecules diffusing between planes, in cylinders and spheres, *J. Magn. Reson. A* **116**, 77 (1995).

[7] D. S. Grebenkov, Use, misuse, and abuse of apparent diffusion coefficients, *Concepts in Magnetic Resonance Part A* **36A**, 24 (2010).

[8] D. E. Woessner, N.M.R. spin-echo self-diffusion measurements on fluids undergoing restricted diffusion, *J. Phys. Chem.* **67**, 1365 (1963).

[9] D. A. Yablonskiy, G. L. Bretthorst, and J. J. Ackerman, Statistical model for diffusion attenuated MR signal, *Magn. Reson. Med.* **50**, 664 (2003).

[10] P. J. Basser, J. Mattiello, and D. Le Bihan, MR diffusion tensor spectroscopy and imaging, *Biophys. J.* **66**, 259 (1994).

[11] C. F. Westin *et al.*, Q-space trajectory imaging for multidimensional diffusion MRI of the human brain, *Neuroimage* **135**, 345 (2016).

[12] G. Kindlmann, Superquadric tensor glyphs, in *Proceedings of the Sixth Joint Eurographics-IEEE TCVG conference on Visualization*, pp. 147–154, Eurographics Association, 2004.

[13] D. Topgaard, Diffusion tensor distribution imaging, *NMR Biomed.* **32**, e4066 (2019).

[14] U. Haeberlen, Adv Magn Reson Suppl. 1, *Academic, New York* (1976).

[15] D. Topgaard, Director orientations in lyotropic liquid crystals: diffusion MRI mapping of the Saupe order tensor, *Phys. Chem. Chem. Phys.* **18**, 8545 (2016).

[16] D. Topgaard, NMR Methods for Studying Microscopic Diffusion Anisotropy, in *Diffusion NMR of Confined Systems: Fluid Transport in Porous Solids and Heterogeneous Materials, New Developments in NMR*, edited by R. Valiullin, pp. 226–259, Cambridge, UK: Royal Society of Chemistry, 2016.

[17] R. Mills, Self-diffusion in normal and heavy water in the range 1-45.deg., *The Journal of Physical Chemistry* 77, 685 (1973).

[18] M. Holz, S. R. Heil, and A. Sacco, Temperature-dependent self-diffusion coefficients of water and six selected molecular liquids for calibration in accurate 1H NMR PFG measurements, *Phys. Chem. Chem. Phys.* **2**, 4740 (2000).

[19] D. A. Yablonskiy and A. L. Sukstanskii, Theoretical models of the diffusion weighted MR signal, *NMR Biomed.* **23**, 661 (2010).

[20] D. S. Novikov, E. Fieremans, S. N. Jespersen, and V. G. Kiselev, Quantifying brain microstructure with diffusion MRI: Theory and parameter estimation, *NMR Biomed.* **32**, e3998 (2019).

[21] F. Szczepankiewicz, *Imaging diffusional variance by MRI [public]: The role of tensor-valued diffusion encoding and tissue heterogeneity*, PhD thesis, Lund University, 2016.

[22] B. Jian, B. C. Vemuri, E. Özarslan, P. R. Carney, and T. H. Mareci, A novel tensor distribution model for the diffusion-weighted MR signal, *Neuroimage* **37**, 164 (2007).

[23] P. J. Basser and C. Pierpaoli, Microstructural and physiological features of tissues elucidated by quantitative-diffusion-tensor MRI, *Journal of magnetic resonance, Series B* **111**, 209 (1996).

[24] P. B. Kingsley, Introduction to diffusion tensor imaging mathematics: Part I. Tensors, rotations, and eigenvectors, *Concepts in Magnetic Resonance Part A* **28**, 101 (2006).

[25] M. Lawrenz, M. A. Koch, and J. Finsterbusch, A tensor model and measures of microscopic anisotropy for double-wave-vector diffusion-weighting experiments with long mixing times, *J. Magn. Reson.* **202**, 43 (2010).

[26] S. N. Jespersen, H. Lundell, C. K. S√∏nderby, and T. B. Dyrby, Orientationally invariant metrics of apparent compartment eccentricity from double pulsed field gradient diffusion experiments, *NMR Biomed.* **26**, 1647 (2013).

[27] S. Lasič, F. Szczepankiewicz, S. Eriksson, M. Nilsson, and D. Topgaard, Microanisotropy imaging: quantification of microscopic diffusion anisotropy and orientational order parameter by diffusion MRI with magic-angle spinning of the q-vector, *Frontiers in Physics* **2** (2014).

[28] F. Szczepankiewicz *et al.*, Quantification of microscopic diffusion anisotropy disentangles effects of orientation dispersion from microstructure: Applications in healthy volunteers and in brain tumors, *Neuroimage* **104**, 241 (2015).

[29] F. Szczepankiewicz *et al.*, The link between diffusion MRI and tumor heterogeneity: Mapping cell eccentricity and density by diffusional variance decomposition (DIVIDE), *Neuroimage* **142**, 522 (2016).

[30] C. Pierpaoli, P. Jezzard, P. J. Basser, A. Barnett, and G. Di Chiro, Diffusion tensor MR imaging of the human brain., *Radiology* **201**, 637 (1996).

[31] A. L. Alexander, K. M. Hasan, M. Lazar, J. S. Tsuruda, and D. L. Parker, Analysis of partial volume effects in diffusion-tensor MRI, *Magn. Reson. Med.* **45**, 770 (2001).

[32] R. J. Zatorre, R. D. Fields, and H. Johansen-Berg, Plasticity in gray and white: neuroimaging changes in brain structure during learning, *Nat. Neurosci.* **15**, 528 (2012).

[33] C. Slichter, *Principles of Magnetic Resonance*Lecture Notes in Computer Science (World Publishing Company, 1990).

[34] M. H. Levitt, *Spin dynamics: basics of nuclear magnetic resonance* (John Wiley & Sons, 2001).

[35] H. C. Torrey, Bloch Equations with Diffusion Terms, *Phys. Rev.* **104**, 563 (1956).

[36] F. V. Chávez and B. Halle, Molecular basis of water proton relaxation in gels and tissue, *Magn. Reson. Med.* **56**, 73 (2006).

[37] B. Halle, Molecular theory of field‚Äêdependent proton spin‚Äêlattice relaxation in tissue, *Magn. Reson. Med.* **56**, 60 (2006).

[38] L. Calucci and C. Forte, Proton longitudinal relaxation coupling in dynamically heterogeneous soft systems, *Prog. Nucl. Magn. Reson. Spectrosc.* **55**, 296 (2009).

[39] P. A. Bottomley, C. Hardy, R. Argersinger, and G. Allen-Moore, A review of 1H nuclear magnetic resonance relaxation in pathology: are T1 and T2 diagnostic?, *Med. Phys.* **14**, 1 (1987).

[40] R. M. Henkelman, G. J. Stanisz, J. K. Kim, and M. J. Bronskill, Anisotropy of NMR properties of tissues, *Magn. Reson. Med.* **32**, 592 (1994).

[41] M. D. Does, Inferring brain tissue composition and microstructure via MR relaxometry, *Neuroimage* **182**, 136 (2018).

[42] P. Tofts, *Quantitative MRI of the Brain: Measuring Changes Caused by Disease* (John Wiley & Sons, 2003).

[43] A. MacKay *et al.*, Insights into brain microstructure from the T2 distribution, *Magn. Reson. Imaging* **24**, 515 (2006).

[44] A. Mackay *et al.*, In vivo visualization of myelin water in brain by magnetic resonance, *Magn. Reson. Med.* **31**, 673 (1994).

[45] K. P. Whittall *et al.*, In vivo measurement of T2 distributions and water contents in normal human brain, *Magn. Reson. Med.* **37**, 34 (1997).

[46] S. Flynn *et al.*, Abnormalities of myelination in schizophrenia detected in vivo with MRI, and post-mortem with analysis of oligodendrocyte proteins, *Mol. Psychiatry* **8**, 811 (2003).

[47] C. Laule *et al.*, Myelin water imaging in multiple sclerosis: quantitative correlations with histopathology, *Multiple Sclerosis Journal* **12**, 747 (2006), PMID: 17263002.

[48] D. S. Grebenkov, *From the Microstructure to Diffusion NMR, and Back* (The Royal Society of Chemistry, 2016), book section 3, pp. 52–110.

[49] D. K. Jones, *Diffusion MRI* (Oxford University Press, 2010).

[50] E. O. Stejskal and J. E. Tanner, Spin diffusion measurements: Spin echoes in the presence of a time-dependent field gradient, *J. Chem. Phys.* **42**, 288 (1965).

[51] M. Kubicki *et al.*, A review of diffusion tensor imaging studies in schizophrenia, *J. Psychiatr. Res.* **41**, 15 (2007).

[52] S. Jbabdi, S. N. Sotiropoulos, S. N. Haber, D. C. Van Essen, and T. E. Behrens, Measuring macroscopic brain connections in vivo, *Nat. Neurosci.* **18**, 1546 (2015).

[53] J. P. Lerch *et al.*, Studying neuroanatomy using MRI, *Nat. Neurosci.* **20**, 314 (2017).

[54] M. Nilsson, E. Englund, F. Szczepankiewicz, D. van Westen, and P. C. Sundgren, Imaging brain tumour microstructure, *Neuroimage* **182**, 232 (2018).

[55] B. D. Boss and E. O. Stejskal, Anisotropic Diffusion in Hydrated Vermiculite, *The Journal of Chemical Physics* **43**, 1068 (1965).

[56] B. D. Boss, E. O. Stejskal, and J. D. Ferry, Self-diffusion in high molecular weight polyisobutylene-benzene mixtures determined by the pulsed-gradient, spin-echo method, *The Journal of Physical Chemistry* **71**, 1501 (1967).

[57] P. P. Mitra, Multiple wave-vector extension of the NMR pulsed-field-gradient spin-echo diffusion measurement, *Phys. Rev. B* **51**, 15074 (1995).

[58] S. Eriksson, S. Lasič, M. Nilsson, C. F. Westin, and D. Topgaard, NMR diffusion-encoding with axial symmetry and variable anisotropy: Distinguishing between prolate and oblate microscopic diffusion tensors with unknown orientation distribution, *J. Chem. Phys.* **142**, 104201 (2015).

[59] D. Topgaard, Multidimensional diffusion MRI, *J. Magn. Reson.* **275**, 98 (2017).

[60] D. G. Cory, A. N. Garroway, and J. B. Miller, Applications of spin transport as a probe of local geometry, *Polymer Prepr.* **31**, 149 (1990).

[61] P. T. Callaghan and I. Furó, Diffusion-diffusion correlation and exchange as a signature for local order and dynamics, *J. Chem. Phys.* **120**, 4032 (2004).

[62] S. Mori and P. C. M. Van Zijl, Diffusion Weighting by the Trace of the Diffusion Tensor within a Single Scan, *Magn. Reson. Med.* **33**, 41.

[63] S. Eriksson, S. Lasič, and D. Topgaard, Isotropic diffusion weighting in PGSE NMR by magic-angle spinning of the q-vector, *J. Magn. Reson.* **226**, 13 (2013).

[64] N. Shemesh *et al.*, Conventions and nomenclature for double diffusion encoding NMR and MRI, *Magn. Reson. Med.* **75**, 82 (2016).

[65] K. Schmidt-Rohr and H. W. Spiess, *Multidimensional solid-state NMR and polymers* (Academic Press, 1994).

[66] E. Andrew, A. Bradbury, and R. Eades, Removal of dipolar broadening of nuclear magnetic resonance spectra of solids by specimen rotation, *Nature* **183**, 1802 (1959).

[67] A. Bax, N. M. Szeverenyl, and G. E. Maciel, Chemical shift anisotropy in powdered solids studied by 2D FT NMR with flipping of the spinning axis, *J. Magn. Reson.* **55**, 494 (1983).

[68] N. M. Szeverenyi, A. Bax, and G. E. Maciel, Magic-angle hopping as an alternative to magic-angle spinning for solid state NMR, *J. Magn. Reson.* **61**, 440 (1985).

[69] L. Frydman *et al.*, Variable-angle correlation spectroscopy in solid-state nuclear magnetic resonance, *J. Chem. Phys.* **97**, 4800 (1992).

[70] M. Lawrenz and J. Finsterbusch, Double-wave-vector diffusion-weighted imaging reveals microscopic diffusion anisotropy in the living human brain, *Magn. Reson. Med.* **69**, 1072 (2013).

[71] E. Kaden, N. D. Kelm, R. P. Carson, M. D. Does, and D. C. Alexander, Multicompartment microscopic diffusion imaging, *Neuroimage* **139**, 346 (2016).

[72] E. Kaden, F. Kruggel, and D. C. Alexander, Quantitative mapping of the per-axon diffusion coefficients in brain white matter, *Magn. Reson. Med.* **75**, 1752 (2016).

[73] M. Edén, Computer simulations in solid-state NMR. III. Powder averaging, *Concepts in Magnetic Resonance Part A* **18A**, 24 (2003).

[74] F. Szczepankiewicz, J. Sjolund, F. Stahlberg, J. Latt, and M. Nilsson, Tensor-valued diffusion encoding for diffusional variance decomposition (DIVIDE): Technical feasibility in clinical MRI systems, *PLoS One* **14**, e0214238 (2019).

[75] M. Herberthson, C. Yolcu, H. Knutsson, C.-F. Westin, and E. Özarslan, Orientationally-averaged diffusion-attenuated magnetic resonance signal for locally-anisotropic diffusion, *Scientific Reports* **9**, 4899 (2019).

[76] D. Topgaard and O. Söderman, Self-diffusion in two-and three-dimensional powders of anisotropic domains: An NMR study of the diffusion of water in cellulose and starch, *J. Phys. Chem. B* **106**, 11887 (2002).

[77] Y.-Q. Song, A 2D NMR method to characterize granular structure of dairy products, *Prog. Nucl. Magn. Reson. Spectrosc.* **55**, 324 (2009).

[78] D. Bernin and D. Topgaard, NMR diffusion and relaxation correlation methods: New insights in heterogeneous materials, *Curr. Opin. Colloid Interface Sci.* **18**, 166 (2013).

[79] Y. Q. Song, Magnetic resonance of porous media (MRPM): a perspective, *J. Magn. Reson.* **229**, 12 (2013).

[80] R. R. Ernst *et al.*, *Principles of nuclear magnetic resonance in one and two dimensions*volume 14 (Clarendon press Oxford, 1987).

[81] A. A. Istratov and O. F. Vyvenko, Exponential analysis in physical phenomena, *Rev. Sci. Instrum.* **70**, 1233 (1999).

[82] K. P. Whittall and A. L. MacKay, Quantitative interpretation of NMR relaxation data, *J. Magn. Reson.* **84**, 134 (1989).

[83] J. Mitchell, T. C. Chandrasekera, and L. F. Gladden, Numerical estimation of relaxation and diffusion distributions in two dimensions, *Prog. Nucl. Magn. Reson. Spectrosc.* **62**, 34 (2012).

[84] Y. Q. Song *et al.*, T1–T2 correlation spectra obtained using a fast two-dimensional Laplace inversion, *J. Magn. Reson.* **154**, 261 (2002).

[85] M. D. Hürlimann and L. Venkataramanan, Quantitative Measurement of Two-Dimensional Distribution Functions of Diffusion and Relaxation in Grossly Inhomogeneous Fields, *J. Magn. Reson.* **157**, 31 (2002).

[86] P. Callaghan, S. Godefroy, and B. Ryland, Diffusion–relaxation correlation in simple pore structures, *J. Magn. Reson.* **162**, 320 (2003).

[87] Y. Qiao, P. Galvosas, and P. T. Callaghan, Diffusion correlation NMR spectroscopic study of anisotropic diffusion of water in plant tissues, *Biophys. J.* **89**, 2899 (2005).

[88] P. Galvosas and P. T. Callaghan, Multi-dimensional inverse Laplace spectroscopy in the NMR of porous media, *C. R. Phys.* **11**, 172 (2010).

[89] L. F. Gladden and J. Mitchell, Measuring adsorption, diffusion and flow in chemical engineering: applications of magnetic resonance to porous media, *New Journal of Physics* **13**, 035001 (2011).

[90] J. P. de Almeida Martins and D. Topgaard, Two-Dimensional Correlation of Isotropic and Directional Diffusion Using NMR, *Phys. Rev. Lett.* **116**, 087601 (2016).

[91] D. Topgaard, Isotropic diffusion weighting using a triple-stimulated echo pulse sequence with bipolar gradient pulse pairs, *Microporous Mesoporous Mater.* , 48 (2015).

[92] M. Nilsson *et al.*, Liquid crystal phantom for validation of microscopic diffusion anisotropy measurements on clinical MRI systems, *Magn. Reson. Med.* (2017).

[93] G. J. Stanisz, A. Szafer, G. A. Wright, and R. M. Henkelman, An analytical model of restricted diffusion in bovine optic nerve, *Magn. Reson. Med.* **37**, 103 (1997).

[94] P. Tofts, *Quantitative MRI of the brain: measuring changes caused by disease* (John Wiley & Sons, 2005).

[95] A. Daoust *et al.*, Transverse relaxation of cerebrospinal fluid depends on glucose concentration, *Magn. Reson. Imaging* **44**, 72 (2017).

[96] S. De Santis, D. Barazany, D. K. Jones, and Y. Assaf, Resolving relaxometry and diffusion properties within the same voxel in the presence of crossing fibres by combining inversion recovery and diffusion–weighted acquisitions, *Magn. Reson. Med.* **75**, 372 (2016).

[97] J. Veraart, D. S. Novikov, and E. Fieremans, TE dependent Diffusion Imaging (TEdDI) distinguishes between compartmental T2 relaxation times, *Neuroimage* **182**, 360 (2018).

[98] J. P. de Almeida Martins and D. Topgaard, Multidimensional correlation of nuclear relaxation rates and diffusion tensors for model-free investigations of heterogeneous anisotropic porous materials, *Sci. Rep.* **8**, 2488 (2018).

[99] S. Eriksson *et al.*, NMR quantification of diffusional exchange in cell suspensions with relaxation rate differences between intra and extracellular compartments, *PloS one* **12**, e0177273 (2017).

[100] Y.-Q. Song, L. Venkataramanan, R. Kausik, and N. Heaton, *Two-dimensional NMR of Diffusion and Relaxation* (The Royal Society of Chemistry, 2016), book section 4, pp. 111–155.

[101] C. L. Lawson and R. J. Hanson, *Solving least squares problems* (Prentice-Hall, 1974).

[102] M. Urbańczyk, D. Bernin, W. Koźmiński, and K. Kazimierczuk, Iterative Thresholding Algorithm for Multiexponential Decay Applied to PGSE NMR Data, *Anal. Chem.* **85**, 1828 (2013), PMID: 23297715.

[103] M. Slawski *et al.*, Non-negative least squares for high-dimensional linear models: Consistency and sparse recovery without regularization, *Electronic Journal of Statistics* **7**, 3004 (2013).

[104] S. W. Provencher, CONTIN: a general purpose constrained regularization program for inverting noisy linear algebraic and integral equations, *Comput. Phys. Commun.* **27**, 229 (1982).

[105] L. Venkataramanan, Y.-Q. Song, and M. D. Hurlimann, Solving Fredholm integrals of the first kind with tensor product structure in 2 and 2.5 dimensions, **50**, 1017 (2002).

[106] P. T. Callaghan, S. Godefroy, and B. N. Ryland, Use of the second dimension in PGSE NMR studies of porous media, *Magn. Reson. Imaging* **21**, 243 (2003).

[107] P. Berman, O. Levi, Y. Parmet, M. Saunders, and Z. Wiesman, Laplace inversion of low-resolution NMR relaxometry data using sparse representation methods, *Concepts in Magnetic Resonance Part A* **42**, 72 (2013).

[108] D. Benjamini and P. J. Basser, Use of marginal distributions constrained optimization (MADCO) for accelerated 2D MRI relaxometry and diffusometry, *J. Magn. Reson.* **271**, 40 (2016).

[109] M. Delsuc and T. Malliavin, Maximum entropy processing of DOSY NMR spectra, *Anal. Chem.* **70**, 2146 (1998).

[110] E. Chouzenoux, S. Moussaoui, J. Idier, and F. Mariette, Efficient maximum entropy reconstruction of nuclear magnetic resonance T1-T2 spectra, *IEEE Trans. Signal Proc.* **58**, 6040 (2010).

[111] A. Daducci *et al.*, Accelerated Microstructure Imaging via Convex Optimization (AMICO) from diffusion MRI data, *Neuroimage* **105**, 32 (2015).

[112] M. D. Hürlimann, L. Burcaw, and Y.-Q. Song, Quantitative characterization of food products by two-dimensional D–T2 and T1–T2 distribution functions in a static gradient, *J. Colloid Interface Sci.* **297**, 303 (2006).

[113] M. Prange and Y. Q. Song, Quantifying uncertainty in NMR T2 spectra using Monte Carlo inversion, *J. Magn. Reson.* **196**, 54 (2009).

[114] M. Prange and Y. Q. Song, Understanding NMR T(2) spectral uncertainty, *J. Magn. Reson.* **204**, 118 (2010).

[115] D. W. de Kort, J. P. van Duynhoven, F. J. Hoeben, H. M. Janssen, and H. Van As, NMR nanoparticle diffusometry in hydrogels: enhancing sensitivity and selectivity, *Anal. Chem.* **86**, 9229 (2014).

[116] D. E. Koppel, Analysis of Macromolecular Polydispersity in Intensity Correlation Spectroscopy: The Method of Cumulants, *J. Chem. Phys.* **57**, 4814 (1972).

[117] N. G. Van Kampen, *Stochastic processes in physics and chemistry*volume 1 (Elsevier, 1992).

[118] V. G. Kiselev, The cumulant expansion: an overarching mathematical framework for understanding diffusion NMR, in *Diffusion MRI: theory, methods, and applications*, edited by D. K. Jones, pp. 152–168, Oxford Univ. Press, 2010.

[119] J. H. Jensen, J. A. Helpern, A. Ramani, H. Lu, and K. Kaczynski, Diffusional kurtosis imaging: The quantification of non-gaussian water diffusion by means of magnetic resonance imaging, *Magn. Reson. Med.* **53**, 1432 (2005).

[120] V. G. Kiselev and K. A. Il'yasov, Is the "biexponential diffusion" biexponential?, *Magnetic Resonance in Medicine: An Official Journal of the International Society for Magnetic Resonance in Medicine* **57**, 464 (2007).

[121] D. L. VanderHart and H. S. Gutowsky, Rigid-Lattice NMR Moments and Line Shapes with Chemical-Shift Anisotropy, *J. Chem. Phys.* **49**, 261 (1968).

[122] J. H. Jensen and J. A. Helpern, MRI quantification of non-Gaussian water diffusion by kurtosis analysis, *NMR Biomed.* **23**, 698 (2010).

[123] M. Röding *et al.*, The gamma distribution model for pulsed-field gradient NMR studies of molecular-weight distributions of polymers, *J. Magn. Reson.* **222**, 105—111 (2012).

[124] D. K. Jones and M. Cercignani, Twenty-five pitfalls in the analysis of diffusion MRI data, *NMR Biomed.* **23**, 803 (2010).

[125] S. J. Graham, P. L. Stanchev, and M. J. Bronskill, Criteria for analysis of multicomponent tissue T2 relaxation data, *Magn. Reson. Med.* **35**, 370 (1996).

[126] F. Fenrich, C. Beaulieu, and P. Allen, Relaxation times and microstructures, *NMR Biomed.* **14**, 133 (2001).

[127] J. Sjölund *et al.*, Constrained optimization of gradient waveforms for generalized diffusion encoding, *J. Magn. Reson.* **261**, 157 (2015).

[128] N. Ben-Eliezer and L. Frydman, Spatiotemporal encoding as a robust basis for fast three-dimensional in vivo MRI, *NMR Biomed.* **24**, 1191 (2011).

[129] R. Schmidt and L. Frydman, New spatiotemporal approaches for fully refocused, multislice ultrafast 2D MRI, *Magn. Reson. Med.* **71**, 711 (2014).

[130] E. Solomon, G. Liberman, N. Nissan, and L. Frydman, Robust diffusion tensor imaging by spatiotemporal encoding: Principles and in vivo demonstrations, *Magn. Reson. Med.* **77**, 1124 (2017).

[131] E. Fieremans and H.-H. Lee, Physical and numerical phantoms for the validation of brain microstructural MRI: A cookbook, *Neuroimage* **182**, 39 (2018).

[132] S. Gatidis, H. Schmidt, P. Martirosian, and N. F. Schwenzer, Development of an MRI phantom for diffusion-weighted imaging with independent adjustment of apparent diffusion coefficient values and T2 relaxation times, *Magn. Reson. Med.* **72**, 459 (2014).

[133] I. Åslund and D. Topgaard, Determination of the self-diffusion coefficient of intracellular water using PGSE NMR with variable gradient pulse length, *J. Magn. Reson.* **201**, 250 (2009).

[134] E. Fieremans, A. Pires, and J. H. Jensen, A simple isotropic phantom for diffusional kurtosis imaging, *Magn. Reson. Med.* **68**, 537 (2012).

[135] S. E. Maier, D. Mitsouras, and R. V. Mulkern, Avian egg latebra as brain tissue water diffusion model, *Magn. Reson. Med.* **72**, 501 (2014).

[136] J. Lätt *et al.*, Effects of restricted diffusion in a biological phantom: a q-space diffusion MRI study of asparagus stems at a 3T clinical scanner, *Magnetic Resonance Materials in Physics, Biology and Medicine* **20**, 213 (2007).

[137] N. Yanasak and J. Allison, Use of capillaries in the construction of an MRI phantom for the assessment of diffusion tensor imaging: demonstration of performance, *Magn. Reson. Imaging* **24**, 1349 (2006).

[138] E. A. von dem Hagen and R. M. Henkelman, Orientational diffusion reflects fiber structure within a voxel, *Magn. Reson. Med.* **48**, 454 (2002).

[139] M. Komlosh *et al.*, Detection of microscopic anisotropy in gray matter and in a novel tissue phantom using double pulsed gradient spin echo MR, *J. Magn. Reson.* **189**, 38 (2007).

[140] M. Lawrenz and J. Finsterbusch, Detection of microscopic diffusion anisotropy on a whole-body MR system with double wave vector imaging, *Magn. Reson. Med.* **66**, 1405 (2011).

[141] D. Wu *et al.*, In vivo high-resolution diffusion tensor imaging of the mouse brain, *Neuroimage* **83**, 18 (2013).

[142] M. Aggarwal, S. Mori, T. Shimogori, S. Blackshaw, and J. Zhang, Three-dimensional diffusion tensor microimaging for anatomical characterization of the mouse brain, *Magn. Reson. Med.* **64**, 249 (2010).

[143] N. Shemesh and Y. Cohen, Microscopic and compartment shape anisotropies in gray and white matter revealed by angular bipolar double-PFG MR, *Magn. Reson. Med.* **65**, 1216 (2011).

[144] K. B. Franklin *et al.*, *The mouse brain in stereotaxic coordinates*volume 3 (Academic press New York:, 2008).

[145] S. Godefroy and P. Callaghan, 2D relaxation/diffusion correlations in porous media, *Magn. Reson. Imaging* **21**, 381 (2003).

[146] J. G. Seland, M. Bruvold, H. Brurok, P. Jynge, and J. Krane, Analyzing equilibrium water exchange between myocardial tissue compartments using dynamical two-dimensional correlation experiments combined with manganese-enhanced relaxography, *Magn. Reson. Med.* **58**, 674 (2007).

[147] N. Marigheto, L. Venturi, and B. Hills, Two-dimensional NMR relaxation studies of apple quality, *Postharvest Biol. Technol.* **48**, 331 (2008).

[148] A. E. English, K. P. Whittal, M. L. G. Joy, and R. M. Henkelman, Quantitative two-dimensional time correlation relaxometry, *Magn. Reson. Med.* **22**, 425 (1991).

[149] D. Kim, E. K. Doyle, J. L. Wisnowski, J. H. Kim, and J. P. Haldar, Diffusion-relaxation correlation spectroscopic imaging: A multidimensional approach for probing microstructure, *Magn. Reson. Med.* **78**, 2236 (2017).

[150] D. Benjamini and P. J. Basser, Magnetic resonance microdynamic imaging reveals distinct tissue microenvironments, *Neuroimage* **163**, 183 (2017).

[151] P. J. Slator *et al.*, Combined diffusion-relaxometry MRI to identify dysfunction in the human placenta, *Magn. Reson. Med.* **82**, 95 (2019).

[152] P. Mansfield, Multi-planar image formation using NMR spin echoes, *J. Phys. C* **10**, L55 (1977).

[153] M. Nilsson, D. van Westen, F. Ståhlberg, P. C. Sundgren, and J. L√§tt, The role of tissue microstructure and water exchange in biophysical modelling of diffusion in white matter, *Magn. Reson. Mater. Phy.* **26**, 345 (2013).

[154] J. Veraart, D. S. Novikov, and E. Fieremans, TE dependent Diffusion Imaging (TEdDI) distinguishes between compartmental T2 relaxation times, *Neuroimage* (2017).

[155] B. Lampinen *et al.*, Searching for the neurite density with diffusion MRI: Challenges for biophysical modeling, *Hum. Brain Mapp.* **40**, 2529 (2019).

[156] M. Lawrenz and J. Finsterbusch, Mapping measures of microscopic diffusion anisotropy in human brain white matter in vivo with double-wave-vector diffusion-weighted imaging, *Magn. Reson. Med.* **73**, 773 (2015).

[157] B. Fischl *et al.*, Whole brain segmentation: automated labeling of neuroanatomical structures in the human brain, *Neuron* **33**, 341 (2002).

[158] K. M. Hasan, I. S. Walimuni, L. A. Kramer, and P. A. Narayana, Human brain iron mapping using atlas-based T2 relaxometry, *Magn. Reson. Med.* **67**, 731 (2012).

[159] M. J. Knight, B. Wood, E. Couthard, and R. Kauppinen, Anisotropy of spin-echo T2 relaxation by magnetic resonance imaging in the human brain in vivo, *Biomedical Spectroscopy and Imaging* **4**, 299 (2015).

[160] P. Hagmann *et al.*, Understanding diffusion MR imaging techniques: from scalar diffusion-weighted imaging to diffusion tensor imaging and beyond, *Radiographics* **26**, S205 (2006).

[161] J. D. Tournier, F. Calamante, D. G. Gadian, and A. Connelly, Direct estimation of the fiber orientation density function from diffusion-weighted MRI data using spherical deconvolution, *Neuroimage* **23**, 1176 (2004).

[162] G. Watson, Equatorial distributions on a sphere, *Biometrika* **52**, 193 (1965).

[163] K. V. Mardia and P. E. Jupp, *Directional statistics* (John Wiley & Sons, 2009).

[164] R. Gil *et al.*, An in vivo study of the orientation-dependent and independent components of transverse relaxation rates in white matter, *NMR Biomed.* **29**, 1780 (2016).

[165] E. T. McKinnon and J. H. Jensen, Measuring intra-axonal T2 in white matter with direction-averaged diffusion MRI, *Magn. Reson. Med.* **81**, 2985 (2019).

Scientific Publications

Author Contributions

Paper I: Two-Dimensional Correlation of Isotropic and Directional Diffusion Using NMR

I assembled the phantoms, was responsible for the NMR measurements, and analysed the data. I contributed to formalising the theory described in the supplemental material. I was the main author of the paper.

Paper II: Multidimensional correlation of nuclear relaxation rates and diffusion tensors for model-free investigations of heterogeneous anisotropic porous materials

I assembled the phantoms and was responsible for the NMR measurements, contributed to the development of the analysis code, and analysed all experimental data. I designed and performed the simulations testing the limits of the proposed inversion algorithm. I was the main author of the paper.

Paper III: Trueness and precision of statistical descriptors obtained from multidimensional diffusion signal inversion algorithms

I contributed to the design of the study and the data analysis. I wrote the manuscript together with the main co-author.

Paper IV: Diffusion tensor distribution imaging of *in vivo* mouse brain at ultra-high magnetic field by spatiotemporal encoding

I contributed to the design of the analysis pipeline and analysed the data. I wrote the manuscript together with the main co-author.

Paper V: Transferring principles of solid-state and Laplace NMR to the field of *in vivo* brain MRI

I contributed to the design of the *in vivo* experiments, designed and implemented the proposed inversion algorithm together with D. Topgaard, and analysed the data. I was the main author of the paper.

Paper VI: Mapping and visualizing fibres in heterogeneous brain voxels

I contributed to the design of the study, contributed to the design of the *in vivo* acquisition protocol, implemented the Orientation Distribution Function reconstruction algorithm together with D. Topgaard, and analysed the data. I was the main author of the paper.